

INFORMATION TO USERS

The most advanced technology has been used to photograph and reproduce this manuscript from the microfilm master. UMI films the text directly from the original or copy submitted. Thus, some thesis and dissertation copies are in typewriter face, while others may be from any type of computer printer.

The quality of this reproduction is dependent upon the quality of the copy submitted. Broken or indistinct print, colored or poor quality illustrations and photographs, print bleedthrough, substandard margins, and improper alignment can adversely affect reproduction.

In the unlikely event that the author did not send UMI a complete manuscript and there are missing pages, these will be noted. Also, if unauthorized copyright material had to be removed, a note will indicate the deletion.

Oversize materials (e.g., maps, drawings, charts) are reproduced by sectioning the original, beginning at the upper left-hand corner and continuing from left to right in equal sections with small overlaps. Each original is also photographed in one exposure and is included in reduced form at the back of the book.

Photographs included in the original manuscript have been reproduced xerographically in this copy. Higher quality 6" x 9" black and white photographic prints are available for any photographs or illustrations appearing in this copy for an additional charge. Contact UMI directly to order.

U·M·I

University Microfilms International
A Bell & Howell Information Company
300 North Zeeb Road, Ann Arbor, MI 48106-1346 USA
313.761-4700 800.521-0600



Order Number 9028144

**In-flight methods for satellite sensor absolute radiometric
calibration**

Biggar, Stuart Frick, Ph.D.

The University of Arizona, 1990

U·M·I
300 N. Zeeb Rd.
Ann Arbor, MI 48106



**IN-FLIGHT METHODS FOR SATELLITE SENSOR
ABSOLUTE RADIOMETRIC CALIBRATION**

by

Stuart Frick Biggar

A Dissertation Submitted to the Faculty of the
COMMITTEE ON OPTICAL SCIENCES (Graduate)

In Partial Fulfillment of the Requirements
For the Degree of

DOCTOR OF PHILOSOPHY

In the Graduate College

THE UNIVERSITY OF ARIZONA

1990

THE UNIVERSITY OF ARIZONA
GRADUATE COLLEGE

As members of the Final Examination Committee, we certify that we have read
the dissertation prepared by Stuart Frick Biggar

entitled In-flight Methods for Satellite Sensor Absolute
Radiometric Calibration

and recommend that it be accepted as fulfilling the dissertation requirement
for the Degree of Doctor of Philosophy.

<u>P. Slater</u>	<u>April 6, 1990</u>
	Date
<u>Ray L. Jackson</u>	<u>April 6, 1990</u>
	Date
<u>Stuart L. Mayh</u>	<u>April 6, 1990</u>
	Date
<u>James M. Palmer</u>	<u>April 6, 1990</u>
	Date
<u>A. Mearns</u>	<u>April 6, 1990</u>
	Date

Final approval and acceptance of this dissertation is contingent upon the
candidate's submission of the final copy of the dissertation to the Graduate
College.

I hereby certify that I have read this dissertation prepared under my
direction and recommend that it be accepted as fulfilling the dissertation
requirement.

<u>P. Slater</u>	<u>May 3, 1990</u>
Dissertation Director	Date

STATEMENT BY AUTHOR

This dissertation has been submitted in partial fulfillment of requirements for an advanced degree at The University of Arizona and is deposited in the University Library to be made available to borrowers under rules of the Library.

Brief quotations from this thesis are allowable without special permission, provided that accurate acknowledgement of source is made. Requests for permission for extended quotation from or reproduction of this manuscript in whole or in part may be granted by the head of the major department or the Dean of the Graduate College when in his or her judgment the proposed use of the material is in the interests of scholarship. In all other instances, however, permission must be obtained from the author.

SIGNED:

Arthur F. Bugg

ACKNOWLEDGMENTS

I would like to thank my wife Joan and daughter Gwen for their support during my second career as a student. They put up with months of having a husband and father too busy for many family activities. I would like to thank my advisor, Dr. Philip N. Slater, for his guidance and patience during the past six years. Special thanks also go to Dr. Richard Santer whose help was instrumental in the work on the irradiance method. I would also like to thank Drs. Ray Jackson and Jim Palmer for their advice and help. I would like to thank visiting scholars Dr. Phil Teillet, Yuan Benfan and Che Nianzeng for their help in developing data reduction methods and measurement techniques. I would like to thank Jelila Labeled for her work in the reflectance panel calibration project. Many people helped in the collection of data in the field at White Sands. Thanks to Susan Moran and Tom Clarke from the USDA Water Conservation Laboratory and to University of Arizona staff and students David Gellman, Rick Bartell, Ron Holm, Carol Kastner, Ken Castle, Mark Smith, Barbara Grant, Quinn Hart, David Flittner, Carmen Guzman, Amy Phillips, Linda Lingg, and Carter Grotbeck. I would also like to acknowledge the help of Doug Ream, Manny Rico, Dan Ferralez, and Rich Savage of the Atmospheric Sciences Laboratory at White Sands, and the people of the US Army helicopter unit located at Holloman Air Force Base. The research for this dissertation was funded under NASA grant NAGW-896.

TABLE OF CONTENTS

	Page
LIST OF TABLES	9
LIST OF ILLUSTRATIONS	12
ABSTRACT	14
1. INTRODUCTION	16
2. RADIATIVE TRANSFER CODES AND MODELS	23
Introduction to Beer's law, the atmosphere, and polarization	24
The Equation of Transfer	27
The Phase Function	32
Rayleigh Scattering	32
Mie Scattering	34
Scattering Cross Section	36
Particle size distribution	37
Optical Depth	40
Partition of optical depths by the two-point method	43
Iterative partition	44
Verification of the Iterative Method	45
The radiative transfer codes	49
Boundary conditions	49
Solution strategy	50
Herman and Browning code	51
Deuzé code	52
The Simulation of the Satellite Signal in the Solar Spectrum (5S) approximate code	52

TABLE OF CONTENTS (Continued)

		Page
3.	REFLECTANCE MEASUREMENT AND THE REFLECTANCE-BASED METHOD	54
	Reflectance Panel Calibration	54
	Calibration Facility and Methodology	55
	Equipment and fixtures	55
	Motion control and data acquisition	56
	Radiometer and source	57
	Noise and integration time	58
	Halon® reference	59
	Derivation of Directional Reflectance Factor	60
	Experimental Procedure and Results	61
	Procedure	61
	BaSO ₄ panel calibrations	63
	Comparison between the field and laboratory calibrations	64
	Summary of the field method	64
	Differences between the laboratory and field experiments ...	66
	Comparison	67
	Conclusions	68
	Optical Depth Determination	69
	Measurements at MAC III	69
	Spectral Optical Depths at MAC III	71
	The Reflectance-based method	74

TABLE OF CONTENTS (Continued)

		Page
4.	THE RADIANCE-BASED METHOD	79
	Spectral Calibration	81
	Radiometric Calibration	83
	Conclusions	96
5.	THE IRRADIANCE-BASED METHOD	98
	Introduction	98
	Theory of the Irradiance-Based Method	98
	Expression for the apparent reflectance	99
	Relative contribution of atmospheric and ground reflectance	102
	Error analysis	104
	Irradiance Measurements	109
	Principle	109
	Field Measurements	114
	Corrections to the diffuse-to-global ratio related to the non-lambertian properties of the BaSO ₄ panel	124
	Truncated diffuse irradiance	126
	Solid angle estimate	127
	Computation of the irradiance	129
	Comparison of the reflectance- and irradiance-based methods	131
	Comparison of the measured diffuse-to-global ratio to an estimate using a transfer code	131
	Comparison of the two methods	134
	Conclusions	138

TABLE OF CONTENTS (Continued)

	Page
6. CONCLUSIONS	139
Reflectance-based Method	139
Radiance-based Method	141
Irradiance-based Method	142
Error Contributions	142
Recommendations	146
LIST OF REFERENCES	150

LIST OF TABLES

	Page
2.1 Errors and standard deviations for the two-point and iterative method simulation	47
3.1 Integration time versus standard deviation	59
3.2 Extinction optical depths (δ) at MAC III	71
3.3 Spectral optical depth components at MAC III	73
4.1 Exotech 3526 responses during laboratory calibration of 87.12.04 with FEL lamp F196 and BaSO ₄ panel #3	85
4.2 SPOT HRV filters/Exotech detector equivalent wavelengths in micrometers (μm) as determined by the moments method	86
4.3 Standard lamp F196 and BaSO ₄ panel #3 parameters for the 87.12.04 calibration	90
4.4 Average Exotech outputs for 87.07.17 over Chuck Site at White Sands Missile Range	91
4.5 Measured average scene radiances in $\text{W}/\text{m}^2\text{-sr-}\mu\text{m}$ for 87.07.17 over Chuck Site at White Sands Missile Range	92
4.6 Interpolated measured and computed scene radiances in $\text{W}/\text{m}^2\text{-sr-}\mu\text{m}$ for 87.07.17 over Chuck Site at White Sands Missile Range	92
4.7 Average Exotech outputs for 88.11.21 over Chuck Site at White Sands Missile Range	94
4.8 Measured average scene radiances in $\text{W}/\text{m}^2\text{-sr-}\mu\text{m}$ for 88.11.21 over Chuck Site at White Sands Missile Range	94
4.9 Measured and computed scene radiances in $\text{W}/\text{m}^2\text{-sr-}\mu\text{m}$ for 88.11.21 over Chuck Site at White Sands Missile Range	95
4.10 Computed scene radiances at 10000 feet MSL and the top of the atmosphere in $\text{W}/\text{m}^2\text{-sr-}\mu\text{m}$ for 88.11.21 over Chuck Site at White Sands Missile Range	96
4.11 Measured and computed scene radiances in $\text{W}/\text{m}^2\text{-sr-}\mu\text{m}$ for 86.03.08 over Chuck Site at White Sands Missile Range	96

	10
5.1	Ground reflectances for the band centers of the solar reflective TM bands on 1985.11.16 103
5.2	Estimation of the accuracy of the irradiance method 107
5.3	Estimation of the inaccuracy of the irradiance method for different ground reflectances 110
5.4	Optical thickness and ground reflectances for the White Sands calibrations 116
5.5a	Diffuse-to-global ratio measurements at White Sands in 1985 118
5.5b	Diffuse-to-global ratio measurements using the Barnes on 87.03.27 at White Sands 119
5.5c	Diffuse-to-direct measurements with Exotech at White Sands on 87.07.17 120
5.5d	Diffuse-to-global ratio for White Sands on 87.03.28, for SPOT using panel 11 121
5.5e	Diffuse-to-global flux measurements using the Exotech on 88.02.08 at White Sands 122
5.5f	Diffuse-to-global flux measurements using the Exotech on 88.02.09 at White Sands 123
5.5g	Diffuse-to-global flux measurements using the Barnes on 88.02.10 at White Sands 124
5.6	Diffuse-to-global ratio variability data from measurements using the Barnes on 87.03.27 at White Sands 125
5.7	Simulated diffuse-to-global ratios for perfect and non-lambertian panel and Rayleigh and 23 km visibility atmospheres 127
5.8	Errors in apparent reflectance for Rayleigh and 23-km visibility atmospheres for a view zenith angle of 10 degrees 128
5.9	Percentage increase in diffuse-to-global ratio on 88.02.10 due to diffuse correction according to equation 4.23 132
5.10	Geometrical conditions of the observations, aerosol optical depth, and Junge slope ν used for the aerosol characterization 135
5.11	Apparent reflectances computed using a transfer code and the irradiance method and relative difference (%) 136

	11
6.1 Reflectance-based method error sources	144
6.2 Radiance-based method error sources	145
6.3 Irradiance-based method error sources	146

LIST OF ILLUSTRATIONS

		Page
2.1	Atmospheric processes	25
2.2	Coordinate system and angles	28
2.3	Standard deviation of the Junge parameter from simulation	48
2.4	Standard deviation of the ozone amount from simulation	49
3.1	Reflectance measurement layout	56
3.2	Fitted <i>B</i> coefficient for Halon®	62
3.3	Panel OSC #2 reflectance factors	64
3.4	Reflectance factors at 450 nm	65
3.5	Normalized irradiance and filter response	67
3.6	Reflectance factor comparison	68
3.7	Langley plot for 0.6108 μm on 88.06.12 at MAC	70
3.8	Optical depths on 88.06.11 at MAC	74
3.9	Optical depths on 88.06.12 at MAC	75
3.10	Optical depths on 88.06.13 at MAC	76
4.1	Lamp F196 spectral irradiance	83
4.2	SPOT HRV Panchromatic band filter response	87
4.3	SPOT HRV Spectral band 1 (XS1) filter response	88
4.4	SPOT HRV Spectral band 2 (XS2) filter response	89
4.5	SPOT HRV Spectral band 3 (XS3) filter response	90
4.6	BaSO ₄ panel #3 spectral reflectance factor at 45 degrees	91
5.1	Irradiance decomposition	101
5.2	Spectral dependence of the normalized extinction coefficient for three aerosol models	103

5.3	Computation of the apparent reflectances measured in the TM bands for three aerosol models and for a solar zenith angle of 30 degrees	105
5.4	Computation of the apparent reflectances measured in the TM bands for three aerosol models and for a winter observation with a solar zenith angle of 60 degrees	106
5.5a	Variation of the TM1 apparent reflectance computed for the three aerosol models versus the ground reflectances for the winter case	108
5.5b	Variation of the TM4 apparent reflectance computed for the three aerosol models versus the ground reflectances for the winter case	109
5.6a	Diffuse-to-global measurement setup -- Unshaded by parasol	111
5.6b	Diffuse-to-global measurement setup -- Shaded by parasol	111
5.7	Diffuse-to-global ratio computed versus the airmass for TM1 band and ground reflectances of 0.0 and 0.5	113
5.8	Diffuse-to-global ratio measured on 87.03.27 in the TM1 band	117
5.9	Reflectance factor of BaSO ₄ panel 11	125
5.10	Panel and parasol geometry	129
5.11	Angle definitions for diffuse correction	130
5.12	Diffuse-to-global ratio measured at TM overpass time	133

ABSTRACT

Three methods for the in-flight absolute radiometric calibration of satellite sensors are presented. The Thematic Mapper (TM) on the Landsat satellites and the HRV on the SPOT satellite have been calibrated using the three methods at the White Sands Missile Range in New Mexico. Ground and airborne measurements of ground reflectance, radiance, atmospheric, and weather parameters are made coincident with satellite image acquisition. The data are analyzed to determine inputs to radiative transfer codes. The codes compute the radiance at the sensor entrance pupil which is compared to the average digital count from the measured ground area. The three methods are the reflectance-based, radiance-based and irradiance-based methods.

The relevant theory of radiative transfer through an atmosphere is reviewed. The partition of extinction optical depth into Rayleigh, aerosol and absorption optical depths is discussed. The reflectance-based method is described along with the assumptions made. The reflectance-based method accuracy is no better than the measurement of the ground reflectance which is made in reference to a standard of spectral reflectance.

The radiance-based method is described. The standard for the radiance method is a standard of spectral irradiance used to calibrate a radiometer. The calibration of a radiometer is discussed along with the use of radiative transfer computations to correct for the residual atmosphere above the radiometer.

The irradiance-based method is described. It uses the measurement of the downward direct and total irradiance at ground level to determine the apparent reflectance seen by a sensor. This method uses an analytic approximation to compute the reflectance without the use of an "exact" radiative transfer code. The direct-to-total irradiance ratio implicitly gives the description of the scattering normally calculated from the size distribution and assumption of Mie scattering by the aerosols.

The three methods give independent results which should allow for the detection of possible systematic errors in any of the methods. All three methods give results within the estimated errors of each method on most calibration dates. We expect the results of our sensor calibrations are within five percent of the actual value.

CHAPTER I

INTRODUCTION

Imaging sensors operating in the visible and near infrared part of the spectrum have been placed in orbit aboard satellites launched by several nations. The data from these sensors are analyzed with the intent to provide information for scientific studies and inputs to management decisions for natural resource, agricultural and environmental programs. The goal of several space programs is a coordinated, long-term, world scale understanding of the changes in the world environment due to both natural causes and man. Imaging sensors can provide an important input to these programs if the data are of sufficient quality. Image quality can only be assured if the sensors are accurately calibrated.

The quality of imagery is dependent on its resolution and upon stability and repeatability of the data. The data must have spatial resolution good enough that the targets under study can be differentiated. The temporal resolution must be good enough to allow for monitoring at the time scale required by the study. The sensor must also provide the spectral resolution needed to resolve the spectral radiance differences characteristic of the subject under study. Finally, the sensor must be able to provide the radiometric resolution to distinguish features with only slight differences in radiance or reflectance. This spectral and radiometric resolution must be stable and of a known value if repeatable data are to be obtained. Furthermore, if the study needs the absolute value of the radiance, the radiometric resolution and scale must be calibrated in an absolute sense. As these sensors image the earth's surface through the atmosphere, a correction must also be made for the atmosphere.

What type of study might require the absolute value of the radiance at the sensor? Any study that requires the value of the spectral radiance at the earth surface requires both an absolute sensor calibration and a correction for the radiance due to the atmosphere. These

studies might include the determination of surface reflectance, determination of energy balance relationships, and biomass determinations. A stable absolute calibration is required for any long-term study and any study that attempts to use data collected by more than one sensor.

If a sensor is to be used for studies requiring absolute radiance values, several independent, reliable methods should be used for radiometric calibration. Various independent methods should be used for three reasons (Slater, 1988); (1) No single method can be guaranteed to be free of systematic error, (2) a difference between two or more independent methods may help determine the actual change in the sensor causing the calibration change, and (3) a detailed analysis of the differences between two calibration methods may enable one to improve one method for future calibrations. Three types of calibration could include preflight laboratory calibration, on-board calibrator(s), and in-flight calibrations. Each of these three methods is useful but each has limitations. An example of preflight calibration is the illumination of the sensor entrance pupil with the port of a large, uniform integrating sphere source. This sphere source should have selectable radiance levels covering the dynamic range of the sensor. An example of on-board calibrators is the lamp-based internal calibrator carried on the thematic mapper (TM) on Landsat 4 and 5. The light from the lamps is introduced at the focal plane to monitor any change in the response of the detectors and electronics. An example of in-flight calibration is the use of a carefully characterized earth surface site and atmospheric modeling to determine the radiance at the sensor entrance pupil. Another in-flight calibration method is the use of a well calibrated radiometer at the same time as the satellite sensor and in a similar geometry. The resulting radiance value is then corrected for the effect of the atmosphere above the radiometer.

Preflight calibration is necessary to determine the sensor linearity, the spectral bandpass of each channel of the sensor, and the calibration of each channel of the sensor. The output of most imaging sensors of current and future interest is a stream of digital numbers or digital counts, one number per channel per pixel of the image. The radiometric calibration relates the digital number to the average incident radiance in the spectral channel. In order to calibrate the radiometry of the sensor, first the spectral response of each channel must be determined. Once this response function is determined, the spectrally integrated entrance pupil radiance at the sensor can be found as the integral of the product of the spectral response and the spectral output of the calibration source. This radiance should be measured at multiple levels of source brightness spanning the range from sensor noise level to the saturation radiance or the largest radiance expected from a fully illuminated highly reflective ground target. These calibrations should be done in conditions corresponding to the actual in-orbit environment to the maximum extent possible. Even when great care is taken during calibration, various problems still effect the preflight results. The calibration environment is not the same as the alternating sunlit and dark vacuum of space. The spacecraft temperature may vary from calibration conditions. Filters and other optical elements with thin film coatings may shift in spectral characteristics due to outgassing in the film under the vacuum of space. This obviously effects the spectral response of the channels and hence the radiometric calibration. Launch stresses may slightly change the precise alignment of the optics with a possible change in the response. Finally, ageing effects and contamination of the optical surfaces, especially those of the telescope, may change the response from that during the preflight calibration.

In order to determine if any changes from the preflight calibration have actually occurred, some imaging sensors have carried internal calibrators. These calibrators take light from temporally stable sources and inject this "known" irradiance into the optical system at

some point. This internal calibrator signal is then recorded at various times to determine if the sensor response is changing. The TM has an internal calibrator which consists of a series of three lamps and a set of optical fibers to carry the lamp output to a pivoted flag which moves into a position where the focal plane is illuminated by the light from the fibers. The High Resolution - Visible (HRV) sensors carried by the Systeme Probatoire d'Observation de la Terre (SPOT) -1 satellite also have a lamp-based internal calibrator. The HRVs also have a solar-based calibrator which uses fibers to bring in sunlight. The TM calibrator has a major flaw. It can not measure any response change due to the fore-optics of the system. The TM calibrator can only monitor changes in the filters, detectors, and the following electronics. Any spectral shifts in filters or dichroics or response change due to contamination of mirror and other surfaces will be missed. Several studies have shown that a long-term change in response of TM has occurred that was not found by the internal calibrator.

Since both preflight and current on-board calibrations cannot ascertain calibration shifts due to various probable sensor changes, a third methodology must be used if calibrated data are needed. I shall refer to these methods as "vicarious" or in-flight calibration, ie methods that do not use on-board procedures but refer to selected areas of the earth's surface. These methods use modeling of the atmosphere, and measurements of various atmospheric and ground surface parameters, and possibly radiance measurements to predict the radiance at the sensor entrance pupil. With suitable ground targets, these methods should allow for the determination of both ends of the radiometric scale of the sensor, possibly determining if there are system non-linearities, for example a stray light contribution to the signal from the approximately three steradian out-of-field source of the sunlit earth. Various investigators have made in-flight calibrations of various sensors. Schott (1988), Abel, et al (1988), Hovis, et al (1985) and Slater, et al (1987) have described methods using calibrated radiometers

carried by aircraft to some altitude above a ground site and underflying the spacecraft sensor. Slater (1986, 1987) has described a reflectance based calibration method which has been used at several ground sites to calibrate TM, HRV and the Advanced Very High Resolution Radiometer (AVHRR) carried on the NOAA series of satellites. Justus (1988) has described a method to calibrate sensors using overcast cloud layer targets. Other workers have described satellite intercomparisons and balloon-borne experiments.

In this dissertation, I shall describe and compare three in-flight calibration methods. Two methods depend heavily on the accurate measurement of the reflectance of a ground site. The third method uses an instrument calibrated in radiance to measure the radiance above the site at an altitude of 3050 meters (10,000 ft) above mean sea level (MSL). I shall refer to these three methods as reflectance-based, radiance-based, and irradiance-based. The reflectance- and irradiance-based methods both require the accurate determination of the surface reflectance factor of the ground site. The reflectance factor of the site is measured by ratioing the output of a spectroradiometer or multiband radiometer over the site to the output over a reference panel. Both the panel and the site are illuminated by the sun. The reflectance of the reference is determined in a laboratory or field experiment with reference to a pressed polytetrafluoroethylene powder (trade name of Halon[®], manufactured by Allied Chemical Company, identified as type G-80 tetrafluoroethylene resin) standard constructed in accordance with instructions from the National Institute of Standards and Technology (NIST) (Weidner, et al, 1985). The reflectance-based method uses the measured reflectance as an input to a radiative transfer code which calculates the radiance at the top of the atmosphere. Other inputs required by the code are optical depths due to molecular scattering and aerosols, the complex refractive index of the aerosols and the aerosol particle size distribution. The code assumes that the aerosols are spherical and that they are adequately described by an effective refractive index and the Mie solution to scattering.

The scattering solution is corrected for gaseous absorption due to ozone, water vapor, carbon dioxide, and oxygen as appropriate to the spectral channel being calibrated.

The irradiance-based method uses the inputs for the reflectance method along with a measurement of the ratio of the diffuse-to-global downward irradiance at ground level. The ratio is measured over the reference panel. The radiometer measures the global (total) irradiance on the panel and then an opaque parasol is used to block the direct beam so that the diffuse component can be measured. Diffuse-to-global ratios are needed for the zenith angles corresponding to the solar illumination and to the sensor line-of-sight to the target. For a sensor with a nadir view such as TM, this requires an extrapolation of the ratio to an airmass ($m \approx \sec \theta$) of 1.0. This extrapolation becomes a problem at higher latitudes, especially during the winter. The irradiance method attempts to reduce the uncertainty caused by the assumptions made in choosing the aerosol model for the radiative transfer computation.

The reflectance- and irradiance-based methods are not totally independent as they both require the ground surface reflectance. A third method which does not require reflectance is the radiance-based method. In this method, a well calibrated, stable radiometer is carried aloft into the same viewing geometry as the satellite sensor. This radiance is then corrected for the absorption and scattering effects of the atmosphere above the aircraft level. As most of the water vapor and aerosols are in the lower part of the atmosphere, the correction is much smaller than that which would be required if the radiance were measured near ground level. The higher the radiometer is, the smaller the correction will be. In this work, the radiometer was carried to 3050 m MSL as this was the service ceiling of the helicopter available to carry the radiometer. In this method, the limiting factor is the calibration accuracy of the aircraft-mounted radiometer. Other possible problems are registration and

angular pointing accuracy, residual atmospheric correction errors, and logistical problems such as aircraft and airspace availability at the time of the satellite overpass.

In the following chapters, I shall discuss the theory underlying the models used for the calibrations, the methods and results for the laboratory calibrations of the reference panels and radiometer, and the methods and results from the actual sensor calibrations done with the three methods. Finally, I shall discuss the advantages and problems of each method and suggest various steps that might be taken to improve future in-flight sensor calibrations.

CHAPTER 2

RADIATIVE TRANSFER CODES AND MODELS

The absolute calibration of sensors already in orbit by reference to measured ground sites depends strongly on accurate accounting for the effects of the atmosphere. These atmospheric effects are described by appropriate solutions to the equation of radiative transfer or by models of radiative transfer which incorporate simplifying assumptions. In this chapter, I shall discuss the theory behind the numerical solutions of the equation of transfer and some of the dependencies which strongly effect the sensor calibration work.

When light travels through a medium, it may be scattered, absorbed or transmitted. The medium also emits light; the radiant exitance depends on the emissivity and the temperature of the medium. These processes are described by the equation of radiative transfer. The equation is mathematically intractable when scattering is included. There are no known closed form solutions to the full problem. If scattering is removed, as is appropriate for many cases in the infrared in a planetary atmosphere, solutions have been found which can be verified to some extent with measurements. In the case of the visible and the near infrared, however, scattering is a very important contributor to the total radiation field. In this wavelength range, emission by the atmosphere is negligible. Therefore, the solution needed for sensor calibration must include scattering by both molecules and by various particles which I shall refer to as aerosols. The solution must also take into account absorption by any atmospheric constituent such as ozone, oxygen, carbon dioxide, or water vapor.

The theory of radiative transfer uses the work of George Stokes done in 1852 (Chandrasekhar, 1950). He presented a method for describing polarized light which is now referred to as the Stokes vector or parameter. Chandrasekhar realized that the Stokes representation could be applied to the solution of an equation of transfer for a non-

absorbing, Rayleigh-scattering atmosphere that was horizontally homogeneous and divided into plane-parallel layers. His solution consists of a pair of coupled non-linear integral equations which can be solved by iterative numerical methods on a digital computer. These solutions compare well with atmospheric measurements corrected for deviations from Rayleigh scattering. This solution is not useful, however, for other, more complicated scattering processes such as that from aerosol particles. Therefore, other more flexible numerical solutions had to be developed to compute a solution for more realistic cases. Herman and Browning (1965) presented a numerical solution based on a Gauss-Seidel iterative technique and other workers have presented Monte Carlo, successive orders of scattering, and Fourier decomposition methods of solution. The sensor calibration work at the University of Arizona Optical Sciences Center has used the code based on the Herman-Browning method and code based on the successive order method. This sensor work has also used approximate codes that incorporate data from the "exact codes" with various simplifications. All rely on a solution to the basic equation of transfer.

Introduction to Beer's law, the atmosphere, and polarization

When electromagnetic radiation passes through a homogeneous, isotropic material that attenuates some of the radiation, the intensity of the radiation is reduced. This effect was described by Bouguer in 1729 and Beer in 1852 as cited by Dobrowolski (1978). Both of these effects described the transmittance τ as a function of the thickness t of the absorbing material. Bouguer's law is

$$\tau_{\lambda} = 10^{-\alpha_{\lambda} t} \quad (2.1)$$

where α_{λ} is the spectral absorption coefficient. Beer's law is

$$\tau_{\lambda} = 10^{-\epsilon_{\lambda} c t} \quad (2.2)$$

where ϵ_{λ} is the spectral absorption coefficient per unit concentration and c is the

concentration. Bouguer's or Beer's law, when written in the units used in atmospheric physics, are the physical basis for derivation of the equation of transfer.

Figure 2.1 shows the radiative transfer processes that occur in an atmosphere. The incident beam is E_s^0 . The radiation scattered from an infinitesimally small area in the atmosphere is L and it is scattered in a direction Θ from the incident beam. Radiation can also be emitted from an area in the atmosphere. This emission is governed by the Planck distribution and radiance depends on emissivity, temperature and wavelength. Light can also be absorbed from the beam with the energy going to increase the temperature of the atmosphere. Because light is scattered and absorbed from the incident beam, it is reduced in radiance. At the bottom of the atmosphere the irradiance will be E_s .

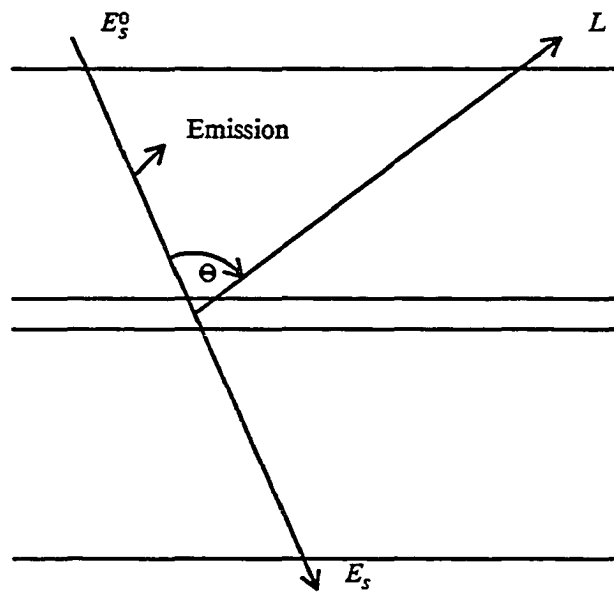


Figure 2.1. Atmospheric processes.

The radiation propagating through the atmosphere is, in general, polarized. To describe the polarization state of the radiation, we need the amplitudes of the electric field components in both orthogonal directions and the phase difference between these components. Let the wave under consideration propagate in the positive z direction with a frequency ω and a propagation constant k . The amplitude of the two components are a_l and a_r and the phases are ξ_l and ξ_r . The two components are then

$$\begin{aligned} E_l &= a_l e^{-i\xi_l} e^{-ikz+i\omega t} \\ E_r &= a_r e^{-i\xi_r} e^{-ikz+i\omega t} \\ \xi &= \xi_r - \xi_l \end{aligned} \quad (2.3)$$

The beam is completely described by the amplitudes and phase difference. For computations of the optical fields, a set of parameters, each member having the same unit of measure is more useful. Since the irradiance of the field is proportional to the square of the field amplitude, Stokes defined four parameters as follows:

$$\begin{aligned} I &= E_l E_l^* + E_r E_r^* \\ Q &= E_l E_l^* - E_r E_r^* \\ U &= E_l E_r^* + E_r E_l^* \\ V &= -i (E_l E_r^* - E_r E_l^*), \end{aligned} \quad (2.4)$$

where $*$ denotes the complex conjugate. Note that $I^2 = Q^2 + U^2 + V^2$ for a completely polarized field and we can define the degree of polarization of a partially polarized field as

$$P = \frac{\sqrt{Q^2 + U^2 + V^2}}{I}.$$

Various manipulations show that

$$\begin{aligned} I &= a_l^2 + a_r^2 \\ Q &= a_l^2 - a_r^2 \\ U &= 2a_l a_r \cos \xi \\ V &= 2a_l a_r \sin \xi. \end{aligned} \quad (2.5)$$

For real fields as seen by real detectors, the quantities I , Q , U , and V are time averages as the detector sees many individual wave trains during any realistic integration period. Another set of parameters which describe the field equally well would be I_l , I_r , U and V . In the scattering calculations, I shall pick the plane containing both the incident and scattered beam as the reference (scattering) plane. Direction l is parallel to the reference plane and r is perpendicular to the plane. If we denote the Stokes vector as I_n and S_{nm} as a matrix of proportionality constants defining the scattering from an incident beam:

$$\begin{aligned}
 I_n^s &= S_{nm} I_m^i \text{ where} \\
 S_{11} &= |S_l|^2 \\
 S_{22} &= |S_r|^2 \\
 S_{33} &= \text{Re} (S_r S_l^*) = S_{44} \\
 S_{34} &= -S_{43} = \text{Im} (S_r S_l^*) \\
 S_{12} &= S_{13} = S_{14} = S_{21} = S_{23} = S_{24} = S_{31} = S_{32} = S_{41} = S_{42} = 0
 \end{aligned} \tag{2.6}$$

when $E_l^s = S_l E_l^i$ and $E_r^s = S_r E_r^i$. These matrix elements are appropriate for the scattering plane and must be transformed if another, more convenient, coordinate system is to be used. For the sensor calibration problem, a better coordinate system will be defined by the plane through the sun and the outward normal to the plane of stratification.

The Equation of Transfer

The equation of transfer depends on the analysis of all components of the radiative field within a wavelength region of interest. Now consider a pencil of light of wavelength λ traveling a distance ds through a medium of density ρ with a mass extinction coefficient of $K_{T\lambda}$. The radiance of this pencil of light is L_λ and the change in radiance is dL_λ :

$$dL_\lambda = -K_{T\lambda} \rho L_\lambda ds. \tag{2.7}$$

The units for ρ are g/cm^3 , for $K_{T\lambda}$ are cm^2/g , for ds is cm and for L_λ is $\text{watts/m}^2\text{-sr-}\mu\text{m}$.

The λ subscript makes explicit the wavelength dependence of the radiance and the

extinction coefficient. The mass extinction coefficient is dependent on both the scattering and absorption in the path ds such that $K_{T\lambda} = K_{s\lambda} + K_{a\lambda}$. The radiance field in an atmosphere varies depending upon the spatial position and the direction of the beam. Therefore, the direction of the incident beam will be given by the polar angles θ and ϕ , where θ is the zenith angle measured from the vertical (z) axis and ϕ is the azimuth angle. The scattered beam direction will be given by θ' and ϕ' . The coordinate system is shown in Figure 2.2. In this figure, the angle ϕ is zero as the sun is in the x - z plane. The beams are of a small angular extent within a differential solid angle of $d\omega$ and $d\omega'$. The angle between

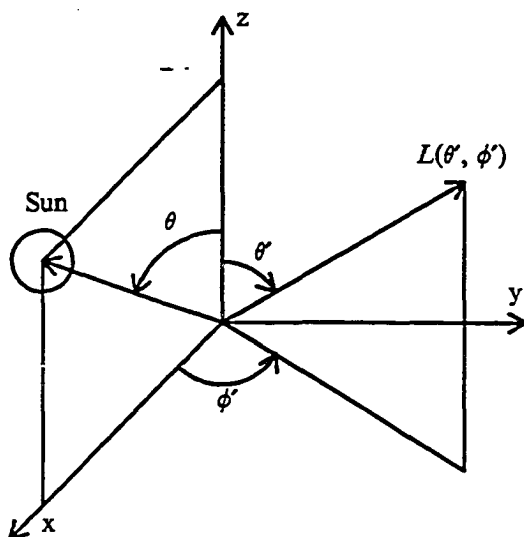


Figure 2.2 Coordinate system and angles.

the incident and scattered beam is called the phase angle Θ . Since we wish to understand the entire radiation field, we must describe the angular distribution of radiance. Hence, for

scattering processes, we define a scattering phase function, $P(\Theta)$, which describes the radiance scattered from $d\omega$ around the direction (θ, ϕ) into $d\omega'$ around the new direction (θ', ϕ') . The two directions are separated by the angle Θ . The integration of the outgoing radiance from a scattering area gives a normalization requirement of $\int_{\omega} P(\Theta) d\omega' = \omega_0 \leq 1$ where ω_0 is the single scatter albedo. For a conservative atmosphere, $\omega_0 = 1$ and the extent to which ω_0 is less than unity is a measure of the aerosol and gaseous absorption of the atmosphere. Other workers have used different normalizations of the phase function, a common one being $4\pi\omega_0$ rather than ω_0 . With this definition of a phase function, we can now write the scattered beam radiance in the direction θ' and ϕ' as

$$P(\theta', \phi', \theta, \phi) L_{\lambda}(\theta, \phi) d\omega'. \quad (2.8)$$

Now, to get an equation of transfer, we must add up the sources of radiation and the sinks. For the sinks

$$dL_{\lambda} = -K_{t\lambda} \rho L_{\lambda} ds$$

and for the sources

$$dL_{\lambda} = j_{\lambda} \rho ds$$

where j_{λ} is the source coefficient due to radiant exitance and scattering into the pencil beam of radiation. Therefore

$$dL_{\lambda} = j_{\lambda} \rho ds - K_{t\lambda} \rho L_{\lambda} ds$$

and

$$\frac{dL_{\lambda}}{K_{t\lambda} \rho ds} = \frac{j_{\lambda}}{K_{t\lambda}} - L_{\lambda} = J_{\lambda} - L_{\lambda} \quad (2.9)$$

where $J_{\lambda} = \frac{j_{\lambda}}{K_{t\lambda}}$. This is the general equation of radiative transfer with no simplifying assumptions or preferred coordinate system. In our description,

$$J_{\lambda} = \int_{\omega} P(\Theta) L(\omega') d\omega' + \frac{E_{\lambda}}{K_{t\lambda}} \quad (2.10)$$

where $E_\lambda \equiv$ emitted energy/mass-time-wavelength-solid angle. In the sensor calibration problem, we have assumed a plane parallel, horizontally homogeneous, steady state medium. Therefore

$$\frac{\partial L_\lambda}{\partial x} = \frac{\partial L_\lambda}{\partial y} = \frac{\partial L_\lambda}{\partial t} = 0$$

and

$$\frac{dL_\lambda}{ds} = \frac{\partial L_\lambda}{\partial z} \frac{dz}{ds} = \frac{\partial L_\lambda}{\partial z} \cos \theta$$

where θ is the zenith angle measured from the outward normal to the plane of stratification. z is measured in the vertical direction. Now with the definitions $\cos \theta = \mu$ and $d\delta_\lambda = -\rho K_{t_\lambda} dz$, $\delta_\lambda = \int_z^\infty K_{t_\lambda} \rho dz$ where $\delta_\lambda \equiv$ optical depth (or thickness) is measured from the top of atmosphere downward. For these assumptions the equation of radiative transfer becomes

$$\mu \frac{dL_\lambda}{d\delta_\lambda} = L_\lambda - J_\lambda \quad (2.11)$$

where the directional dependencies are implied. We now consider the boundary conditions for our problem. At the top of the atmosphere, $\delta = 0$, $-1 \leq \mu \leq 0$ ($\pi/2 \leq \theta \leq \pi$), and $L_\lambda(\delta = 0, -\mu, \phi) = 0$. At the bottom of the atmosphere, $\delta = \delta_t$, $0 \leq \mu \leq 1$ ($0 \leq \theta \leq \pi/2$), and $L_\lambda(\delta = \delta_t, \mu, \phi)$ is some known radiance. At the top, there is also incident solar radiation which is a plane parallel beam, giving an irradiance, not radiance. The contribution to the radiance field is given by $P(\Theta) E_{s_\lambda}^0(\delta_\lambda, -\mu_0, \phi_0)$ where $\mu_0 = \cos \theta_0$ and θ_0 is the solar zenith angle.

Now using an integrating factor $e^{-\delta/\mu}$, we can rewrite equation 2.11 as

$$\mu \frac{d}{d\delta} (e^{-\delta/\mu} L_\lambda(\delta, \mu, \phi)) = -e^{-\delta/\mu} J_\lambda(\delta, \mu, \phi). \quad (2.12)$$

If we want L at some optical depth δ , we integrate the equation from $\delta_1 < \delta$ to δ

$$\int_{\delta_1}^{\delta} \frac{d}{d\delta'} e^{-\delta'/\mu} L_\lambda(\delta', \mu, \phi) d\delta' = -\frac{1}{\mu} \int_{\delta_1}^{\delta} e^{-\delta'/\mu} J_\lambda(\delta', \mu, \phi) d\delta'$$

giving (after multiplication by $e^{\delta/\mu}$)

$$L_{\lambda}(\delta, \mu, \phi) = L_{\lambda}(\delta_1, \mu, \phi) e^{-(\delta_1 - \delta)/\mu} - \int_{\delta_1}^{\delta} e^{-(\delta' - \delta)/\mu} J_{\lambda}(\delta', \mu, \phi) \frac{d\delta'}{\mu}. \quad (2.13)$$

If $\delta_1 \rightarrow 0$, we can bring in the upper boundary condition $L_{\lambda}(0, \mu, \phi)$. Similar reasoning for the upward case gives (with $\delta_2 > \delta$)

$$L_{\lambda}(\delta, \mu, \phi) = L_{\lambda}(\delta_2, \mu, \phi) e^{-(\delta_2 - \delta)/\mu} + \int_{\delta}^{\delta_2} e^{-(\delta' - \delta)/\mu} J_{\lambda}(\delta', \mu, \phi) \frac{d\delta'}{\mu}. \quad (2.14)$$

To bring in the lower boundary conditions, let $\delta_2 \rightarrow \delta_t$ giving $L_{\lambda}(\delta_t, \mu, \phi)$ which, in our case, is due to the reflection of downward radiation by the surface.

Equations (2.13) and (2.14) must be solved at the desired δ for the sensor calibration. When J_{λ} has scattering terms, they cannot be solved analytically as J_{λ} must be known at all values of δ and then integrated. The approach taken by Herman (1963) was to divide the atmosphere into layers of some small $\Delta\delta$ and then evaluate J_{λ} numerically at the midpoint of each layer. Using the output of one layer as the input to the next and iterating through the atmosphere gives a converging solution.

Let us now consider the simplest form of the equation which is when the source term $J_{\lambda} = 0$. There is no emission or scattering. Then

$$L_{\lambda}(\delta, -\mu, \phi) = L_{\lambda}(0, -\mu, \phi) e^{-\delta/\mu} \quad (2.15)$$

for downward beams and

$$L_{\lambda}(\delta, \mu, \phi) = L_{\lambda}(\delta_t, \mu, \phi) e^{-(\delta_t - \delta)/\mu} \quad (2.16)$$

for upward beams. The equation for the downward beam will be important for our determination of the optical thickness of the atmosphere using solar radiometry. The downward equation is the experimentally determined Beer or Bouguer or Lambert Law. This idealization is only useful when δ is small enough that the emission and scattering terms are negligible. This means that the temperature of the atmosphere must be less than that of

the source to make re-emission small at the wavelength in question. Also δ_t must be small enough that

$$\int_0^{\delta_t} J_{scat} e^{-(\delta_t - \delta')} d\delta' \ll L_0 e^{-\delta_t}.$$

For our sensor calibrations, Beer's law is not appropriate as there is a substantial contribution to the upward radiance due to both Rayleigh and aerosol scattering. In our calculations we use separate Rayleigh phase functions and aerosol phase functions. The aerosol phase function is based on the Mie theory of scattering from spherical particles. For both types of scattering, the phase function is dependent on the polarization of the incident beam. Depending upon the optical depths, the wavelength and the bottom boundary condition (the downward field as reflected by the ground), the calculations may or may not require the use of polarization to get the calibration accuracy we desire.

The Phase Function

The phase function for scattering is dependent on the size of the particle causing the scattering. In the limit of a small particle, one whose radius is much smaller than $\lambda/2\pi$, the scattering is adequately described as Rayleigh. For larger particles, the scattering spherical particles is described by equations first derived by Mie (1908). Mie's derivation is appropriate only for spherical particles; for particles of other shapes, the derivation is much more complicated (ellipsoids or cylinders for example) and unknown for irregular particles. In all work in this dissertation, we will assume spherical particles and use the Mie theory.

Rayleigh Scattering

Lord Rayleigh first described scattering by molecules in the atmosphere in 1871. He showed the $1/\lambda^4$ wavelength dependence by making heuristic arguments based on units and possible dependencies. He later made a rigorous derivation based on electromagnetic theory. The starting point for his analysis is the description of the molecule as a small,

homogeneous, isotropic sphere. An incident radiation field E_0 induces a dipole p_0 in the molecule such that $p_0 = \chi E_0$ where χ is the polarizability. This moment modifies the field internal to the molecule and near it. If the incident field is oscillating, the moment also oscillates due to the driving force. Let θ be the angle between the observation point and the dipole and r be the distance from the dipole and the observation point. In this case, the electric field is

$$\mathbf{E} = \frac{1}{c^2} \frac{1}{r} \frac{\partial^2 \mathbf{p}}{\partial t^2} \sin \theta .$$

When the field E_0 is oscillating $\mathbf{p} = p_0 e^{-ik(r-ct)}$.

Solving for \mathbf{E} we can show that

$$\mathbf{E} = E_0 \frac{e^{-ik(r-ct)}}{r} k^2 \chi \sin \theta .$$

Now we decompose this field into two orthogonal components E_l and E_r . With Θ as the scattering angle, we get

$$E_r = -E_0 \frac{e^{-ik(r-ct)}}{r} k^2 \chi$$

and

$$E_l = E_0 \frac{e^{-ik(r-ct)}}{r} k^2 \chi \cos \Theta .$$

In terms of irradiance, the two components are

$$I_r = I_0 \frac{k^4 \chi^2}{r^2}$$

and

$$I_l = I_0 \frac{k^4 \chi^2}{r^2} \cos^2 \Theta .$$

Now if we assume unpolarized incident light and realizing that $k = 2\pi/\lambda$, we get

$$I = \frac{I_0}{r^2} \chi^2 \left(\frac{2\pi}{\lambda} \right)^4 \frac{1 + \cos^2 \Theta}{2} . \quad (2.17)$$

This is the formula derived by Rayleigh. This same wavelength dependence can be derived by solving Maxwell's equations for a medium which has spontaneous fluctuations of density

(Born and Wolf, 1980). Similarly, Rayleigh scattering can be derived using semi-classical quantum optics theory by assuming a two level atom (Sargent, 1985). This formula can also be derived from the general Mie equations for the small particle limit (van de Hulst, 1957).

The scalar phase function for Rayleigh scattering can then be written as

$$P(\cos(\Theta)) = \frac{3}{16\pi} (1 + \cos^2\Theta) . \quad (2.18)$$

Note that there is no polarization dependence in the scalar version of the phase function. For r polarized light, the scattering is isotropic. For l polarized light, the scattering is proportional to $\cos^2\Theta$.

Mie Scattering

The Mie theory describes the scattering by an isotropic sphere of arbitrary size with a radius of r . A nondimensional size parameter α (x for some authors) is usually defined as $\alpha = 2\pi r/\lambda$ to simplify the expressions derived in the theory. The derivation of Mie theory starts with Maxwell's equations and proceeds with the solution of the vector wave equation by assuming a separable solution in spherical coordinates. The complete derivation entails expansion of the solution in Legendre and Bessel functions and matching boundary conditions at the surface of the sphere. As the derivation is complicated and presented in various sources such as van de Hulst (1957), Liou (1980) and Stratton (1941), we will not repeat it here. The Mie solution gives the field components at any point, either inside or outside the sphere. In our case, we are interested only in the far field components outside the sphere. In the far field ($2\pi r/\lambda \gg 1$), an asymptotic expression for the spherical Bessel function is used. In the far field, the radial components of the solution fall off faster than $1/r$ so they are neglected. The tangential components are usually expressed as two scattering functions:

$$S_1(\theta) = \sum_{n=1}^{\infty} \frac{2n+1}{n(n+1)} [a_n \pi_n(\cos\theta) + b_n \tau_n(\cos\theta)] \quad (2.19)$$

$$S_2(\theta) = \sum_{n=1}^{\infty} \frac{2n+1}{n(n+1)} [b_n \pi_n(\cos\theta) + a_n \tau_n(\cos\theta)] \quad (2.20)$$

where

$$\pi_n(\cos\theta) = \frac{1}{\sin\theta} P_n^1(\cos\theta) \quad (2.21)$$

and

$$\tau_n(\cos\theta) = \frac{d}{d\theta} P_n^1(\cos\theta) . \quad (2.22)$$

The functions a_n and b_n are complicated expressions of the Riccati-Bessel functions

$$\psi_n(x) = \sqrt{\frac{\pi x}{2}} J_{n+1/2}(x)$$

and

$$\xi_n(x) = \sqrt{\frac{\pi x}{2}} H_{n+1/2}^2(x) ,$$

the size parameter α , the complex refractive index m , and $y = m\alpha$:

$$a_n = \frac{\psi'_n(y)\psi_n(\alpha) - m\psi_n(y)\psi'_n(\alpha)}{\psi'_n(y)\xi_n(\alpha) - m\psi_n(y)\xi'_n(\alpha)} \quad (2.23)$$

and

$$b_n = \frac{m\psi'_n(y)\psi_n(\alpha) - \psi_n(y)\psi'_n(\alpha)}{m\psi'_n(y)\xi_n(\alpha) - \psi_n(y)\xi'_n(\alpha)} .$$

If we have an incident, normalized electric field, we can decompose it into two perpendicular components

$$E_r^i = e^{-ikz} \sin\phi$$

$$E_l^i = e^{-ikz} \cos\phi$$

and then find the scattered field as

$$\begin{bmatrix} E_l^s \\ E_r^s \end{bmatrix} = \frac{e^{-ikr+ikz}}{ikr} \begin{bmatrix} S_2(\theta) & 0 \\ 0 & S_1(\theta) \end{bmatrix} \begin{bmatrix} E_l^i \\ E_r^i \end{bmatrix} . \quad (2.24)$$

We can also define the so-called intensity functions

$$\begin{aligned}
 i_1(\theta) &= |S_1(\theta)|^2 \\
 i_2(\theta) &= |S_2(\theta)|^2 \\
 i_3(\theta) &= S_2 S_1^* \\
 i_4(\theta) &= S_1 S_2^*
 \end{aligned}
 \tag{2.25}$$

which are used to construct the phase matrix for scattering by a single sphere. The real problem in using Mie theory is the computation of the intensity functions for the appropriate wavelength, size, and scattering angles. The infinite series converge, however the number of terms required increases as α increases. There may also be difficulties with numerical stability in the recursive computation of some of the Bessel functions.

Scattering Cross Section

The scattering cross section is a number with the units of area. If we let the total energy scattered in all directions be equal to the energy of the incident wave falling on an area, the area is defined to be the cross section. The symbol used for the scattering cross section is σ_s . In terms of the phase function $P(\Theta)$, we can define the scattering cross section as

$$\sigma_s = \frac{1}{k^2} \int P(\Theta) d\omega$$

where $d\omega = \sin\theta d\theta d\phi$ and the integral is over all space (4π sr). In the case of Rayleigh scattering, we can show that the scattering cross section is

$$\sigma_{Ray} = \frac{8\pi^3(m^2-1)^2}{3N^2\lambda^4} \tag{2.26}$$

where N is the number of molecules per unit volume and m is the real part of the refractive index of the molecules. This value is correct only for spherical particles; for the real molecules found in the atmosphere a multiplicative correction factor $f(\rho)$ must be applied (Young, 1981).

The factor is

$$f(\rho) = \frac{6 + 3\rho}{6 - 7\rho} \quad (2.27)$$

where ρ is the anisotropic factor. The anisotropic factor results from the variation of the refractive index with direction. This variation means that the polarizability χ is a tensor.

For Mie scattering, the computation of the scattering and extinction cross sections is more complicated. Readers are referred to Liou (1980) or van de Hulst (1957) for derivation of the result that the extinction cross section is

$$\sigma_e = \frac{4\pi}{k^2} \text{Re}\{S(0)\} \quad (2.28)$$

where

$$S(0) = S_1(0) = S_2(0) = \frac{1}{2} \sum_{n=1}^{\infty} (2n+1)(a_n + b_n) .$$

Similarly, the result for the scattering cross section can be shown to be

$$\sigma_s = \frac{\lambda^2}{2\pi} \sum_{n=1}^{\infty} (2n+1)(|a_n|^2 + |b_n|^2) . \quad (2.29)$$

The efficiency factors, usually denoted by the symbol Q with an appropriate subscript, are related to the cross section by the area of the particle, πr^2 . Hence $Q_s = \sigma_s / \pi r^2$ for example. This would be the fraction of the energy passing through an area of πr^2 which is scattered by the particle of that area.

Particle size distribution

The phase functions and scattering cross sections above were computed for a single particle of a given size. A real atmosphere in a collection of particles of varying sizes with a particle density that varies as a function of height. We shall first discuss the variation of size in a given volume of the atmosphere. The term polydispersion is applied to a system of particles with varying characteristics. The most important polydispersion for our atmospheric problem is that of the aerosol particles. The sizes of these particles vary widely. According to Coulson (1988), the smallest aerosol particles that are radiatively effective are

of radius of about $0.04 \mu m$. The largest particles included in a normally occurring polydispersion is taken to be about $10 \mu m$. Thus the particle radii vary by over two orders of magnitude. We obviously need to know the number of particles of a given size in order to compute the radiative effect of the polydispersion. For this purpose we use a statistical distribution function which gives the frequency of occurrence as a function of radius. This function is usually symbolized as $n(r)$ where n is the number density of particles. Several distributions have been proposed to describe the aerosol polydispersion. Some examples are the Junge distribution, the gamma distribution, the modified gamma distribution and the log-normal distribution.

The most commonly used distribution is the Junge distribution (Junge, 1963). It was based on aerosol observations. It is a power law distribution of the form

$$\frac{dn(r)}{dr} = c r^{-(\nu+1)} \quad (2.30)$$

where ν is the so-called Junge fitting factor, c is a factor proportional to the total concentration. In a log-log plot of $n(r)$ versus r , ν is the slope of the curve. The Junge distribution may also be written as

$$\frac{dn(r)}{d(\log r)} = c r^{-\nu} .$$

The normal value for ν is between 2 and 4 according to Liou.

The form of the other standard distributions can be found in references such as Coulson (1988). In making use of the size distribution, we are assuming that the particles are far enough apart that the distance between them is greater than the wavelength. In this case the particles scatter independently and the phases of the scattering are irrelevant. There are no interference effects and the intensities from each scattering particle can be added *without* considering the relative phases. In this case, the cross sections and phase functions for a polydispersion can be computed by integrating the product of the size distribution and the desired parameter over the range of sizes in the polydispersion. We can compute extinction

and scattering coefficients as follows

$$\beta_e = \int_{r_1}^{r_2} \sigma_e(r) \frac{dn(r)}{dr} dr \quad (2.31)$$

and

$$\beta_s = \int_{r_1}^{r_2} \sigma_s(r) \frac{dn(r)}{dr} dr . \quad (2.32)$$

The single scatter albedo for the polydispersion is then

$$\omega_0 = \beta_s / \beta_e . \quad (2.33)$$

The elements of the Mie scattering phase matrix can be similarly integrated over the range of the size distribution to compensate for the range of sizes. The effect of the integration is usually to smooth the variations with angle in the phase matrix. The effect is similar for the scalar phase function used in computations which do not consider polarization.

We now have a description of the size distribution within a small area of the atmosphere. We must also consider the spatial variation of the aerosols. In our work we assume that the same size distribution holds anywhere in the atmosphere. The actual numbers of particles may vary, however, with altitude. The numbers do not vary with horizontal position as we assume a horizontally homogeneous, stratified atmosphere. We use a model of aerosol vertical distribution originally derived by Elterman (1968). This distribution was defined from an average of profiles measured under clear atmospheric conditions over White Sands, New Mexico. This vertical distribution is used in the radiative transfer code to apportion the appropriate amount of aerosol scattering to each layer used in the iterative computation. Similarly, a molecular number density profile is used to apportion the appropriate amount of Rayleigh scattering to each layer. Vertical distributions are also used for ozone and other absorbers as appropriate.

Optical Depth

The spectral optical depth is related to the spectral solar irradiance at the ground $E(\lambda)$ by the relation

$$E(\lambda) = E_s^0(\lambda) e^{-m(\delta_r(\lambda) + \delta_a(\lambda))} T_g(\lambda) \quad (2.34)$$

where $E_s^0(\lambda)$ is the exoatmospheric spectral solar irradiance, m is the airmass (approximately the secant of the solar zenith angle), $\delta_r(\lambda)$ is the optical depth due to Rayleigh scattering, $\delta_a(\lambda)$ is the optical depth due to aerosol scattering, and $T_g(\lambda)$ is the gaseous transmission of the atmosphere. In the range of 0.37 to 1.05 μm , the transmission may be less than 1 because of absorption by atmospheric constituents such as ozone. At the concentrations present in the earth's atmosphere, Beer's law is appropriate for ozone absorption so we can write

$$T_{O_3}(\lambda) \simeq e^{-m\delta_{O_3}(\lambda)} . \quad (2.35)$$

This approximation is appropriate for some other constituents such as NO_2 but not water vapor. Beer's law is for monochromatic radiation. The absorption by water vapor consists of many narrow absorbing lines of varying strength, width, and spectral position. Over a band of radiation, the effect of these lines must be combined by integrating the absorption over all lines. This integration can be done numerically using an atlas of lines for the absorber or by using an appropriate band model and doing the statistical integration. In either case, for water vapor the integration result for transmission is different than that given by Beer's law. Key results are that absorption can saturate and that there are two limiting absorption cases: linear and square root (Liou, 1980). Combining equations 2.34 and 2.35 we can write

$$\log E(\lambda) = \log E_s^0(\lambda) - m(\delta_r(\lambda) + \delta_a(\lambda) + \delta_{O_3}(\lambda) + \delta_{NO_2}(\lambda)) , \quad (2.36)$$

for the wavelength regions where only O_3 and NO_2 absorb. By measuring $E(\lambda)$ as a function

of airmass m , we can determine both $E_s^0(\lambda)$ and $\delta_t(\lambda)$ if $\delta_t(\lambda)$ is constant with respect to m . This is the Langley or Langley-Bouguer technique.

A large component of $\delta_t(\lambda)$ is due to Rayleigh scattering, especially at shorter wavelengths. We must determine this part of the extinction optical depth. The optical depth due to Rayleigh scattering can be shown to be

$$\delta_r(\lambda) = \sigma_s(\lambda) \int_{z_0}^{z_t} N(z) dz, \quad (2.37)$$

where $N(z)$ is the number density of molecules as a function of height, z_0 is the ground elevation, and z_t is the altitude corresponding to the top of the atmosphere. In the case of a downward-pointed sensor on an aircraft, z_t is the sensor altitude used to calculate δ_r for the upward path to the sensor. The variable $\sigma_s(\lambda)$ is the scattering cross section and for unpolarized incident light we can calculate it using equations 2.26 and 2.27:

$$\sigma_s(\lambda) = \frac{8\pi^3(m_r^2 - 1)^2}{3\lambda^4 N^2} \frac{6 + 3\rho}{6 - 7\rho}. \quad (2.38)$$

In this case, ρ is the anisotropy factor and is taken to be 0.0279 (Young, 1981). m_r is the real part of the complex refractive index of the molecules and is close to unity but wavelength dependent. As can be seen from equations 2.37 and 2.38, we can calculate $\delta_r(\lambda)$ if we know the number of molecules. We can compute a reasonably good value for N and hence δ_r from an accurate measurement of the atmospheric pressure at the ground site.

For ozone and other absorbers obeying Beer's law, $\delta_{abs}(\lambda) = N_{abs} K_{abs}(\lambda)$, where N_{abs} is the amount of the gaseous absorber and $K_{abs}(\lambda)$ is the absorption coefficient. We use units of cm-atm (STP) for N_{abs} and $\text{cm}^{-1}\text{-atm}^{-1}$ for K_{abs} . N_{abs} is the total atmospheric column amount.

For the aerosol optical depth, we have assumed that the distribution of aerosol particle size follows the Junge distribution

$$\frac{dn(a)}{da} = C(z) a^{-(\nu+1)}, \quad (2.39)$$

where a is the radius of a spherical particle, $n(a)$ is the number density, ν is the Junge parameter, and $C(z)$ is a factor proportional to the aerosol concentration which is dependent on the height z . This simple and generally realistic distribution was chosen for our calibration work as it appears to adequately describe the aerosols in many cases and it has a very useful mathematical property. If we assume limits on the radius of zero and ∞ , we can show that

$$\delta_a(\lambda) = k \lambda^{-\nu+2}, \quad (2.40)$$

where

$$k = \pi (2\pi)^{\nu-2} \int_{z_0}^{z_t} C(z) dz \int_0^{\infty} \frac{Q_e(\alpha)}{\alpha^{\nu-1}} d\alpha. \quad (2.41)$$

$Q_e(\alpha)$ is the extinction efficiency computed from Mie theory. If the limits of integration for the particle size are not 0 and ∞ , k is not independent of wavelength. If, however, the size limits are taken to be 0.01 to 10 μm , k is independent of wavelength to better than the accuracy of our measurements of $\delta_t(\lambda)$. Atmospheric aerosols are thought to have this range of sizes where we measure spectral optical depths. From equation 2.40 we can see that $\log \delta_a(\lambda)$ versus $\log \lambda$ will give a straight line.

We determine the spectral extinction optical depths $\delta_t(\lambda)$ with a solar radiometer and the Langley plot method. For morning satellite acquisitions, we take measurements from an airmass of about 6.5 until solar noon. We then reduce the data to optical depths at the radiometer wavelengths. If the atmosphere is stable during the entire time covered by measurements, the optical depth is given by the negative slope of the straight-line result of the Langley plot. If the atmosphere is not stable and the radiometer is stable and well-calibrated, the optical depth at any airmass can be computed from a single measurement. The radiometer wavelengths were chosen to avoid absorption bands and lines due to

atmospheric constituents other than ozone, nitrogen dioxide, and the 0.94- μm band of water vapor (Castle, 1985). The Chappuis band for ozone covers the region from about 0.45 to 0.77 μm . Nitrogen dioxide absorbs at wavelengths less than about 0.53 μm . We use the 0.94- μm band of one of our radiometers to attempt to determine the water vapor content of the atmospheric column at the site.

Partition of optical depths by the two-point method

From our determination of extinction optical depth and the calculation of the optical depth due to Rayleigh scattering, we can obtain the residual optical depth δ_{res} due to aerosol scattering and absorption

$$\delta_{res}(\lambda) = \delta_t(\lambda) - \delta_r(\lambda) . \quad (2.42)$$

For wavelengths less than 0.53 μm , we then calculate and subtract an absorption optical depth for nitrogen dioxide. We use the absorption coefficients from Hall and Blacet, 1952, averaged over the radiometer bands and extrapolated to 0.53 μm . We use the nitrogen dioxide columnar amount from the US 1976 model in LOWTRAN 7 (Kneizys et al, 1988). The resulting absorption optical depth is quite small (0.0006 at 0.4447 μm for example) so the correction for this effect is small, probably less than the errors in the extinction measurements. We now assume a Junge size distribution so the aerosol scattering optical depth is of the form of equation 2.40. We select two widely separated radiometer wavelengths that have virtually no absorption optical depth due to ozone (0.4447 and 0.873 μm in this case). The residual extinction optical depth at these wavelengths is then due only to aerosol scattering. From equation 2.40, a provisional value of ν is derived from the slope of the line which connects the optical depths at these two wavelengths in a plot of $\log \delta_a(\lambda)$ vs $\log \lambda$. A value of k can also be derived from the equation of the line. We calculate a first approximation of the aerosol optical depths at each radiometer wavelength and then

calculate the optical depth due to absorption as

$$\delta_{abs}(\lambda) = \delta_{res}(\lambda) - \delta_a(\lambda) . \quad (2.43)$$

In the case of well-chosen radiometer wavelengths, this $\delta_{abs}(\lambda)$ should be due only to ozone (or water vapor in the 0.94- μm band). If we know the ozone absorption coefficient in the bandpass of the radiometer, we can compute an amount of ozone. At this point we have a provisional value for the Junge parameter, the Rayleigh optical depths, an estimate of the aerosol optical depths, and an estimate of the columnar amount of ozone and the corresponding optical depths. We choose the amount of ozone computed in the radiometer band with the largest absorption coefficient as the columnar ozone amount. This method, referred to as the two-point method, was previously described by Kastner (1985) and other workers. It is sensitive, however, to any errors in the measurement of spectral optical depths, especially at the two widely separated wavelengths. Errors can give high or low values for the Junge parameter ν and erroneous values for the ozone concentration. During our calibration work we have collected extinction data sets that gave suspect values for ν and the amount of ozone using the two-point method.

Iterative partition

The iterative method starts with the two-point method results. It, however, uses all of the data points in order to reduce the errors. If we use our two-point value of the ozone concentration to compute the ozone optical depth at the radiometer wavelengths, we can derive a new estimate of the spectral aerosol optical depths at all radiometer wavelengths except the water vapor band (if present in our radiometer). We then fit a straight line through all points except the water vapor band, with a weighted least squares technique. The weighting is based on the estimated error in the measured extinction optical depth appropriately scaled for log-log space. This multiple-point fit gives a new estimation of ν and k . We now use these to recompute $\delta_{abs}(\lambda)$ and the ozone amount. We iterate this

procedure until both the Junge parameter and the ozone amount converge. This method takes into account the estimated errors in the measurement of the extinction optical depths. On days that the size distribution is not adequately described by the Junge distribution, the straight line fit will give δ_a outside the estimated errors and a different method must be used.

If a Junge distribution is not appropriate or the aerosols do not cover our normal size limits, a straight line in log-log space is not the correct functional form. A small deviation from a Junge distribution can be adequately described in log-log space by the ad hoc choice of a quadratic function. On certain days, a quadratic allows a fit of the data within estimated errors where a straight line does not. This empirical fit does not, however, correspond to any analytic form of the size distribution known to the author. Hence, the values given by the quadratic fit require an inversion of the size distribution, which will not be discussed here.

Now we have analytic expressions for the Rayleigh optical depth and the aerosol optical depth as a function of wavelength and values for the Junge parameter and the ozone amount. We can now compute the optical depths needed for atmospheric correction for any sensor wavelength within the range of our measurements.

Verification of the Iterative Method

We have used both the iterative method and the two-point method to partition synthetic extinction optical depth data. We have generated groups of 100,000 data sets with a known Junge parameter, specified aerosol and Rayleigh optical depths, US 1976 model nitrogen dioxide amount, and specified ozone amount. The aerosol optical depth was computed from the optical depth at $0.55 \mu\text{m}$ and the Junge parameter ν using a power law:

$$\delta_a(\lambda) = \delta_a(0.55) \left[\frac{\lambda}{0.55} \right]^{2-\nu} .$$

Gaussian noise with a standard deviation of a given fraction σ of the aerosol optical depth was added:

$$\delta_a^n(\lambda) = (1 + \sigma * RV) \delta_a(\lambda) ,$$

where RV is a normally distributed random variable with a standard deviation of one. The Rayleigh, aerosol (δ_a^n), nitrogen dioxide, and ozone optical depths were added to form the extinction optical depth. Each of the 100,000 sets was analyzed by the two-point method and the iterative method. Data sets were generated for standard deviations σ of 0.01, 0.02, 0.05, and 0.1 with the aerosol optical depth at 0.55 μm of 0.01, 0.02, 0.05, 0.1, 0.2, and 0.3. The ozone amount was set at 0.3 cm-atm (STP). The Junge parameter was set at 3.0. The outputs (ν and amount of ozone) of all the data sets were averaged for the two methods and the standard deviations were found. The number of data sets in each group was large so that the results are constant to the precision presented irrespective of the starting point in the sequence of pseudorandom numbers used to generate the optical depth.

The simulation results are summarized in Table 2.1. The iterative method fails in a few cases in each group for large standard deviation and optical depth inputs. The failure mode is a derived ozone amount less than 0. This failure occurs only where the errors in the extinction optical depth are greater than one would expect from an accurate solar radiometer's actual extinction measurements. Certain cases with large standard deviations also cause the two-point method to give a Junge parameter of less than 2 or a negative ozone amount, which are obvious errors. The iterative method gives an average Junge parameter and ozone amount closer to the known values than the two-point method and the standard deviation is lower. The standard deviations of the Junge parameter for various levels of noise versus the optical depth are plotted in Figure 2.3 for the iterative method. The standard deviations of the amount of ozone for various levels of noise versus the optical depth are plotted in Figure 2.4 for the iterative method. The two-point method gives

Table 2.1. Errors and standard deviations for the two-point and iterative method simulation.					
δ_a (550 nm)	0.01	0.02	0.05	0.1	0.2
input Std. dev.					
Two-point method					
0.01	-4.5±0.7	-2.3±0.7	-0.9±0.7	-0.5±0.7	-0.2±0.7
0.02	-4.5±1.3	-2.3±1.4	-0.9±1.4	-0.5±1.4	-0.2±1.4
0.05	-4.6±3.4	-2.3±3.4	-1.0±3.5	-0.5±3.5	-0.3±3.5
0.1	-4.6±6.8	-2.4±7.0	-1.0±7.0	-0.5±7.1	-0.3±7.1
Iterative method					
0.01	0.0±0.4	0.0±0.4	0.0±0.4	0.0±0.4	0.0±0.4
0.02	0.0±0.8	0.0±0.8	0.0±0.8	0.0±0.8	0.0±0.8
0.05	0.0±1.9	0.0±1.9	0.0±1.9	0.0±1.9	N/A
0.1	0.0±3.8	0.0±3.8	0.0±3.8	N/A	N/A
Both values are given as percentage (error = (known - mean) * 100 / known). N/A means not applicable as both methods failed in a few cases.					

similar results with a larger standard deviation for the Junge parameter. The two-point method gives nearly the same (slightly larger) standard deviation for the amount of ozone. For small aerosol optical depths, there is a systematic error in the computation of the Junge parameter by the two-point method due to the erroneous assumption of no ozone absorption at 0.44 μm . Ignoring the effect of nitrogen dioxide causes an additional, but smaller (0.6%) error in the Junge parameter.

In general, the iterative method gives (on average) a more accurate estimation of the Junge parameter. The standard deviation is lower. The simulation also shows that the

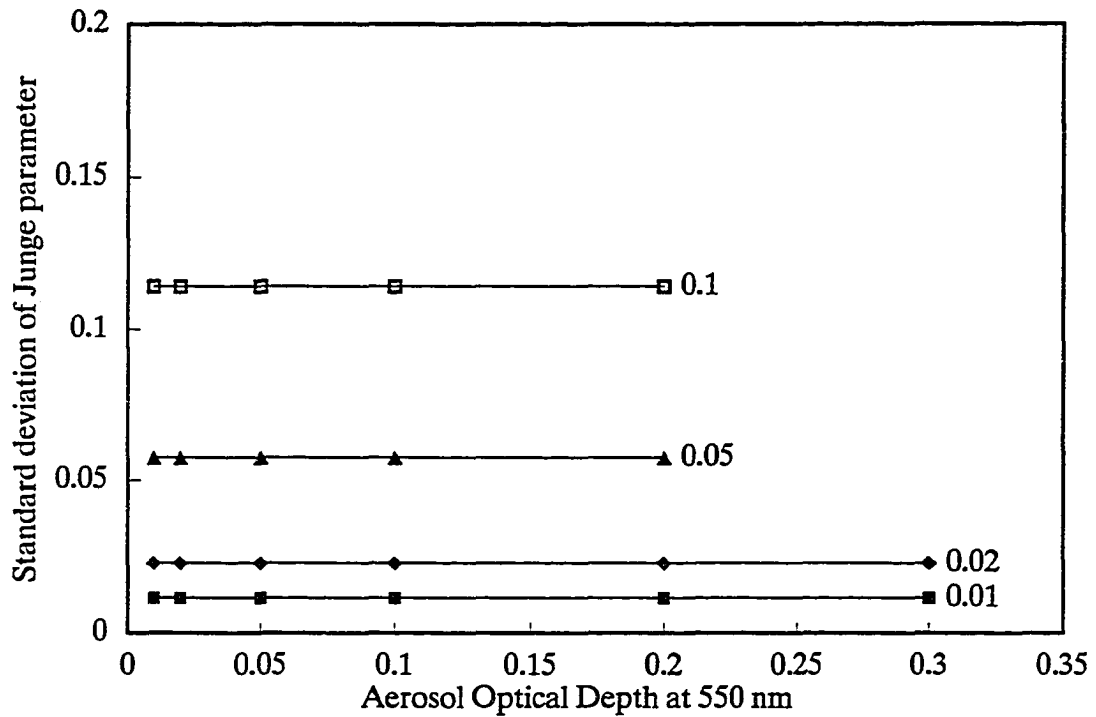


Figure 2.3. Standard deviation of the Junge parameter from simulation

determination of the amount of ozone from radiometer extinction measurements is difficult. Confidence in the inversion of ozone amount from radiometer measurements is restricted by the errors in those measurements. The acceptable error level depends on the actual ozone amount and on the aerosol optical depth. For example, a 95% confidence that an inverted ozone amount is within 20% of the actual amount requires a radiometer error of less than 4% (at an optical depth of 0.1 and ozone amount of 0.3 cm-atm). The iterative method improves the determination of ozone only a very small amount (about 1%) in comparison with the two-point method.

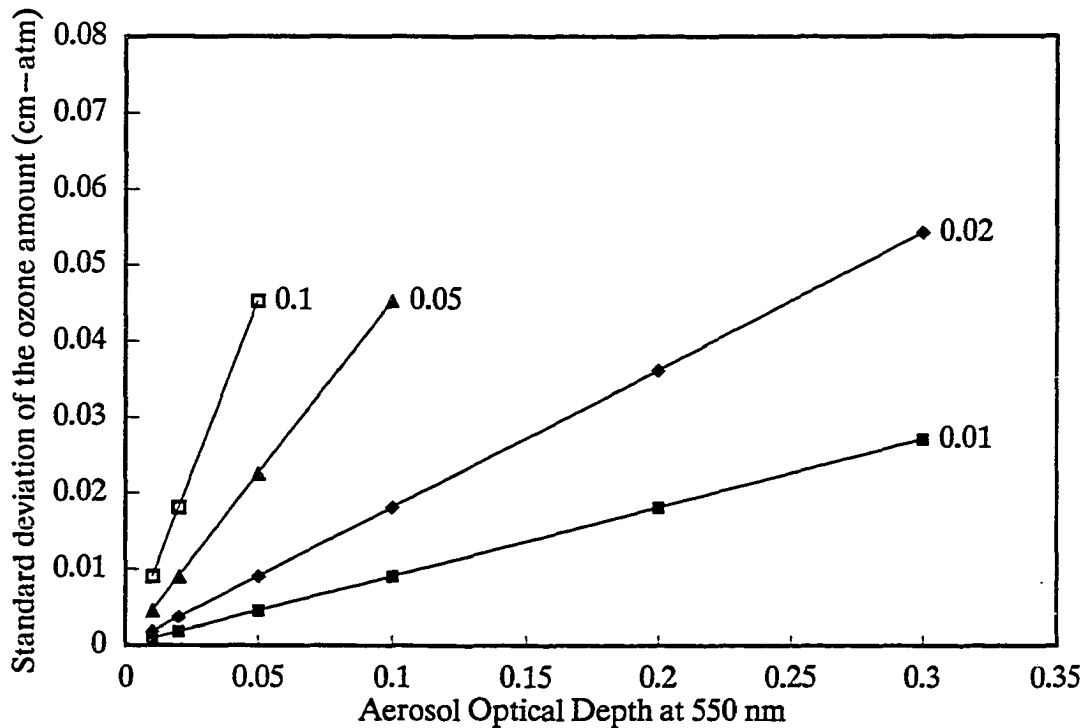


Figure 2.4. Standard deviation of the ozone amount from simulation

The radiative transfer codes

Boundary conditions

To solve the transfer equation, we must know the boundary conditions at the top of the atmosphere and at the bottom. At the top, the downward radiance is zero as there is no source. The source of radiant energy is the solar irradiance at the top of the atmosphere. We assume that we know the solar spectral irradiance from data like that found in Iqbal (1983) corrected for the appropriate earth-sun distance. The upward radiance at the top of the atmosphere is an unknown that we wish to find. At the bottom of the atmosphere, we must specify the upward radiance. This radiance is determined by the reflectance characteristics of the surface. In our satellite calibration work, we have assumed that the

ground is a lambertian reflector with a spectral reflectance which we measured. Hence, the upward radiance at the bottom of the atmosphere is isotropic and of the value $L = \rho E/\pi$ where E is the total irradiance on the surface.

Solution strategy

The transfer equations 2.13 and 2.14 cannot be solved analytically when the phase function is complicated as is the case for Mie scattering. The Mie solution is considered to be the simplest approximation which can yield realistic results for a planetary atmosphere. Therefore, some numerical scheme must be used to solve the equations with the given boundary conditions. In our satellite calibration work using the reflectance-based method, we have used a numerical code originally developed by Herman and Browning (1965). We have used a different code developed by Deuzé (1974) for our irradiance-based method. Both of these codes are "exact" codes that compute a numerical solution at a net of points in space. They both include both Rayleigh and Mie scattering. Both assume a plane parallel stratified atmosphere that is horizontally homogeneous and a lambertian bottom boundary condition. Both codes compute the phase matrix (or function for the scalar case) using a specified size distribution with given size limits. We have assumed that the size distribution is Junge. For the Herman and Browning code, we have used size limits of 0.01 to 10.0 μm with an integration step size of 0.01 μm . For the Duez  code, the size limits are normally specified by the size parameter α and the limits are 0.05 to 200. The large limit extends beyond 10 μm for the wavelengths we use. The differences in the phase function due to the few large particles is small. The major differences between the two codes are the method for integrating the azimuthal direction. The Herman and Browning code uses finite differences in θ and ϕ and uses a Gauss-Seidel numerical integration. The Duez  code uses a Fourier series decomposition of the radiance and phase matrix and then uses an analytic integration in ϕ . This integration is possible because of the orthogonal properties of the

Fourier series. Both codes have been developed in versions that use a phase matrix and compute the Stokes parameters of the radiation field and in versions that use a phase function and compute only the radiance.

Herman and Browning code

The Herman and Browning code uses finite differences. In our work we have used a $\Delta\phi$ of 30 degrees and a $\Delta\theta$ of 10 degrees. In this method, the phase matrix and radiance terms are computed at the midpoint of the interval and that value is used as the average over the interval. This average value is pulled outside the integral. The integral then becomes a sum and the scattering component can be computed. This computation starts at the top layer of the atmosphere and progresses down to the bottom. For the first pass through the atmosphere, the upward radiance is assumed zero as it is unknown. The downward radiance exiting a layer is used in the computation for the next layer. After one full iteration, a first approximation of the radiance field in both the upward and downward directions has been computed. This is now used for a second pass. This process is continued until the fields converge. We have selected a change of less than 0.5% as a convergence criteria. In order for this method to converge reliably, the optical depth in each layer must be small enough that most of the scattering is single scattering. This means that the source term is essentially constant over the layer. Herman chose a layer thickness of $\Delta\delta = 0.02$ which means that about 96% of the scattering is associated with a single event. This gives a good compromise between many layers and many passes.

The Herman and Browning code can run in a scalar or a polarization form. We have used the scalar version for most of our work as it runs much more quickly and gives nearly the same value for the radiance. The aerosols and multiple scattering tend to depolarize the radiance field so the scalar code is appropriate for our work. In the case of an

extraordinarily clear atmosphere dominated by Rayleigh scattering, polarization would give a more accurate computation.

Deuzé code

The Deuzé code is a successive order of scattering code that uses a Fourier series decomposition in azimuth of the fields. As a first step, all the Fourier coefficients for the phase matrix are computed for a given index for size parameters varying from 0.05 to 200.0. During the next step, the integration over the size distribution is done. The phase matrix is determined at the appropriate angles for 80 point Gaussian quadrature and at 0, 90, and 180 degrees. The third step is the actual radiative transfer computation. The atmosphere is divided into 25 plane parallel layers. The first order of scattering is the primary scattering from the solar beam. The estimate of the n times scattered light is computed from the $n-1$ times scattered light. The radiance is computed at discrete points in θ corresponding to the Gaussian angles. The θ integration is by Gaussian quadrature. The ϕ integration is analytic. The number of terms in the Fourier series depends on the type of scattering and the range of the size parameter. For Rayleigh scattering, only three terms are needed to completely specify the phase matrix. For aerosols, the number of terms depends on the geometry and on the size parameter and it may vary between about 30 and 65. The fourth step is the summing of the Fourier series to obtain the radiance in a specified direction.

The Simulation of the Satellite Signal in the Solar Spectrum (5S) approximate code

Tanré et al (1986) developed an approximate code that uses an analytic approximation to compute both scattering and absorption in the earth's atmosphere. We modified this code to allow computations for ground elevations other than sea level and for sensor altitudes other than space. 5S computes the absorption effects of water vapor, carbon dioxide (CO₂), oxygen (O₂), and ozone. It uses random exponential band models: Goody (1964) for water vapor and Malkmus (1967) for the other three. We use this code to compute the effects of

gaseous absorption in the sensor bands for our calibrations. 5S computes at 5 nm intervals through the sensor band or at a monochromatic wavelength. We use the band integrated values for absorption. 5S also makes some analytic approximations to calculate the aerosol scattering. We do not use these results in our reflectance-based method. The approximations are not valid for large angles. We do use some 5S computations in the irradiance-based method.

CHAPTER 3

REFLECTANCE MEASUREMENT AND THE REFLECTANCE-BASED METHOD

It is necessary to know the reflectance factor of target materials for various remote sensing applications. For example, in the reflectance-based method we need to accurately know the spectral reflectance factor of the ground target, normally the gypsum sand at White Sands. In many cases the reflectance is determined by reference to a calibrated field reflectance standard. The standard is usually either a painted BaSO_4 panel or a pressed Halon[®] panel. Spectralon[®], a new reflectance material made by Labsphere can also be used. In order to use these panels to accurately determine the reflectance of the target, the standard panels must be calibrated because they are not perfectly lambertian reflectors. Because these panels are used with a nadir viewing angle under varying conditions of illumination (the solar zenith angle changes during the period of observations), the directional reflectance factor of the panels must be determined.

Once the reflectance factor of the ground surface is determined, we can use the reflectance along with atmospheric parameters to compute the radiance in or above the earth's atmosphere. In this chapter I shall describe a laboratory facility for the calibration of field reflectance standards, illustrate the determination of the atmospheric optical depths, and briefly describe the reflectance-based method of sensor calibration.

Reflectance Panel Calibration

Ideally, a reflectance panel should be calibrated using the same source and sensor that will be used for field measurements. Indeed, a field calibration method was recently reported (Jackson et al, 1987). However, the field method requires clear skies and constant atmospheric conditions during the measurement period. The scheduling of calibrations is thereby controlled by the weather, and not by the needs of the investigator. Calibrations made in a laboratory setting are not subject to these constraints and, in most cases, the

illumination and measurement geometry can be held to considerably higher accuracies. A laboratory facility and methodology for calibrating reference reflectance standards is presented in this chapter.

The reflectance panel calibration apparatus is also used for the calibration of portable radiometers. If a calibrated reflectance panel is mounted on the apparatus at an accurately known distance from a standard source of spectral irradiance, the panel provides a surface of known spectral radiance. Voltage outputs from a portable radiometer can then be associated with the spectral radiances within each band of the radiometer when the integrated relative spectral response across each band has been independently determined.

Calibration Facility and Methodology

Equipment and fixtures

Three fixtures comprise the laboratory set up. The first is an L-shaped arm which supports the radiometer. The arm has an interchangeable mount to accommodate different radiometers. It held the center of the radiometer's entrance pupil 50 cm away from the center of the panel and it aligned the radiometer's optical axis in the plane containing incident illumination beam and the panel normal.

The second fixture is the panel holder. It kept the panel's front surface coincident with the vertical axis of rotation of the stage. The panel can be as large as 24 inches on a side. The entire set up was aligned by securing a mirror to the empty panel holder and placing a laser behind the source so that its beam coincided with the optical axis of the illumination source.

The lamp that provides illumination and its holder are the third fixture, which is mounted to a table. The holder allows three orthogonal translations, two orthogonal tilts and a rotation of the source. A large vertical screen with a circular aperture of 3-cm diameter restricts illumination to the center of the panel. Figure 3.1 is a block diagram (not to scale)

of the equipment layout. Both the arm and the panel holder are fastened to a rotary stage; the stages are stacked with the base of the top stage fastened to the rotating platform of the bottom stage. The base of the bottom stage is rigidly fastened to the same table as the lamp holder. All the elements were made of aluminum. They were anodized and/or painted flat black to reduce stray reflections.

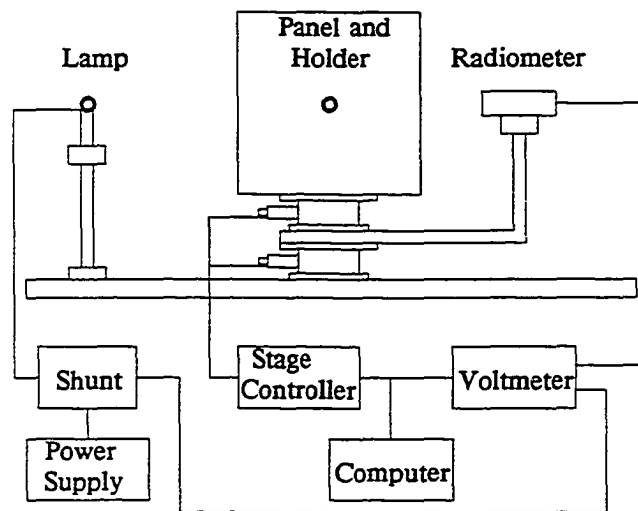


Figure 3.1. Reflectance measurement layout.

Motion control and data acquisition

Angular scanning in both incidence and viewing angles was controlled by two rotary positioning stages featuring resolution of 6 arc sec and absolute accuracy on the order of 0.5 arc min. Stepping motor and stage control were provided by a microprocessor-based controller. The stages, motors and controller were supplied by Aerotech. The accuracy of the angular alignment of the system was estimated to be better than ± 0.1 degree.

The apparatus does not use a chopper, because certain field radiometers such as the Exotech do not have provisions for chopping. Therefore, a high accuracy digital voltmeter

was used to measure the radiometer output. The voltmeter used was a Hewlett Packard Model HP3457A, chosen because it offers good AC line rejection, measurement speed, resolution, accuracy, and remote programming via an external computer. The data acquisition and motion control was commanded by an IBM personal computer running PC-DOS configured with an IEEE-488 interface. Control and analysis software was written in the C language.

Radiometer and source

Two radiometers were used in the laboratory for panel calibration. The first was a locally manufactured instrument provided with six manually interchangeable spectral filters on the front. The band center wavelengths were 0.45, 0.50, 0.55, 0.65, 0.75 and 0.85 μm . Other 25-mm diameter interference filters can also be used. This radiometer had a nominal 1-degree full FOV and a silicon detector.

The second radiometer was a four-band, silicon detector radiometer with internal filters which simulate the first four Thematic Mapper (TM) bands. It was a model 100AX hand held radiometer made by Exotech Incorporated. It is approximately 5 x 5 x 8.5 inches in size and weighs about 5 pounds. Other available internal filters simulated the three SPOT or four Landsat MultiSpectral Scanner (MSS) spectral bands. The internal filters can be removed and external filters fitted for other bandpasses. Large square filters from the same batch used in the flight HRV instruments have been used with this radiometer for the radiance method measurements. This radiometer is normally used for field ground-reflectance measurements and radiance measurements made from aircraft. The FOV is either 1 or 15 degrees. The 1-degree FOV was used for the panel calibrations and the radiance-based method. The radiometer holder was designed such that any one of the four detector apertures was aligned with the equipment axis.

The radiometer fixture can also hold a Barnes Engineering Company Modular Multispectral 8-channel Radiometer (MMR). Although the MMR has not been used for panel calibrations, one has been calibrated in radiance units using this equipment (Markham and Wood, 1988). The MMR is a portable, battery operated instrument containing eight independent, optically chopped radiometers. It was originally designed to measure the reflectance of agricultural crops. It measures about 9 x 10 x 11 inches and weighs about 14 pounds. All 8 channels have parallel optical axes and they are arranged in a circle. The instrument simulates the seven TM bands and has one extra band at 1.15 to 1.3 μm in the SWIR. The bands corresponding to TM1-TM4 have silicon detectors. The 3 bands in the region between 1.15 and 2.35 μm have lead sulphide (PbS) detectors and the thermal band has a lithium tantalate (LiTaO_3) pyroelectric detector. The FOV of each channel can be 1 or 15 degrees.

The sources are FEL or DXW type, 1-kW quartz halogen lamps, powered by two Hewlett Packard 6274B DC power supplies connected in an autoserries constant current configuration. The lamp current is monitored by measuring the voltage across a precision 0.01 ohm shunt from Leeds and Northrup.

Noise and integration time

The HP3457A has programmable integration time. To ensure a good compromise between measurement time and noise rejection, three sets of 100 measurements, at integration times of 1, 10 and 100 power line cycles, were made. The 10 power line cycles integration time gave the lowest standard deviation, probably due to an interaction between integration time and variation in lamp output due to lamp current drift over the total measurement period. This is illustrated in Table 3.1.

Table 3.1. Integration time versus standard deviation

Power line cycles	1	10	100
Output (volts)	3.243	3.248	3.247
σ (volts)	0.0028	0.0012	0.0013
elapsed time (sec)	19	55	416

In order to determine how sensitive the irradiance was to variation in the lamp current, the radiance of the Halon[®] with normal illumination was measured 10 degrees from the panel normal, while the current through the lamp was varied from 7.5 to 8.45 amps. At a current of 8.0 amps, a variation of 0.001 amps resulted in a calculated change of 0.0125% in the radiometer voltage. Maintaining this low error in current appears reasonable unless the AC line supply varies significantly.

Halon[®] reference

For each set of measurements, a freshly pressed Halon[®] panel 10.8 cm in diameter and 1 cm thick was made in the laboratory following the procedures outlined by Weidner et al (1985). It was smaller than the BaSO₄ panel and because of the non-ideal out-of-field rejection characteristics of the radiometer, attention had to be paid to the area surrounding the Halon[®]. For this reason a hole the size of the Halon[®] panel was cut in the center of a BaSO₄ panel, and the Halon[®] was placed within the surrounding BaSO₄ panel whenever the Halon[®] panel was measured as the standard. This procedure minimized the out-of-field problem.

Derivation of Directional Reflectance Factor

According to Hsia and Weidner (1981) the hemispherical reflectance factor (R_R^h) of a material (Halon® in this case) may be calculated for normally incident light from the angular variations of the reflectance factor [$R_R(0^\circ; \theta)$]:

$$R_R^h = \frac{\int_0^{\pi/2} R_R(0^\circ; \theta) \cos\theta \sin\theta \, 2\pi \, d\theta}{\int_0^{\pi/2} \cos\theta \sin\theta \, 2\pi \, d\theta} . \quad (3.1)$$

Dividing by $R_R(0^\circ; 45^\circ)$, Equation 3.1 can be written as:

$$\frac{R_R^h}{R_R(0^\circ; 45^\circ)} = 2 \int_0^{\pi/2} \frac{R_R(0^\circ; \theta)}{R_R(0^\circ; 45^\circ)} \sin\theta \cos\theta \, d\theta . \quad (3.2)$$

In terms of measurable quantities, Equation 3.2 can be rewritten as:

$$\frac{R_R^h}{R_R(0^\circ; 45^\circ)} = 2 \int_0^{\pi/2} B(0^\circ; \theta) \sin\theta \cos\theta \, d\theta \quad (3.3)$$

where

$$B(0^\circ; \theta) = \frac{\Phi(0^\circ; \theta)/\cos\theta}{\Phi(0^\circ; 45^\circ)/\cos(45^\circ)} \quad (3.4)$$

with Φ as the reflected flux from the sample. $B(0^\circ; \theta)$ can be approximated by a polynomial of order N in θ :

$$B(0^\circ; \theta) = \sum_{i=0}^N b_i \theta^i . \quad (3.5)$$

Inserting Equation 3.5 into Equation 3.3, the result becomes a summation:

$$\frac{R_R^h}{R_R(0^\circ; 45^\circ)} = 2 \sum_{i=0}^N b_i I_i \quad (3.6)$$

where

$$I_i = \int_0^{\pi/2} \theta^i \sin\theta \cos\theta d\theta. \quad (3.7)$$

The integrals I_i can be computed by recursion after I_0 and I_1 are found. The recursion was developed from the general I_i integral from Gradshteyn and Ryzhik (1980). The recursion relation is based on integration by parts and is

$$I_i = \frac{(\pi/2)^i - i(i-1) I_{i-2}}{4} \text{ for } i \geq 2. \quad (3.8)$$

With the measurement results fitted to the N th order polynomial, Equation 3.6 was solved for $R_R(0^\circ; 45^\circ)$. Then $R_R(0^\circ; \theta)$ was calculated from the angular measurements as described in the following sections.

Experimental Procedure and Results

Procedure

Before a measurement was made, the screen aperture in front of the source and the radiometer entrance aperture were covered and a reading was taken to determine the input offset voltage of the amplifier. This dark value was as high as 0.4% of the smallest signal (at 450 nm).

The Halon[®] panel was measured at six wavelengths (450, 500, 550, 650, 750, 850 nm) and angles between 10 and 80 degrees at 5 degree intervals. One hundred readings were taken at each position and averaged. The dark value was subtracted from the average. The voltages were converted to $B(0^\circ; \theta)$ using Equation 3.4. The $B(0^\circ; \theta)$ were fitted by the least-squares method to a fifth-order polynomial. Due to symmetry considerations, the first derivative of the fit was constrained to zero at zero degrees view angle with normal illumination. An individual datum did not deviate from the fitted curve by more than 0.001 and was normally within ± 0.0002 . Figure 3.2 shows a typical fit of data for Halon[®] at $\lambda = 450$ nm. $R_R(0^\circ; 45^\circ)$ was calculated from the measurements and the NBS published value (Weidner et al, 1985 and Weidner and Hsia, 1981) of R_R^h according to Equation 3.6.

$R_R(0^\circ; \theta)$ was then calculated from a set of voltages at different angles. Reflectance factors for all six wavelengths decreased with increasing incidence angle and were nearly independent of wavelength, the largest decrease being at $\lambda = 850$ nm for angles greater than 75 degrees. The data demonstrate the non-lambertian properties of the pressed Halon[®].

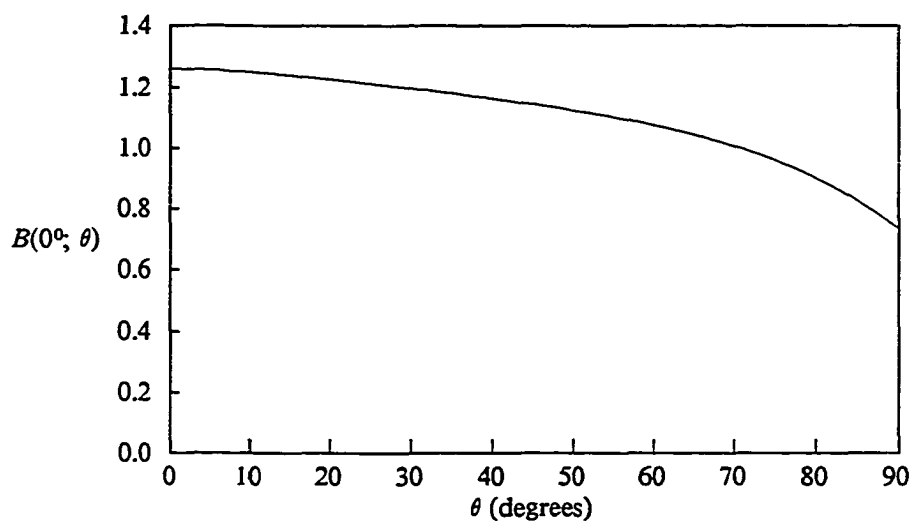


Figure 3.2. Fitted B coefficient for Halon[®].

The measurements for a single Halon[®] panel were made five times under the same conditions. They were made within two days of pressing to reduce possible effects due to aging of the Halon[®]. The panel was also covered between measurements by a stainless steel cover to minimize contamination due to dust and other airborne particles. The results were very consistent. The mean value of $R_R(0^\circ; \theta)$ was calculated for each incident angle and the difference from the mean was computed. For $\lambda = 450$ nm, the maximum departure was less than ± 0.002 but was typically within ± 0.0001 . At $\lambda = 850$ nm, the range of differences from the mean was lower than ± 0.00035 . These variations are much smaller than the accuracy of the hemispheric reflectance of Halon[®].

BaSO₄ panel calibrations

The data for the BaSO₄ panel were acquired in the same way as for the Halon[®] panel. The BaSO₄ panel was measured just before or after the Halon[®] reference with the lamp lit at a constant current during the panel change. The bidirectional reflectance factor (BRF) at a particular angle, θ , was found by ratioing the flux (voltage) from the BaSO₄ panel with that from the Halon[®] panel and multiplying by the Halon[®] directional reflectance for that angle.

Three reference panels, numbered #1, #2 and #3 for identification purposes, were calibrated in August 1987. They were constructed at the Optical Sciences Center Infrared Laboratory by Che Nianzeng. The procedures in painting the three BaSO₄ panels were similar to the procedure outlined in by Robinson and Biehl (1979).

Values of $R(0^\circ; \theta)$ for panel #2 for the six wavelengths and for $10 \leq \theta \leq 80$ degrees are shown in Figure 3.3. BRFs decrease with increasing incidence angle for all wavelengths. The shape of the curves is similar. BRFs for the other two panels, not given here, differ from #2. BRFs for panels #2 and #3 are substantially similar to each other whereas they differ from #1. Panels #2 and #3 are less reflective at small incidence angles and their reflectance factors decrease more slowly with incidence angle.

A comparison between painted BaSO₄ panels for a wavelength of 450 nm is shown in Figure 3.4. At $\lambda = 450$ nm panels #2 and #3 are essentially identical. However, #2 has a higher reflectance than #3 at low incidence angles ($\theta \leq 30$ degrees) and lower reflectance at the high angles. The BRFs are greater than 0.85. Reflectance factors for panel #1 differ considerably from the other two. They are higher at low angles and decrease rapidly with increasing incident angles. For other wavelengths, the trend is the same.

Although the panels were painted by the same person using the same procedure, materials, and equipment, reflectance differences are observable. This emphasizes the need

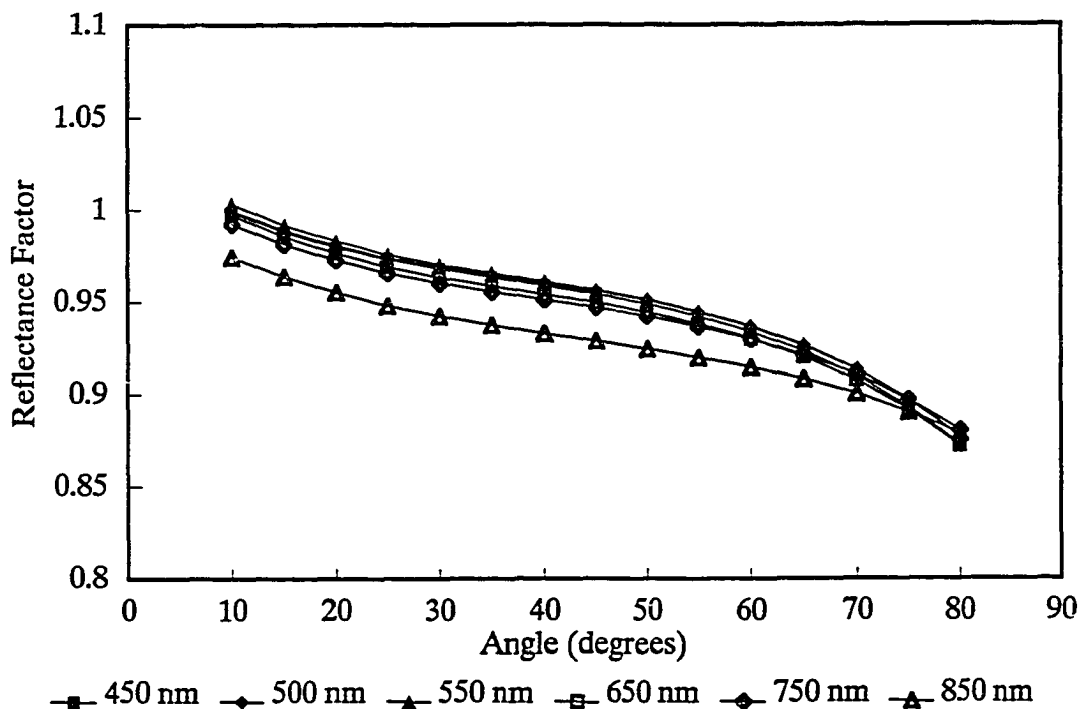


Figure 3.3. Panel OSC #2 reflectance factors.

for meticulous care in the construction of the panels and demonstrates the need for careful calibration if they are to be used as a reference for ground-based measurements.

Comparison between the field and laboratory calibrations

Summary of the field method

The evaluation of $R(0^\circ; \theta)$ in the field required a Halon[®] reflectance standard of sufficient size (approximately that of the field standards) and a goniometer to position the reference panel at a known incidence angle to the sun. The measurements were recorded with an MMR which simulated the seven TM bands. The incidence angles ranged from 15 to 75 degrees in steps of about 10 degrees. As the solar irradiance changed during the course of the measurements, the data-taking sequence was repeated immediately after

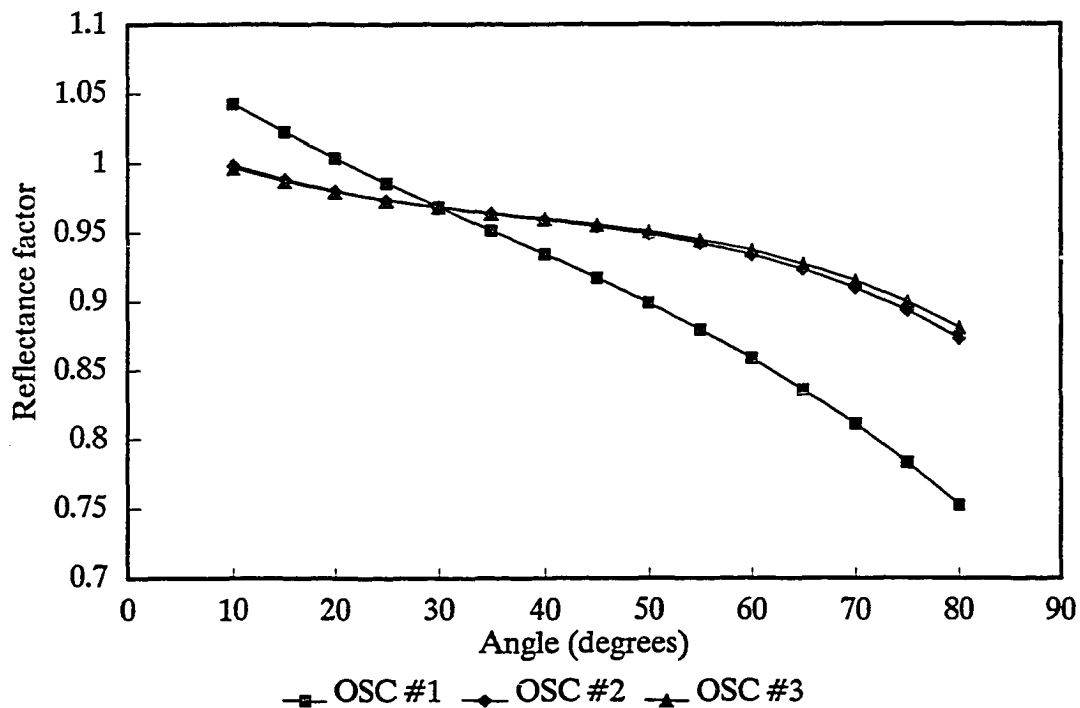


Figure 3.4. Reflectance factors at 450 nm.

completing the 75 degrees measurement but in reverse order. Then, the average of the two readings at each angle were used, minimizing the effect of the earth's rotation.

Because directional quantities were of interest, only the direct solar beam contribution was wanted. Thus, the diffuse sky radiation had to be subtracted from the total. This was done using a flat panel on a 3-m pole as a parasol to alternatively shadow and expose the panel. Two diffuse measurements were made, averaged and subtracted from the sunlit measurement. The corrected data were processed as described above for the laboratory calibration with the exception that the incidence angle data was fit to a third-order polynomial. Also, the first derivative was not forced to zero at zero view due to the low order of the fit and the fewer data points.

Differences between the laboratory and field experiments

There are three major differences between the laboratory calibration and the field calibration; they are the field of view (FOV) of the radiometers, the source, and the radiometer bandpass. In order to compare the results, the data from one experiment must be modified to correct for the differences.

The size of the laboratory, the geometry, and the size of the Halon[®] reference in the laboratory limit the FOV of the radiometers to about one degree in order to minimize any out-of-field contribution. In the field a 15 degree FOV is normally used to average over surface irregularities of the target. To compensate for this difference, the laboratory results were integrated over the field-radiometer field of view. The main effect was to smooth the reflectance factor curve and lower the value at large incidence angles.

The lamp source is quite different from the sun in several respects. The lamp is a finite distance from the panel providing a diverging beam whereas the sun gives a parallel beam. Hence, in the laboratory, the illumination of the panel over the FOV of the radiometer is not constant. We have calculated the effect numerically using a piecewise linear approximation to the FOV. This effect is dependent on both incidence and view angle. The effective temperature of the sun and the lamp are quite different. This results in an effective shift in the center wavelength of the radiometer bandpasses. The magnitude of the shift is dependent on the bandpass of the filter. It is negligible for narrow filters and is about 6 nm for a 100 nm filter such as the SPOT HRV XS1 filter. The "moment" method described by Palmer and Tomasko (1980) was used to calculate the effective center wavelengths independent of source. Figure 3.5 shows the normalized irradiance of the sun and a lamp and the normalized filter response for XS1.

The final consideration is the radiometers' central wavelengths. The laboratory radiometer does not match the field instruments. We fit the data for a given incidence angle

with a 3rd order polynomial in wavelength and interpolated to the required field radiometer wavelengths.

Comparison

Comparing the reflectance factor data with only a correction for wavelength, the largest difference was 0.02 in reflectance. With corrections for the FOV and the finite source distance, the largest difference was 0.013 in reflectance. Figure 3.6 shows the reflectance factors from the two methods.

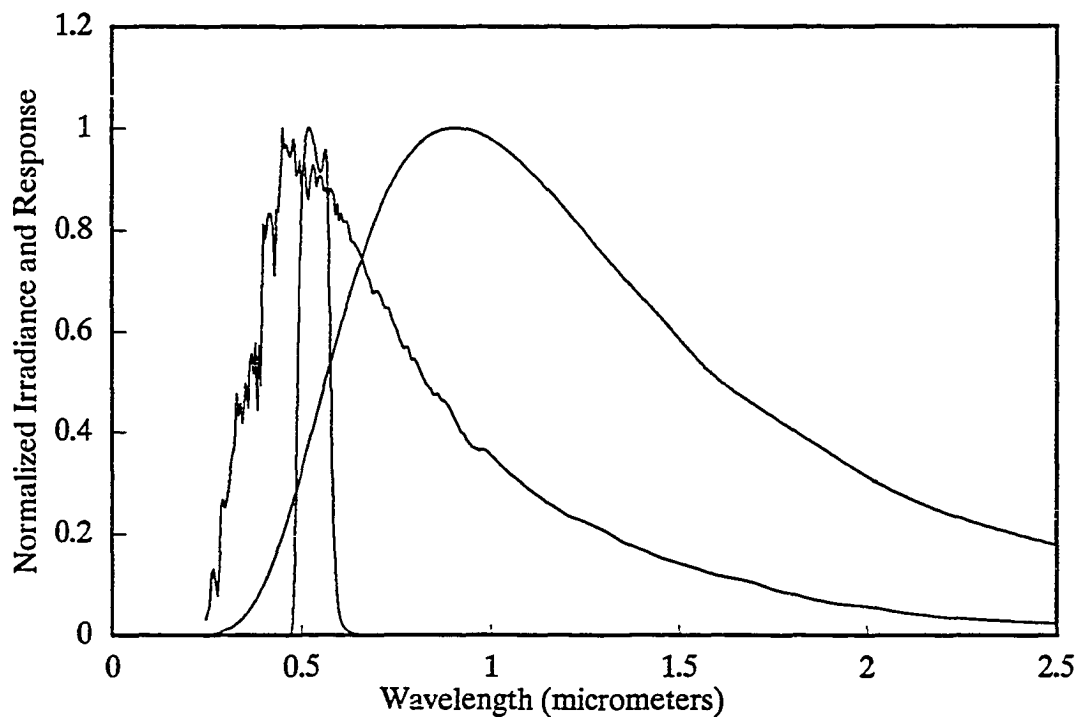


Figure 3.5. Normalized irradiance and filter response.

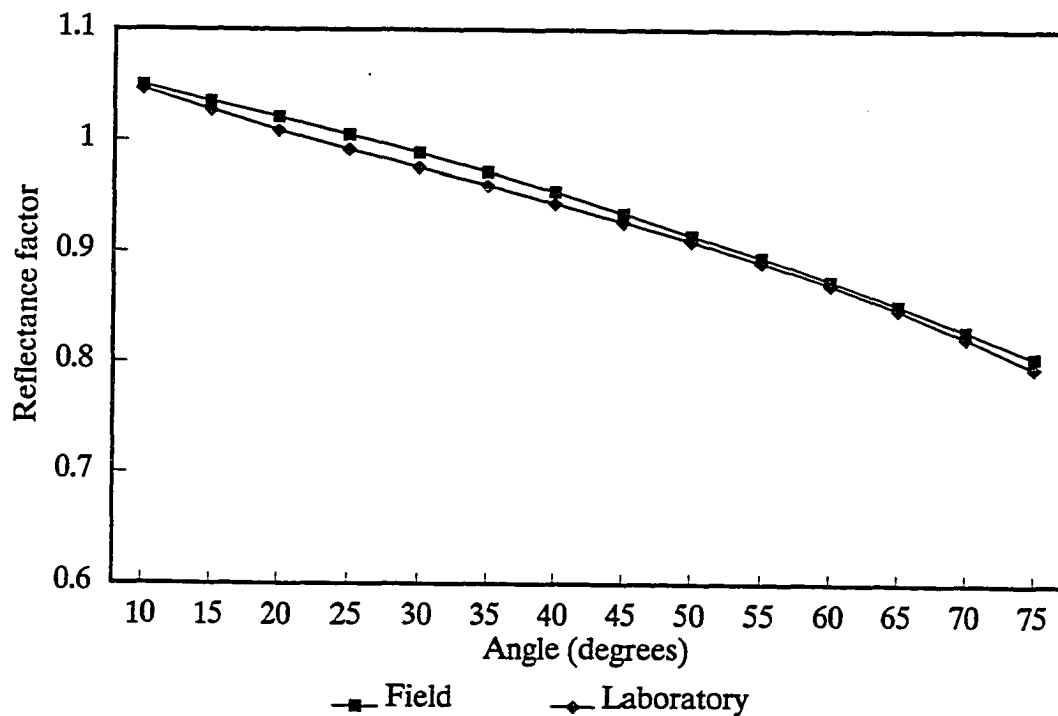


Figure 3.6. Reflectance factor comparison.

Conclusions

A method and equipment have been described for the calibration of several field reflectance panels in terms of their directional reflectance factors. The results confirm the need for accurate calibration of any standard before field use.

The results of the measurements are very repeatable. They agree within 0.013 in reflectance with the results of an independent field method when corrections are made for geometry, wavelength and field of view differences. The automated equipment makes possible quick measurements, which facilitate the calibration of panels before and after important field experiments.

Since the original panel calibrations in August 1987 using this apparatus, the same BaSO_4 panels have been recalibrated prior to use in important field experiments. Spectralon®

panels from Labsphere have also been calibrated using this apparatus. Our results show that Spectralon® is more lambertian than pressed Halon® for angles less than about 60 degrees (wavelength dependent). Since Spectralon® is cleanable and more robust than either pressed Halon® or painted BaSO₄, it is a good candidate for a field reflectance panel.

Optical Depth Determination

We have collected spectral optical depth data on many dates at the White Sands Missile Range near Alamogordo, N.M., the Maricopa Agricultural Center (MAC) near Maricopa, Ariz., and Edwards Air Force Base near Mojave, Calif. On most of these days, the component of spectral optical depth from aerosol scattering between 0.37 and 1.04 μm can be adequately fit to a function of the form of equation 2.39. In order to compute the scattering for use in the radiative transfer code, we must determine ν . I shall use data taken at MAC in June 1988 during an experiment called MAC III to demonstrate the iterative method for deriving optical depths.

Figure 3.7 is an example of a Langley plot for one band during MAC III on 12 June 1988. We measured spectral extinction optical depths at our radiometer's wavelengths for three days during the MAC III experiment (Table 3.2). The radiometer wavelengths were chosen to avoid absorption bands and lines due to atmospheric constituents other than ozone, nitrogen dioxide, and the 0.94- μm band of water vapor.

Measurements at MAC III

We made measurements of the spectral optical depth, barometric pressure, ambient air temperature, integrated solar irradiance, and relative humidity during the mornings of 11-13 June, 1988, at the Maricopa Agricultural Center. Measurements were made from solar zenith angles of about 81 degrees (airmass of about 6.5) until solar noon. The airmass at solar noon was about 1.015, which corresponds to a solar zenith angle of about 9.9 degrees. Two solar radiometers were used for the spectral optical depth measurements. The first was

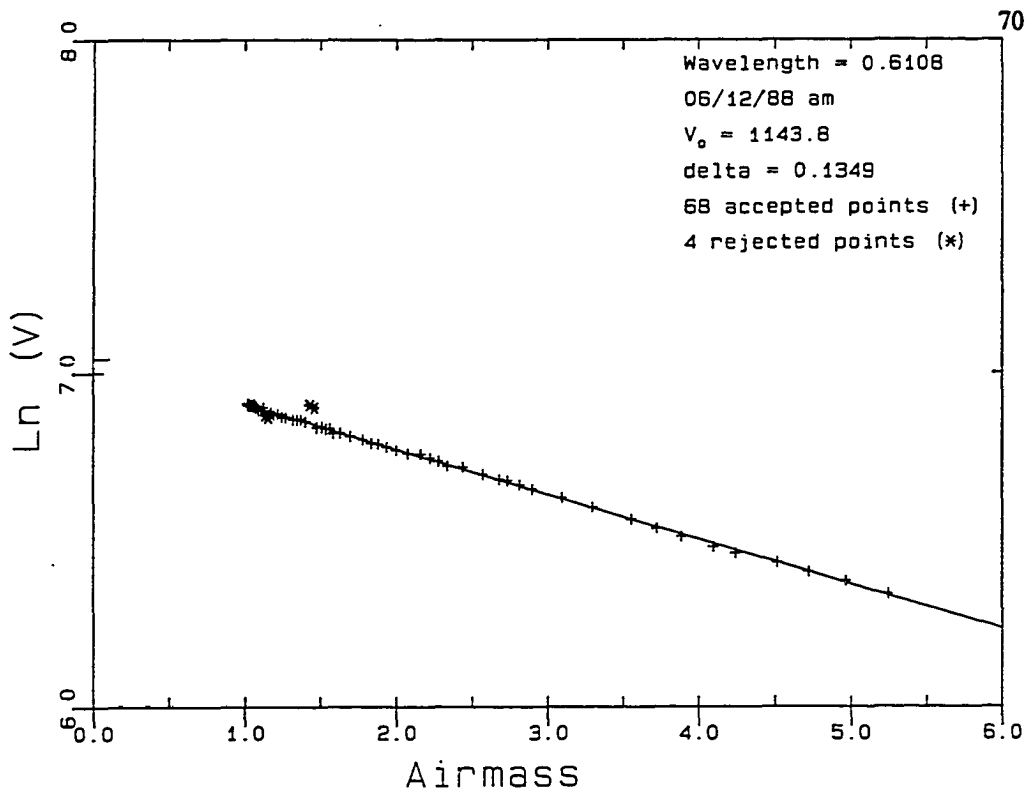


Figure 3.7 Langley plot for 0.6108 μm on 88.06.12 at MAC.

a manually aimed and operated portable solar radiometer with nine narrowband (about 10 nm) interference filters between about 400 and 1040 nm designed by J. A. Reagan. It uses a single temperature-stabilized silicon photodetector. It has been calibrated at a high altitude site in Arizona and in Tucson. The resultant intercept values are not the same, hence the calibration is not well known or the radiometer drifts. We used a full Langley plot analysis of the slope whenever possible at MAC III. The second radiometer was an automated spectropolarimeter with 12 filters (Castle, 1985). The first nine filters cover the range of 420 to 1040 nm and the last three are in the short-wavelength infrared between 1600 and 2400 nm. Temperature-stabilized silicon and lead sulfide detectors are used in the second instrument, which is controlled by a small portable computer. The solar tracking is based on

Table 3.2. Extinction optical depths (δ) at MAC III.			
Wavelength (nm)	Date		
	June 11	June 12	June 13
403.1	0.409	0.386	0.420
444.7	0.294	0.273	0.301
521.1	0.192	0.168	0.192
610.8	0.151	0.135	0.152
670.5	0.106	0.090	0.100
711.7	0.090	0.077	0.088
779.5	0.060	0.054	0.068
873.0	0.060	0.046	0.051
1035.0	0.039	0.041	0.044

the low precision series algorithms and coefficients from the *Almanac for Computers* (United States Naval Observatory, 1988). Solar data were collected at 3-minute intervals with the automated instrument. Data were collected at the operator's discretion with the manual instrument.

The local weather conditions were good for most of the time although some high cirrus clouds and localized dust affected the radiometer data. The automated radiometer failed on 13 June so only data from the portable instrument are presented. Table 3.2 gives the extinction optical depths as measured by the manual solar radiometer. The average barometric pressure for the three mornings was 969.9, 966.2 and 969.2 mb respectively.

Spectral Optical Depths at MAC III

The iterative partition method described above was applied to three data sets. The ozone absorption coefficients used were from Vigroux (1953). The results are given in Table 3.3. The components in the table may not add to give the measured extinction as the

aerosol and ozone optical depths are derived from a linear fit. The extinction optical depth is higher than expected on all three days at 1035.2 nm. This might be due to either absorption by ice crystals in the barely visible high cirrus clouds or a size distribution not described adequately by a Jungian distribution for longer wavelengths. Other workers who have noted this effect in Arizona (Reagan, 1989) suspect ice crystals. This datum point adversely affects the straight line fit of $\log(\delta)$ versus $\log(\lambda)$. Therefore, the 1035.2 nm data were not used in determining the Junge parameter ν and the ozone amount.

The computed Junge parameter and ozone amounts are reasonable for the visibility conditions, time of year, and latitude. The normally accepted value for ozone in June at the latitude for MAC is 0.31 (Iqbal, 1983). Other solar radiometer measurements of ozone have shown large (greater than 20 percent) day-to-day fluctuations (Herman, 1989). The Nimbus 7 Total Ozone Mapping Spectrometer (TOMS) gave ozone amounts of 0.273, 0.268, and 0.272 for the three MAC III dates. The Junge parameter normally falls in the range of $2 < \nu < 4$ (Liou, 1980). On 12 and 13 June 1988, the iterative method gave a Junge parameter slightly smaller than the first estimate given by the two-point fit (0.05 and 0.09). This is due to the non-zero ozone absorption at 444.7 nm and the probable errors in extinction optical depth measurements at 444.7 and 873.0 nm. On 11 June 1988, the iterative method gave a larger ν because of the high optical depth at 0.873 μm (probable measurement error). Graphs of the partition for the three days are presented as Figures 3.8 - 3.10.

Table 3.3. Spectral optical depth components at MAC III.			
Wavelength	Rayleigh	Aerosol	Ozone
11 Jun 88			
403.1	0.333	0.076	0.000
444.7	0.222	0.070	0.001
521.1	0.116	0.062	0.015
601.8	0.061	0.054	0.037
670.5	0.042	0.050	0.014
711.7	0.033	0.048	0.006
779.5	0.023	0.045	0.000
873.0	0.014	0.041	0.000
Junge (ν) = 2.66, Ozone = 0.301 cm atm.			
12 Jun 88			
403.1	0.332	0.053	0.000
444.7	0.221	0.049	0.001
521.1	0.115	0.044	0.014
601.8	0.060	0.039	0.035
670.5	0.041	0.037	0.013
711.7	0.033	0.035	0.006
779.5	0.023	0.033	0.000
873.0	0.014	0.031	0.000
Junge (ν) = 2.70, Ozone = 0.290 cm atm.			
13 Jun 88			
403.1	0.333	0.085	0.000
444.7	0.222	0.077	0.001
521.1	0.116	0.065	0.014
601.8	0.061	0.055	0.036
670.5	0.042	0.050	0.014
711.7	0.033	0.047	0.006
779.5	0.023	0.043	0.000
873.0	0.014	0.038	0.000
Junge (ν) = 3.03, Ozone = 0.296 cm atm.			

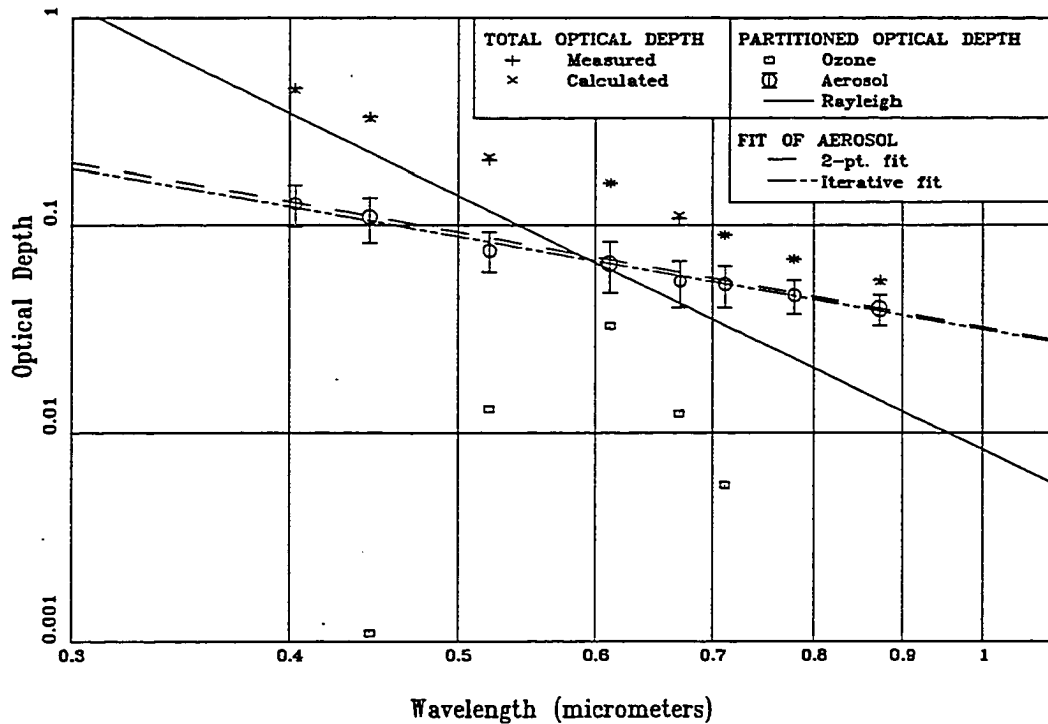


Figure 3.8 Optical depths on 88.06.11 at MAC.

The Reflectance-based method

Reflectance-based methods for in-flight vicarious calibration are believed to have been first proposed by Coulson and Jacobowitz (1972). The first reported attempt to conduct such a calibration was 10 years later by Koepke (1982) who, as far as can be ascertained, has the distinction of coining the term "vicarious calibration". His method, used for the calibration of Meteosat, was based on estimates of ground reflectances and visibilities: the only measurements were of barometric pressure, water vapor and the output of the sensor when it viewed deep space to calibrate the offset values. The estimated 6% uncertainty probably represented a lower limit for the method because it depended on reflectance data not collected simultaneously with the Meteosat imagery and visibility estimates that provided

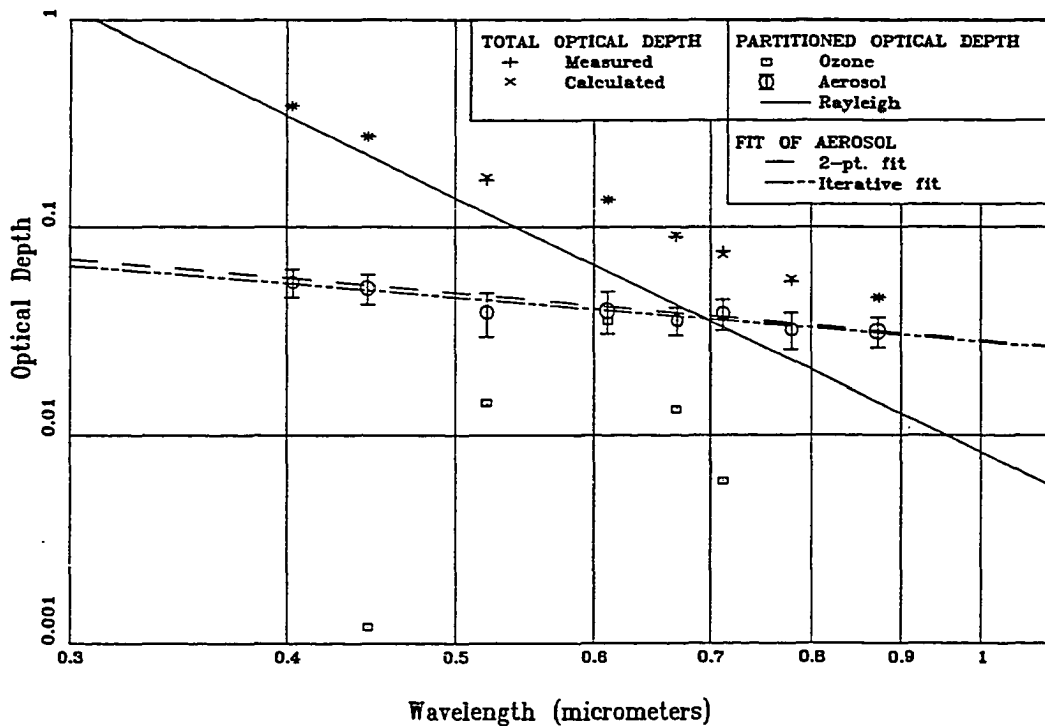


Figure 3.9 Optical depths on 88.06.12 at MAC.

approximate values for optical depths and because Meteosat imagery has only 6-bit resolution. Shortly after Koepke's work, several attempts were made to retrieve reflectances from Landsat-1 Multispectral Scanner System (MSS) data (Hulstrom, 1975; Griggs, 1973; Turner et al., 1975; Potter, 1975, and Fraser et al., 1977). These attempts are mentioned because they are examples of the inverse problem of atmospheric correction and to point out that one reason they were not entirely successful was because of the uncertainty in the in-flight absolute calibration of the MSS. Gordon et al. (1983) described a method for the atmospheric correction of the Coastal Zone Color Scanner (CZCS) that, in conjunction with ocean reflectance measurements, provided a calibration of the sensor. They used an algorithm involving a ratio of the aerosol-optical depths at 520 and 550 nm to that at

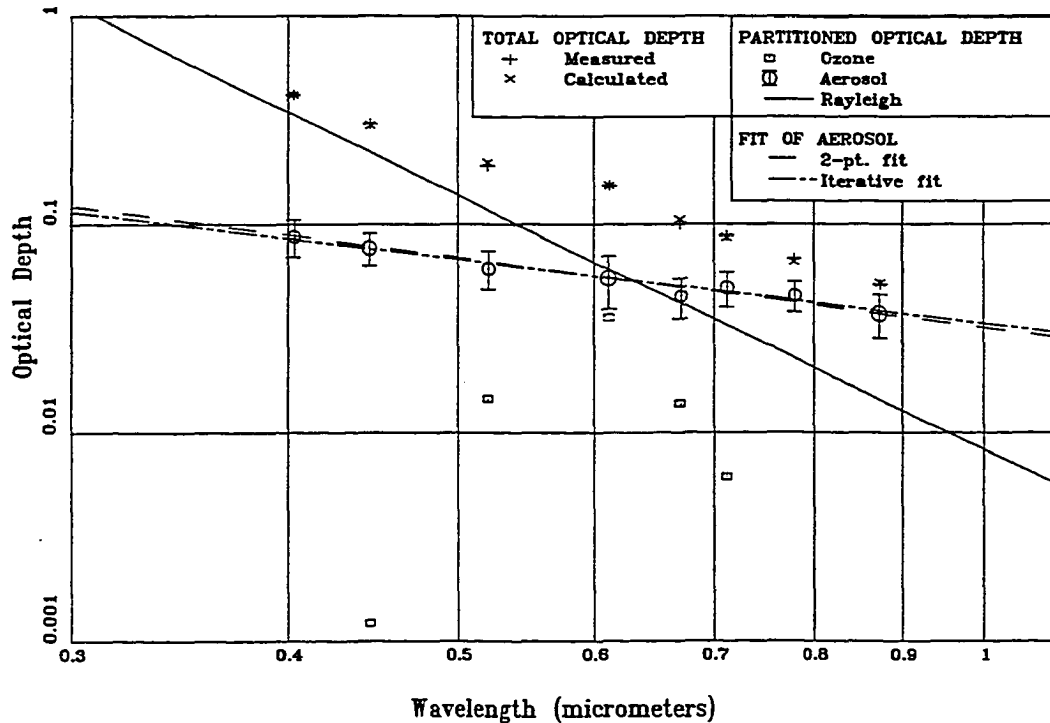


Figure 3.10 Optical depths on 88.06.13 at MAC.

670nm, where the ocean reflectance is assumed zero. This atmospheric-correction algorithm had an average error of 10% - 15%. Gordon (1987) determined, on the basis of a careful error budget, that the calibration uncertainty of his ocean-reference method is at the 1-2 digital count level for CZCS, which corresponds to an absolute calibration uncertainty of less than 1%. Frouin and Gautier (1987) used a procedure similar to Koepke's, in which only visibilities and water-vapor amounts are actually measured. They estimated that the uncertainties in their calibrations were in the range 8 - 13% depending on the channel considered. The sensors they calibrated were the Visible Infrared Spin Scan Radiometer/Vertical Atmospheric Sounder (VISSR/VAS) and the Advanced Very High Resolution Radiometer (AVHRR), using the dunes area at White Sands, NM, as the

reference area. Slater et al. (1986, 1987) also used White Sands as a reference but chose to work in the alkali-flat region because the variations in surface radiance of the dunes could not be tolerated for the calibration of small instantaneous field-of-view systems like the Thematic Mapper (TM) and SPOT. They measured vertical and bidirectional ground-reflectance factors in the sensor's spectral bands, spectral optical depths, pressure, temperature and relative humidity at the time the satellite sensor imaged the measured area. The results of 12 measurements in the visible had a 1σ RMS variation from the mean of $\pm 1.9\%$ over a 16-month period. For 11 measurements in the solar-reflective IR bands the variation was $\pm 3.4\%$, and the RMS variation for all 23 measurements was $\pm 2.8\%$.

At White Sands Missile Range, we have made reflectance-based calibrations of both TM and HRV. This method is based on the accurate measurement of the ground reflectance of a site during the satellite overpass. For TM, about 1500 measurements are made over a ground area covering 4 by 16 30-m pixels using a backpack-mounted Barnes MMR and/or an Exotech. The radiometer FOV is normally 15 degrees to average out small surface irregularities. Solar radiometer data are taken all morning, along with barometric pressure, temperature, relative humidity, and integrated downward irradiance. From these data, spectral optical depth components are determined along with an estimate of the slope of the Junge size distribution. The optical depths, Junge parameter, and ground reflectance are used as inputs to the radiative transfer calculation using the scalar version of the Herman-Browning code. We make assumptions that the complex refractive index of the aerosols is $1.44-0.005i$ and that the limits of the size distribution are 0.01 and 10.0 μm . The code computes the radiance at the top of the atmosphere for a unit solar irradiance. The computation is made at the center wavelength of the sensor band as determined by the moments method. A solar spectral irradiance from Iqbal corrected for the solar distance is used to compute the spectral radiance at the sensor. This radiance is corrected by a

multiplicative gaseous transmission term computed by 5S for the band of interest. This corrected radiance is compared with the average digital count from the sensor for the ground site. This comparison gives a calibration in whatever units desired (counts per unit radiance for example).

CHAPTER 4

THE RADIANCE-BASED METHOD

The radiance-based method of sensor calibration uses a well-calibrated radiometer to measure the radiance of a target at approximately the same time and in approximately the same viewing geometry as the sensor to be calibrated. This measured radiance is then corrected for the effects of the atmosphere between the radiometer and the sensor. The correction is small if the radiometer is at a sufficiently high altitude. In this chapter I shall discuss the calibration and use of radiometers which were used in experiments yielding a radiance calibration of the TM in Landsat 5 and the HRV in SPOT. I shall concentrate on the later SPOT calibrations as the techniques used have improved since the TM calibration in October 1984.

Radiance-based calibration measurements were first attempted in 1981 by Kriebel, who used a calibrated radiometer with a 6-degree field-of-view and a silicon detector with a flat spectral response over a 0.4 to 1.1 μm range. He tried to calibrate the visible channel of Meteosat using this instrument in an aircraft at an 11-km altitude, averaging the approximately 1-km diameter ground-sampled area of the radiometer over agricultural, cloud and ocean regions about 20-km in diameter. Although the uncertainty in the calibration of the radiometer was estimated to be less than $\pm 5\%$, the reflectance of the cloudless ocean regions could only be measured to an uncertainty of about $\pm 20\%$ because of their low reflectance and the 6-bit resolution of Meteosat. The land area measurements on successive days were repeatable to $< 0.1\%$. Although the land results agreed to within about 5%, they disagreed substantially ($\times 0.6$) with the ocean results. This was explained by the triangular spectral response of Meteosat, which gives rise to a significantly different output number of digital counts for the same input radiance depending on the aerosol loading, and therefore the spectral distribution of the atmospheric path radiance. Hovis et al. (1985) and

Abel et al. (1988) used a Learjet at 11.8 km and a U-2 at 19.8 km MSL for radiance-based calibrations of VISSR, AVHRR and TM. In their work they used a continuously wavelength-scanning radiometer that covered a 0.4 to 1.05 μm range with a resolution of 7 nm. They sampled the dunes area at White Sands, NM over 1-km and 2.5-km wide areas for the Learjet and U-2, respectively, and 1.6-km long for both aircraft. The 1.6-km distance was in the in-track direction of the polar orbital systems. Abel et al. estimated that the overall uncertainty of their measurements was $\pm 5\%$. They applied a small correction to their data for the path between the aircraft altitude and the top of the atmosphere. Compared to the preflight calibration, they determined that the GOES-6 VISSR showed a degradation of 15.8% and 13.2% over the two linear ranges (out of a total of five) of its response corresponding to the measured White Sands radiances. This calibration was made after the sensor had been in orbit for 3.5 years. For the AVHRR on NOAA-9 they found that after six months in orbit, channel 1 was unchanged and channel 2 had degraded by 6%. After 20 months, channel 1 had degraded by 13.3% and channel 2 by 18.9%. These changes in sensitivity are with respect to preflight calibration. For the TM on Landsat 5, after 17 months in orbit, band 1 had degraded by 4.7%, bands 2 and 3 were unchanged and band 4 was 12% higher in response.

Slater et al. (1987) also attempted a radiance-based calibration of TM using a calibrated radiometer in a helicopter, the agreement in counts per unit radiance with the reflectance-based calibration for the same day was found to be within 5% for the first three TM bands. The difference of about 10% in band 4 was evidence that the method used for accounting for the water-vapor absorption in the reflectance-based method gave rise to an overcorrection. This is an example of the value of using two, and more when possible, independent calibration procedures to detect systematic errors.

The radiometers used in the radiance method must be calibrated both spectrally and radiometrically. First the bandpass of the individual channels of the radiometer must be accurately determined. Then the radiometer must be calibrated radiometrically by measuring a known radiance distribution. The radiometers used in these experiments were a spectropolarimeter designed and built at the Optical Sciences Center by Castle (1985) and a commercially available four channel radiometer model 100AX built by Exotech. Both instruments are filter radiometers that use silicon detectors. The Castle instrument detector is thermally stabilized at a temperature of about 45° C to reduce responsivity changes with temperature at wavelengths longer than about 850 nm. Both instruments are DC coupled and do not use choppers. They can be powered by batteries and use battery-powered microprocessor controllers and digitizers. Both instruments have selectable fields of view and were used with a nominal 1-degree full field-of-view. The Castle instrument was used for the calibration of TM and the Exotech for SPOT.

Spectral Calibration

In order for a radiometer to be accurately calibrated in radiance units, the spectral bandpass of the radiometer must be known. For the radiometers used in the radiance method, the spectral bandpass is determined mainly by the characteristics of the interference filters (and blocking filters if used). The detector response is a second order effect. The filters were removed from the radiometers and the transmission as a function of wavelength was measured by a Cary 17 spectrophotometer in the Optical Sciences Center Measurements Laboratory. The wavelengths scanned were between 300 and 1100 nm for the Exotech and 300 to 3000 nm for the Castle instrument. The filters were scanned over these limits to determine if there were any out-of-band "leaks" that might affect the radiometer bandpass. No problems were found in the filters for the Exotech or Castle instruments. The MMR filters were also scanned. The band 5 MMR filter (1.15 to 1.3 μm) was found to have a

"leak" that might cause a 10 to 20 % error. This band does not correspond to a TM band. This band is not normally used for our calibration work so the leak is not of importance. If, however, this band is used, the leak must be considered. The filters were scanned at 1-nm intervals. The moments method was used to determine the central wavelength and effective bandpass limits for each filter for each radiometer. The wavelengths were then recomputed after the filter response was modified by the response of a nominal silicon detector of the type used in the radiometers. The results can vary depending on the filter bandpass and the central wavelength. For the nominal 10-nm filters used in the Castle, the shift is negligible. For wider filters such as the SPOT HRV XS1 filter used with the Exotech, the shift of about 6 nm must be considered.

The spectral characteristics of Halon[®] have been determined by NIST and were used to determine the spectral characteristics of the BaSO₄ panels used in the laboratory calibration. A FEL type lamp was used as a secondary standard of spectral irradiance. These lamps were calibrated in irradiance at a specified distance from the mounting pins and at a specified lamp direct current of a specified polarity. The calibration and uncertainty was given as a function of wavelength. The irradiance at 50 cm of a lamp with an identification number of F196 is plotted as a function of wavelength in Figure 4.1. The curve is a cubic spline interpolation of the tabulated calibration data. This lamp was calibrated from 250 nm to 2500 nm by Optronic Laboratories. With a calibrated source such as a FEL lamp and a calibrated reflectance panel such as the BaSO₄ panels calibrated in the laboratory, a known spectral radiance distribution can be generated.

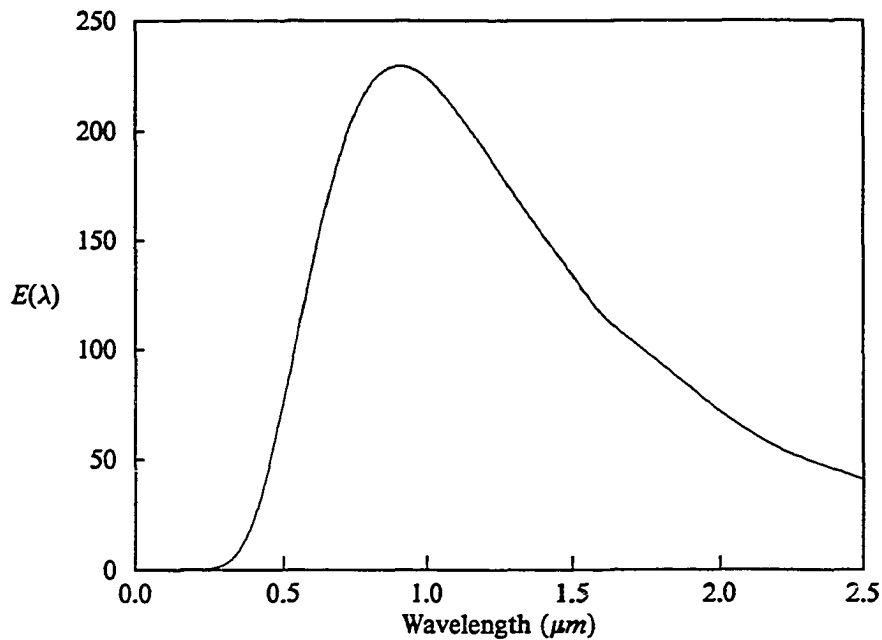


Figure 4.1. Lamp F196 Spectral Irradiance.

Radiometric Calibration

For the radiance method, the radiometer must be calibrated to an absolute radiance scale. The radiometer was mounted on the reflectance measurement radiometer holder. The panel was aligned such that the lamp was on the normal from the panel center 50 cm from the panel. The radiometer was oriented such that it viewed the center of the panel at a 45° angle with respect to the panel normal to prevent any shadowing problems. The radiometer response in a dark room with the source off was measured with an integration time of 100 power line cycles to obtain the dark response voltage. The lamp was then brought slowly to its rated current of 8.0 amperes and allowed to stabilize for at least 30 minutes. A new dark reading was taken with the panel covered and with the aperture of the radiometer blocked

by a black anodized panel painted flat black. The panel was then uncovered and the aperture opened. The lamp current was measured with an integration time of 100 power line cycles and reset if necessary. A series of 100 readings at an integration time of 10 power line cycles were taken for each radiometer band. The lamp current was measured to ensure that it had not changed. If the lamp current had changed by more than 0.001 amp, the set was discarded. The dark readings were repeated at the long integration time after each set of 100 readings. The three dark readings were virtually the same for each band.

The radiance distribution was numerically integrated over the radiometer bandpass and the portion of the panel viewed by the radiometer. The distribution was known on a grid of wavelength and angle points. The angular grid can be fit with good accuracy to a polynomial in angle for either a Halon[®] or BaSO₄ panel. The panel calibration directly gives the polynomial for Halon[®] at the measurement wavelengths. For BaSO₄, the calibration is the Halon[®] polynomial multiplied by the ratio of the voltage readings. This data set can usually be fit to another polynomial of the same order with differences between the fit and the data less than the uncertainty in the hemispheric reflectance of the Halon[®]. The wavelength data can be fit with another polynomial or a cubic spline. The Halon[®] panel reflectance is quite flat with respect to wavelength for the region between 400 and 1050 nm where the radiance method has been used. The BaSO₄ panel is also smooth in this region. We developed continuous functions to describe the spectral dependence of the lamp source and the reflectance. We then numerically integrated the product of the lamp output and panel reflectance over the bandpass and the area subtended by the field of view. In the case of a 1° FOV, the angular dependence was small: the minimum value within the nominal FOV (at the edge) was within 0.2 percent of the maximum value. The range of values over the spatial distribution could be reduced by increasing the lamp-to-panel distance. Any increase in distance would, however, decrease the radiance values and hence

the accuracy of the calibration. The lamp and panel combination is not nearly as bright as the sunlit scene viewed during the radiance method calibration so the lamp was used at the 50 cm calibration distance to obtain maximum brightness for this configuration. Table 4.1 gives the radiometer responses during the calibration of Exotech serial number 3526 with the external SPOT filters. This calibration was done on 1987 December 04.

Table 4.1. Exotech 3526 responses during laboratory calibration on 87.12.04 with FEL lamp F196 and BaSO ₄ panel #3.					
Band	Average Lamp Current	Average Dark Voltage	Average Detector Voltage	± Standard Deviation (1 sigma (%))	Signal Voltage
Pan	8.0001	0.00075	0.7120	± 0.012	0.7113
XS1	8.0004	0.00348	0.2136	± 0.047	0.2100
XS2	8.0004	-0.0087	0.0985	± 0.176	0.1071
XS3	8.0003	0.0016	0.3949	± 0.027	0.3933

The signal in all four bands was lower than desired. However, if we consider the error to be no more than three times the standard deviation, the worst case voltage measurement error was still less than 0.53 percent for all bands. The uncertainty in the NIST 1973 scale of spectral irradiance is not more than 1.2 percent for the wavelengths used in the Exotech calibration (Schneider, 1986). The transfer uncertainty for these wavelengths is no more than 0.5 percent according to Optronic Laboratories. The lamp alignment should allow the uncertainties due to position to be on the order of a few tenths of one percent. The current regulation of the power supplies and the measurement accuracy should reduce the errors due to current variations to less than 0.5 percent. The panel calibration of reflectance factor is

probably better than 2 percent. The uncertainty in the radiance value of the panel is probably about 2.5 percent (root sum of square). The worst case error is probably less than 5 percent.

We have not checked the linearity of the radiometer over the entire output range of 0 to 5 volts due to source limitations. We did check the accuracy of the gain-change switching for the XS2 band using a higher output uncalibrated lamp and found it to be about 0.5 percent. This error is smaller than other major error sources. The voltage in the XS2 band is so low during calibration that there is probably greater error than stated above in using the calibration for a bright scene. One reason for this low signal was that the gain setting used while collecting the data was too low by a factor of at least 5.

Table 4.2 gives the calculated wavelengths, bandwidths and normalized response of the

Band	Center Wavelength	Bandwidth	Short Wavelength	Long Wavelength	Response
Pan	0.6077	0.2201	0.4976	0.7177	0.8876
XS1	0.5480	0.1017	0.4971	0.5989	0.8991
XS2	0.6519	0.0757	0.6141	0.6898	0.6367
XS3	0.8375	0.1164	0.7793	0.8957	0.7818

filters. The individual filter-detector responses are shown in Figures 4.2 through 4.5 along with the calculated bandwidths. Table 4.3 gives the integrated irradiance, panel reflectance at the central wavelength, and the spectral radiance for the laboratory calibration. Figure 4.6 shows the cubic spline interpolated spectral reflectance values for the #3 panel. The

spectral radiance is a numerical integration of the product of the spectral irradiance and spectral reflectance which is then divided by the equivalent bandpass.

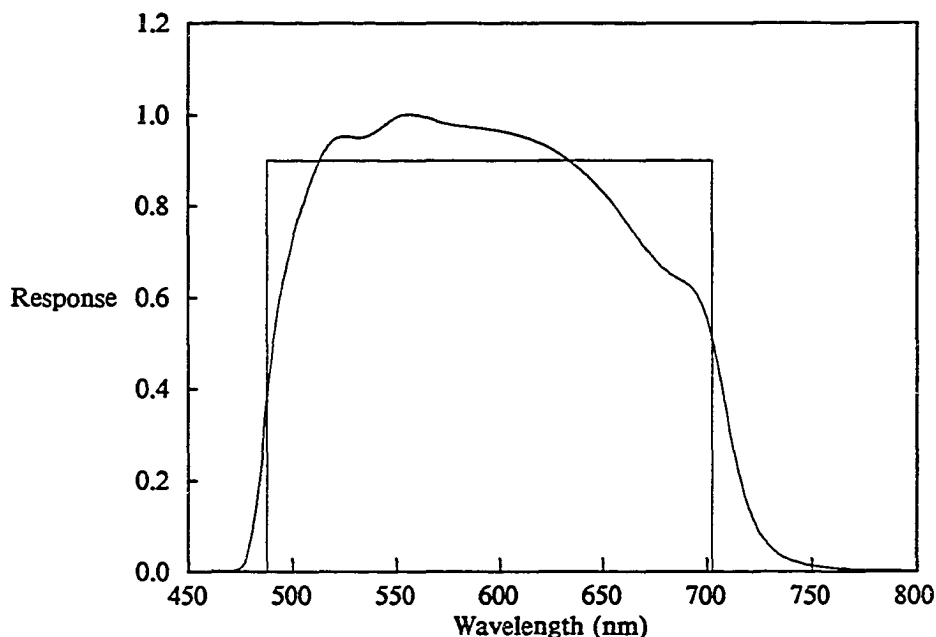


Figure 4.2. SPOT HRV Panchromatic band filter response

The Exotech 3526 was used with the external SPOT filters on 87.07.17 while flying at 10000 feet above mean sea level (MSL). This corresponds to 3048 meters MSL and approximately 6000 feet above ground level (AGL). The ground instantaneous field of view for the radiometer at this altitude is about 32 meters, a good match for TM and the SPOT HRV spectral bands. The radiance-based calibration method was tested at Chuck site (106.351 West 32.919 North) at the White Sands Missile Range. The radiometer and operator were carried aloft in a United States Army UH-1H utility helicopter. The radiometer was hand-held and aimed by the operator using the built-in telescopic sight. The radiometer was configured for a 1-degree full FOV and was pointed vertically down at the site. The

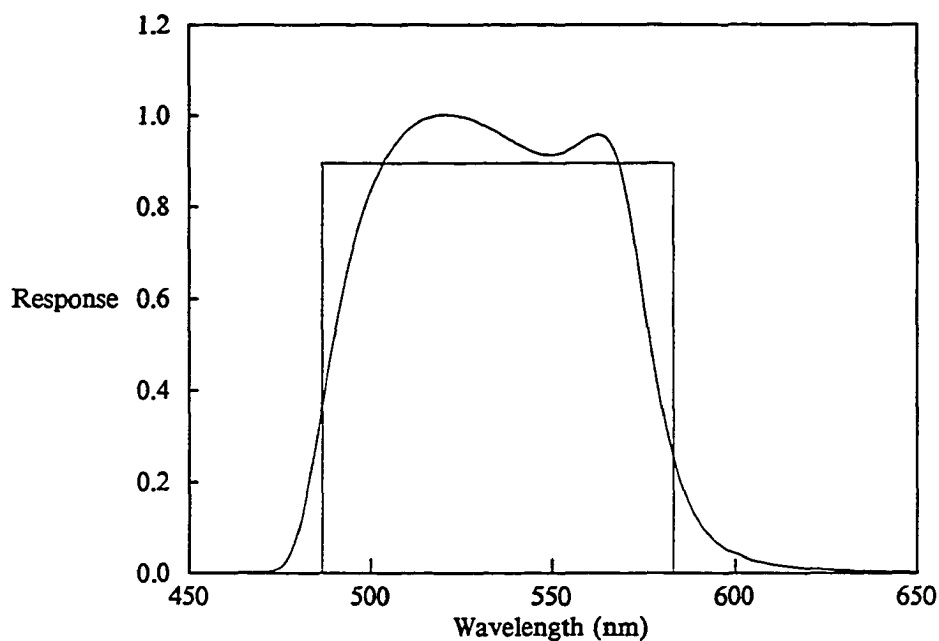


Figure 4.3. SPOT HRV Spectral band 1 (XS1) filter response

view angle was not always exactly vertical due to the movement of the helicopter and possible obstruction by the helicopter landing skid. The radiometer data were sampled at 2 second intervals and then sequentially digitized and logged by an Omnidata Polycorder with a custom sample-and-hold circuit. The voltage readings could not be correlated to actual parts of the site so the readings given in Table 4.4 are averages of the entire SPOT site scanned from East to West. The time given was the mean of 11 and 16 samples respectively. The large standard deviation of the voltage measurements in the field as compared to that in the laboratory was most likely due to nonuniformities in the reflectance of the gypsum of White Sands. This variation was noted by the radiometer operator and in color photography collected during the radiance measurements.

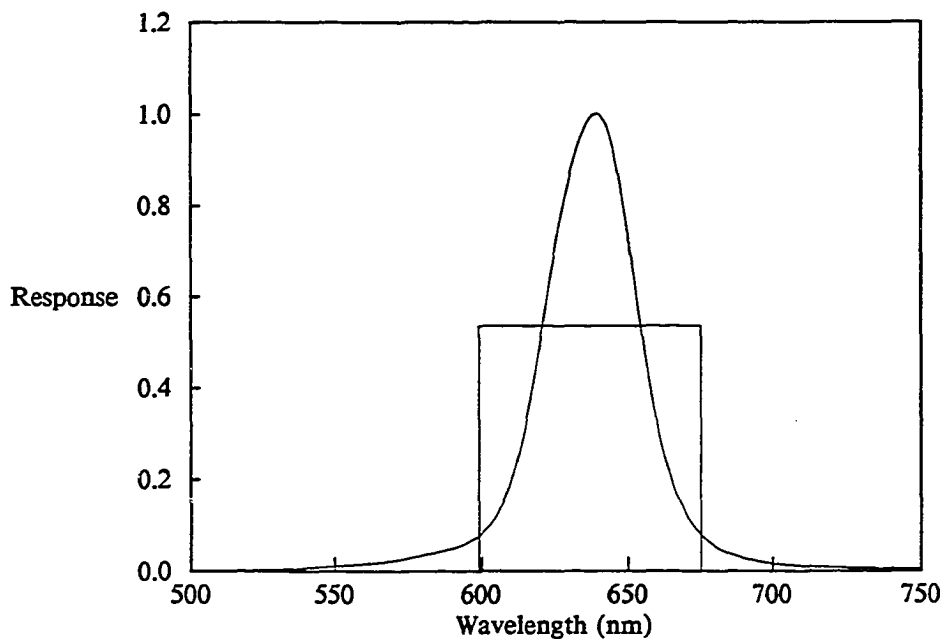


Figure 4.4. SPOT HRV Spectral band (XS2) filter response

The measurements were converted to radiance using the laboratory derived radiometer calibration factors. Table 4.5 gives the spectral radiance measured at 10000 feet MSL. In order to assess the validity of these results, we used the radiative transfer code of Herman and Browning modified to output the normalized radiance at any desired level to compute the radiance at 6000 feet AGL. This output was multiplied by the exoatmospheric spectral irradiance and a gaseous transmission term to calculate the spectral radiance. For the pan band, the code was run at nine wavelengths and the results integrated by the trapezoidal rule and then divided by the bandpass. The predicted radiance for the three spectral bands was that at the central wavelength. The gaseous transmission term was determined by a custom version of the "SS" code which incorporated the measured filter functions and took into account both the sensor altitude and the ground elevation. The measured and calculated

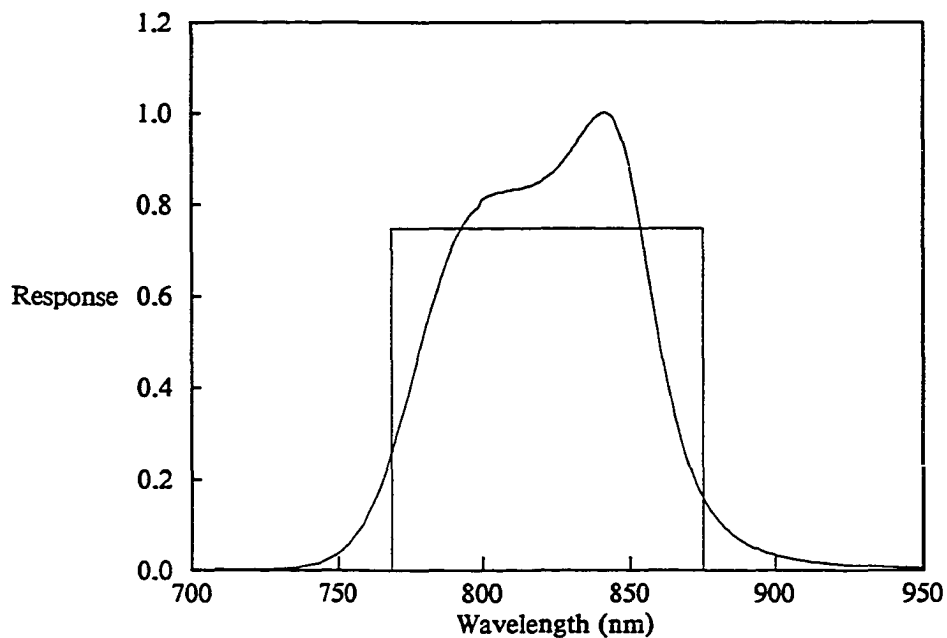


Figure 4.5. SPOT HRV Spectral band (XS3) filter response

Table 4.3. Standard lamp F196 and BaSO ₄ panel #3 parameters for the 87.12.04 calibration.					
Band	λ_c (μm)	$\Delta \lambda$ (μm)	Integrated Irradiance (W/m ²)	Reflectance (ρ)	Spectral Radiance (W/m ² -sr- μm)
Pan	0.6077	0.2201	30.74	0.9579	42.484
XS1	0.5481	0.1017	10.65	0.9618	32.039
XS2	0.6519	0.0757	12.61	0.9537	50.585
XS3	0.8375	0.1164	26.11	0.9349	66.776

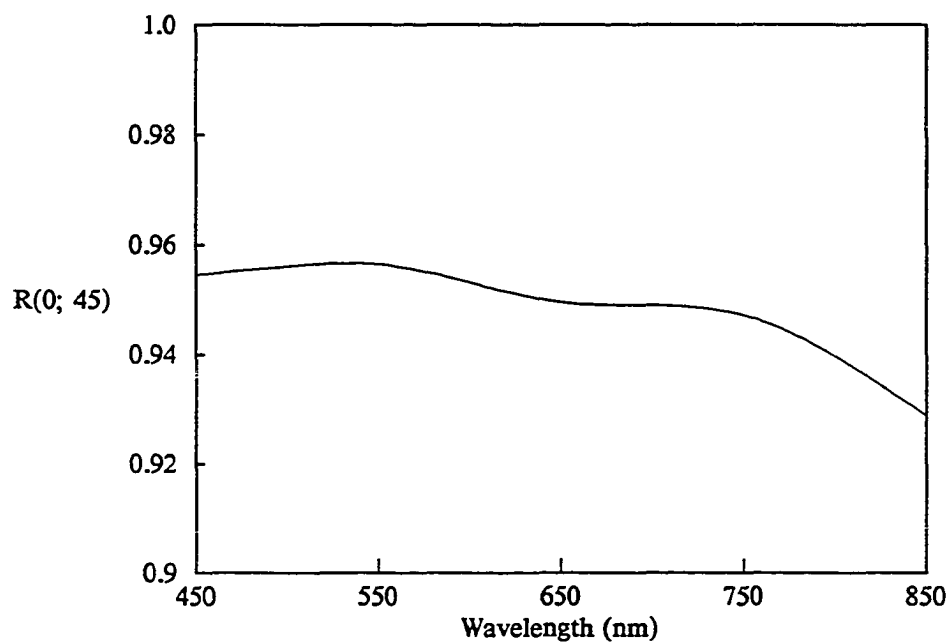


Figure 4.6. BaSO₄ panel #3 spectral reflectance factor at 45 degrees

Table 4.4. Average Exotech outputs for 87.07.17 over Chuck Site at White Sands Missile Range					
Band	Time: 10:31:38		Time: 10:37:06		
	Voltage	σ in %	Voltage	σ in %	
Pan	3.92572	2.045	4.04721	2.290	
XS1	1.67830	1.898	1.74293	1.865	
XS2	0.54344	2.044	0.56235	2.197	
XS3	0.90996	1.740	0.94873	1.887	

Table 4.5. Measured average scene radiances in W/m ² -sr-μm for 87.07.17 over Chuck site at White Sands Missile Range.		
Band	Time: 10:31:38 Spectral Radiance	Time: 10:37:06 Spectral Radiance
Pan	234.5	241.8
XS1	256.0	265.1
XS2	256.6	267.6
XS3	154.5	161.1

spectral radiances for 87.07.17 at White Sands are presented in Table 4.6. The measured values corresponded to a linear extrapolation to the overpass time from the two actual measurement times. The percent difference is $100 * \frac{\text{code radiance} - \text{measured radiance}}{\text{code radiance}}$.

Table 4.6. Interpolated measured and computed scene radiances in W/m ² -sr-μm for 87.07.17 over Chuck site at White Sands Missile Range.			
Band	Time: 10:39:17 Radiance	Calculated Radiance	Percent Difference
Pan	244.7	239.4	- 2.2
XS1	268.7	264.9	- 1.4
XS2	272.0	239.1	-13.8
XS3	163.7	167.1	2.0

Another radiance calibration of SPOT was done on 1988 November 21 over Chuck site at the White Sands Missile Range. The Exotech radiometer was again flown at 10000 feet MSL in a UH-1H helicopter. A higher gain setting was used for the XS2 band. This gain setting was determined in-flight by measuring the site while climbing to final altitude rather than setting it on the ground. For this calibration, the radiometer was fastened to a mount a rifle stock which also held a small CCD color television camera and a Spectron SE-590 linear array spectrometer. The three instruments were mounted about 8 inches apart and boresighted. The output of the video camera was recorded by a video cassette recorder along with a superimposed time signal accurate to one second. The polycorder which digitized the Exotech signal also recorded the time to an accuracy of about one second. The Spectron also records the time that it takes a spectra to one second. The Spectron data were not used for this calibration. The video imagery was used to select appropriate data sets for the radiance calibration. Four sequences of measurements were judged to be accurately aimed at the calibration area in a near vertical orientation. The Exotech output during each sequence was averaged and the standard deviation was found. The average voltage outputs are presented in Table 4.7. These sets correspond to 10, 8, 42, and 166 data points per set. The voltage for the XS3 band was zero because of a break in the cable connecting the Exotech and the sample-and-hold circuit. This problem was discovered when the data were reviewed after the helicopter landed. Hence Table 4.7 and those that follow do not include the XS3 filter values.

The Exotech was calibrated using lamp F196 and a BaSO_4 panel in the laboratory on 1988 December 08. The technique used was the same as the previous SPOT radiance calibration. The resulting calibration was applied to the measured Chuck site voltages to determine the radiance above the site. The radiances for each sequence of measurements and the average are presented in Table 4.8. The radiative transfer code was again run for

the helicopter altitude and the "SS" code was run to compute gaseous transmission. The comparisons between the code computations and the measurements was again quite good and are presented in Table 4.9.

Table 4.7. Average Exotech outputs for 88.11.21 over Chuck Site at White Sands Missile Range. Output is in volts \pm standard deviation in percent.			
Band Time	Pan	XS1	XS2
10.9692	1.6132 \pm 0.91	0.7826 \pm 1.19	2.8326 \pm 0.88
10.9742	1.6458 \pm 0.79	0.8010 \pm 0.72	2.8872 \pm 0.81
10.9855	1.6399 \pm 0.78	0.7981 \pm 0.99	2.8776 \pm 0.68
11.0251	1.6453 \pm 1.01	0.8013 \pm 1.16	2.8976 \pm 0.89

Table 4.8. Measured average scene radiances in W/m ² -sr- μ m for 88.11.21 over Chuck site at White Sands Missile Range.			
Band Time	Pan	XS1	XS2
10.9692	160.63	163.60	157.50
10.9742	163.88	167.43	160.53
10.9855	163.29	166.83	159.99
11.0251	163.83	167.50	159.78
Average	162.91	166.34	159.78

Table 4.9. Measured and computed scene radiances in $W/m^2-sr-\mu m$ for 88.11.21 over Chuck site at White Sands Missile Range.			
Band	Measured Radiance	Calculated Radiance	Percent Difference
Pan	162.9	158.8	-2.6
XS1	166.3	165.0	-0.8
XS2	159.8	162.8	1.8

The 1988.11.21 data was also used to determine the magnitude of the correction required to extrapolate the radiance measurements from 10000 feet MSL to space. In all bands, the radiance at the helicopter altitude was higher than that at the spacecraft. The difference was, however, quite small and calculated as a percent presented in Table 4.10. This result showed that the radiance method requires only a small correction to predict the radiance at an in-orbit sensor.

The radiance-based method was used to check the original reflectance-based calibrations of SPOT after launch in March 1986. The flight procedure at White Sands was the same as described for the later two calibrations. The laboratory calibration was done with a different lamp (F38 at 7.8 amps) and with a much less sophisticated and less accurate reflectance panel apparatus and calibration. The results were, however, within the expected uncertainties of the two methods. With a better laboratory calibration and the improved gaseous absorption calculation now used, the results presented in Table 4.11 would probably have been closer.

Table 4.10. Computed scene radiances at 10000 feet MSL and the top of atmosphere in $W/m^2\text{-sr-}\mu\text{m}$ for 88.11.21 over Chuck site at White Sands Missile Range.			
Band	10000 feet Radiance	Top Radiance	Percent Difference
Pan	158.8	156.1	1.7
XS1	165.0	162.0	1.8
XS2	162.8	161.1	1.0

Table 4.11. Measured and computed scene radiances in $W/m^2\text{-sr-}\mu\text{m}$ for 86.03.08 over Chuck site at White Sands Missile Range.				
Band	Measured Radiance	Measured σ (percent)	Calculated Radiance	Percent Difference
Pan	224.7	2.6	234.0	+4.0
XS1	248.9	2.7	254.1	+2.0
XS2	239.2	2.3	238.8	-0.2
XS3	174.8	2.2	164.0	-6.6

Conclusions

The results presented here demonstrate that the radiance method is a viable means for determining the calibration for the visible and near-IR bands of an in-flight sensor such as the HRV on SPOT and bands 1-4 of the Landsat TM. The radiometer used must be

accurately calibrated and should be flown as high as possible. The correction needed to extrapolate the measured radiance to the spacecraft level is on the order of a few percent for the altitude used and prevailing ground and atmospheric conditions at the White Sands Missile Range, New Mexico during the course of our measurements.

CHAPTER 5

THE IRRADIANCE-BASED METHOD

Introduction

The uncertainty in the absolute radiometric calibration of an optical system can be estimated most reliably by comparing the results of several precise independent methods. This applies equally well to laboratory methods using standard sources or detectors (Schaefer et al., 1984), as it does to on-board and vicarious (ground-reference) methods used for the in-flight calibration of aircraft and space sensors (Slater et al., 1987). Also, disagreement between the results from independent methods can stimulate the search for, and it is hoped the reduction of, sources of systematic errors in the various methods.

For these reasons, we have been exploring two well-known and fundamentally different vicarious methods for satellite-sensor absolute radiometric calibration and have recently developed a third, which is the main topic of this chapter. Of the two well-known methods, one is based on ground-reflectance measurements traceable to a standard of diffuse reflectance and the sun, whose values are traceable to a lamp standard of spectral radiance, while the other is based on ground-radiance measurements from an aircraft, using a radiometer calibrated by a lamp whose irradiance is traceable to a standard of spectral radiance. Both methods are capable of high precision ($<\pm 5\%$) and have the potential to provide low uncertainty ($<\pm 5\%$) absolute calibrations of multispectral sensors in flight.

In this chapter I shall discuss the theory and first results of a new irradiance-based method.

Theory of the Irradiance-Based Method

I shall show in this section that the calibration of aircraft and satellite sensors can be accomplished using measurements of atmospheric optical depth and gaseous transmittance, together with measurements of ground reflectance and the ratio of diffuse-to-global

downward irradiance at ground level. In addition, radiative transfer code results are needed to determine the spherical albedo and intrinsic path radiance of the atmosphere. All the measurements, except those of the diffuse-to-global ratio, are made routinely as part of the reflectance-based method, with the result that the irradiance-based method can be accomplished with the same equipment and personnel usually taken to the field. The following briefly describes the theory behind the irradiance-based method.

Expression for the apparent reflectance

The radiative transfer in the ground-atmosphere system is modeled in the following way. The radiance $L_\lambda(\theta_v, \theta_s, \phi_v - \phi_s)$ measured from space, at wavelength λ , can be expressed as an apparent reflectance:

$$\rho_\lambda^*(\theta_v, \theta_s, \phi_v - \phi_s) = \frac{\pi L_\lambda(\theta_v, \theta_s, \phi_v - \phi_s)}{E_{o\lambda} \mu_s}, \quad (5.1)$$

where $E_{o\lambda}$ is the exo-atmospheric solar spectral irradiance, θ_v , ϕ_v , θ_s , and ϕ_s represent the observation and solar incidence and azimuth angles and $\mu_s = \cos \theta_s$. The notation in the following will be simplified by omitting the subscript λ from spectrally dependent terms.

For a uniform lambertian ground surface of reflectance ρ , the apparent reflectance can be expressed as (Tanré 1982)

$$\rho^*(\theta_v, \theta_s, \phi_v - \phi_s) = \rho_A(\theta_v, \theta_s, \phi_v - \phi_s) + \frac{\tau(\mu_s) \rho \tau(\mu_v)}{1 - \rho s}, \quad (5.2)$$

where τ is the global atmospheric transmittance, ρ_A the intrinsic reflectance of the atmosphere, and s is the spherical albedo of the atmosphere. The spherical albedo is the integrated downward radiance at ground level due to an isotropic upward radiance:

$$s = \frac{1}{\pi} \int_0^{2\pi} \int_0^1 L^-(\delta, \mu) \mu \, d\mu \, d\phi$$

when

$$L^+(\delta, \mu) = 1.$$

Equation 5.2 does not account for gaseous absorption, which reduces the apparent reflectance both in the visible (Chappuis ozone absorption band for example) and in the short-wave infrared (SWIR) atmospheric windows. According to Tanré et al. (1986), Equation 5.2 has to be modified by multiplying the apparent reflectance by the gaseous transmission $T_g(\mu_s, \mu_v)$. This term is decoupled from the scattering process and determined separately using absorber measurements. I shall drop this multiplicative term in the following theoretical development since the irradiance-based method considers only scattering effects. The gaseous transmission term was used in field tests where actual measurements were made.

The global transmittance is given by:

$$\tau(\mu_s) = e^{-\delta/\mu_s} + \frac{\int_0^{2\pi} \int_0^1 L^o(\mu, \mu_s, \phi - \phi_s) \mu d\mu d\phi}{\mu_s E_s} = e^{-\delta/\mu_s} + \frac{E_d^o}{\mu_s E_s}, \quad (5.3)$$

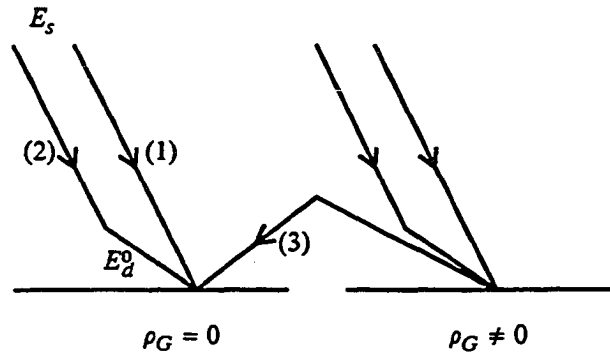
where L^o and E_d^o are respectively the downward radiance and irradiance at the ground level due only to the scattering process; i.e. corresponding to the case of zero ground reflectance. Figure 5.1 is a diagram of the irradiance field as described here.

Let us define the diffuse-to-global irradiance ratio as:

$$\alpha_s = \frac{E_d(\mu_s)}{E_s \mu_s e^{-\delta/\mu_s} + E_d(\mu_s)}. \quad (5.4)$$

We note that the diffuse irradiance term $E_d(\mu_s)$ in Equation 5.4 includes the intrinsic diffuse irradiance $E_d^o(\mu_s)$ and also the coupling term between atmosphere and ground for both the direct beam and the diffuse component for our measurement method. Following Tanré et al. (1982), we find:

$$E_d(\mu_s) = \frac{1}{1 - \rho_S} [E_d^o(\mu_s) + \mu_s E_s e^{-\delta/\mu_s} \rho_S] \quad (5.5)$$



- (1) Direct irradiance at ground level = $\mu_s E_s e^{-\delta/\mu_s}$
 (2) Intrinsic atmospheric irradiance = E_d^0
 (3) Coupled ground-atmosphere irradiance = $\mu_s E_s \frac{\tau(\mu_s)}{1-\rho_s}$

Figure 5.1. Irradiance decomposition.

and, using Equations 5.4 and 5.5, rewrite $\tau(\mu_s)$ as

$$\tau(\mu_s) = \frac{(1-\rho_s) e^{-\delta/\mu_s}}{1-\alpha_s}$$

According to the reciprocity theorem, $\tau(\mu_s)$ and $\tau(\mu_v)$ have the same meaning and therefore $\tau(\mu_v)$ can be expressed in an identical form:

$$\tau(\mu_v) = \frac{(1-\rho_s) e^{-\delta/\mu_v}}{1-\alpha_v}$$

where α_v is the ratio of the diffuse to the total irradiance in the viewing direction.

Equation 5.2 can then be written as:

$$\rho^*(\theta_v, \theta_s, \phi_v - \phi_s) = \rho_A(\theta_v, \theta_s, \phi_v - \phi_s) + \frac{e^{-\delta/\mu_s}}{1-\alpha_s} \rho(1-\rho_s) \frac{e^{-\delta/\mu_v}}{1-\alpha_v}. \quad (5.6)$$

The computation of the apparent reflectance using Equation 5.2 requires the use of a radiative transfer code. The most important input is the optical thickness derived from extinction measurements. The aerosol model, needed to compute the scattering phase matrix, is chosen by assuming values for the aerosol refractive index and the size

distribution. The inaccuracies of the computed apparent reflectance can be more dependent on these assumptions than on the measurement errors; even if some idea of the size distribution can be derived from the spectral dependence of the optical thicknesses.

The approach in the irradiance-based method is to substitute the results of irradiance measurements into Equation 5.6. The assumptions made regarding the aerosol model will only affect the determinations of ρ_A and s needed to correct the irradiance measurements for the coupling term, $1-\rho s$, between ground and atmosphere. The contribution of ρ_A will be relatively small if the target is of high reflectance, as is the case at White Sands.

Relative contribution of atmospheric and ground reflectance

To determine the approximate relative magnitudes of the contributions from the atmosphere and the ground, I have used the 5S program developed by Tanré et al. (1986). This program uses approximations to compute the different reflectance components but is sufficiently accurate for this purpose. TM observations are considered both for summer ($\theta_s = 30^\circ$) and winter ($\theta_s = 60^\circ$) using a continental aerosol model and a visibility of 23 km. The ground reflectances correspond to measurements made at White Sands on 85.11.16 (Slater et al., 1986). Table 5.1 lists the ground reflectances and the optical thicknesses δ_A for aerosols and δ_R for Raleigh scattering for the solar-reflective TM bands on this date. I have also run the program for the same conditions but for the urban and maritime aerosol models available in the 5S program. The spectral dependencies of the optical thicknesses for the three models are shown in Figure 5.2. The continental and urban curves are close as these two models have almost the same size distribution. The main difference is the strong absorption included in the urban model. The spectral variations of the optical thicknesses are weak for the maritime model and indicate larger particles. The optical thicknesses, given in Table 5.1, correspond to the continental model. Accurate transmittance measurements would obviously allow precise modeling of the aerosols; but, for convenience,

I have kept the three models as representative of the errors of measurement and the large remaining uncertainty in the aerosol refractive index.

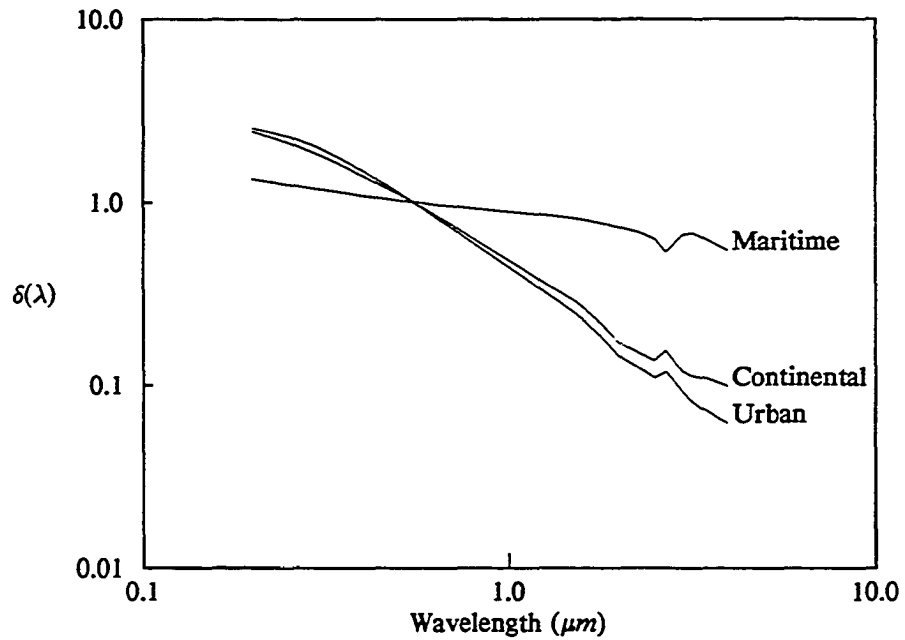


Figure 5.2. Spectral dependence of the normalized extinction coefficient for three aerosol models.

Table 5.1. Ground reflectances for the band centers of the solar reflective TM bands on 1985.11.16. Rayleigh optical depths are computed at sea level. Aerosol optical depths correspond to a visibility of 23 km for the continental model assumed.						
	<i>TM1</i>	<i>TM2</i>	<i>TM3</i>	<i>TM4</i>	<i>TM5</i>	<i>TM7</i>
ρ_G	0.4131	0.4805	0.5189	0.5629	0.3422	0.1116
δ_A	0.270	0.226	0.190	0.141	0.058	0.037
δ_R	0.160	0.083	0.045	0.018	0.001	0.000

The apparent reflectances are reported as a function of wavelength in Figure 5.3 for the three aerosol models and a summer mid-latitude solar zenith angle. The differences are almost the same for the visible TM bands, and decrease for the IR bands in relation to both the decreases of the ground reflectances and the atmospheric corrections. The maritime model corresponds to larger particles and so the large forward scattering peak increases the diffuse transmittance. Moreover, the absence of absorption ($\omega_0 = 1$) increases this term and gives rise to the largest apparent reflectance. The main difference between the continental and urban models is the strong absorption included in the urban model, the transmittance being higher for the continental model. Also included in Figure 5.3 are the atmospheric reflectances computed for the three models. The differences are negligible. This result is due to the fact that the Rayleigh background is the largest contributor, for example it is 0.06 out of the total of 0.08 for TM1. Figure 5.4 gives similar results but for a winter observation. For the larger solar zenith angle, the apparent reflectances are smaller. The global transmittances decrease but these are partially counter-balanced by an increase in the atmospheric reflectances. Slight differences appear in the atmospheric reflectances, caused by the longer atmospheric path. The main conclusion is that the determination of the transmittance is more critical than the determination of the atmospheric reflectance term for high ground reflectances. The last point concerns Equation 5.6 which expresses the global transmittance as a function of the global irradiance. The multiple interactions between the ground and the atmosphere appear in the term $1-\rho_s$. If the ground reflectance is assumed known, inaccuracies in determining ρ^* come from the determination of the spherical albedo.

Error Analysis

The error in the apparent reflectance due both to the determination of the atmospheric reflectance and to the correction by the term $1-\rho_s$ is easily derived by differentiating

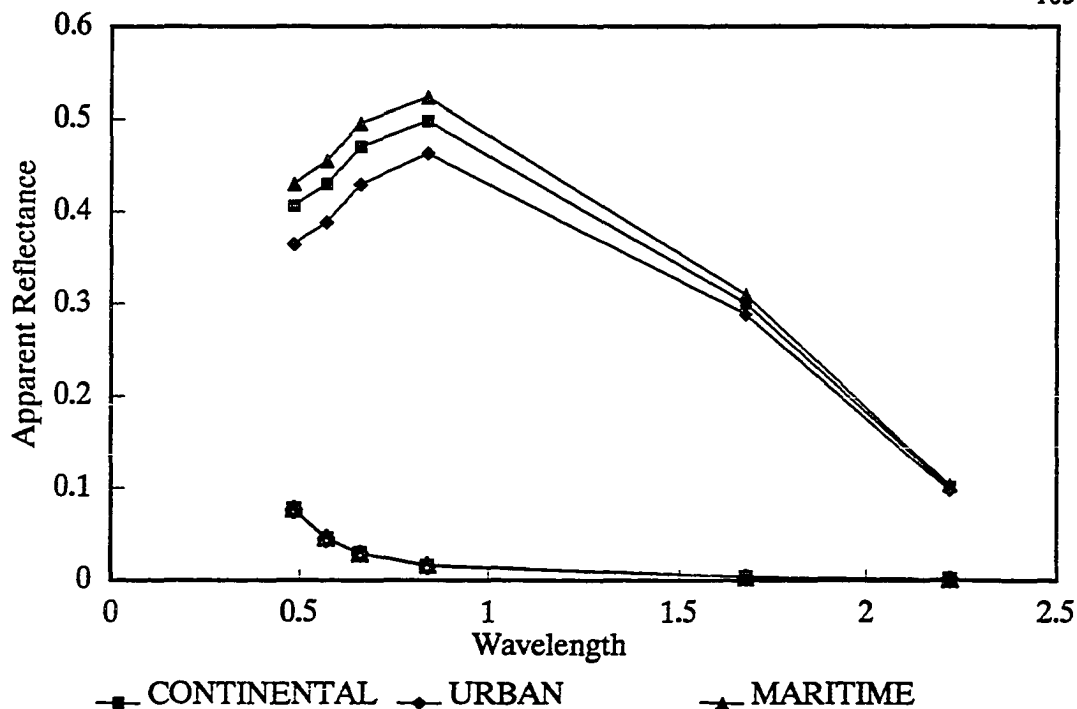


Figure 5.3. Computation of the apparent reflectances measured in the TM bands for three aerosol models and for a solar zenith angle of 30 degrees. The atmospheric reflectances are also plotted for the three models as the three overlapping curves at the bottom of the graph.

Equation 5.6, thus:

$$d\rho^*(\theta_s, \theta_v, \phi_v - \phi_s) = d\rho_A(\theta_s, \theta_v, \phi_v - \phi_s) - \frac{e^{-\delta/\mu_s}}{1-\alpha_s} \rho^2 \frac{e^{-\delta/\mu_v}}{1-\alpha_v} ds. \quad (5.7)$$

The spherical albedo s is an integrated value of the outward radiances; and so generally ds and $d\rho_A$ will have the same sign. Thus the two terms in Equation 5.6 will be counter-balanced in most cases. The continental model atmosphere is assumed to be the actual atmosphere and the $d\rho^*$ is given in Table 5.2 using the maritime and urban models both for summer and winter observations. Since 5S provides results to only three significant figures, some results will be affected by the round-off error. For summer observations, the errors in determining apparent reflectances have, for the maritime model, an average value of 0.003 for the visible bands and are less than the round-off errors in the infrared bands. They are

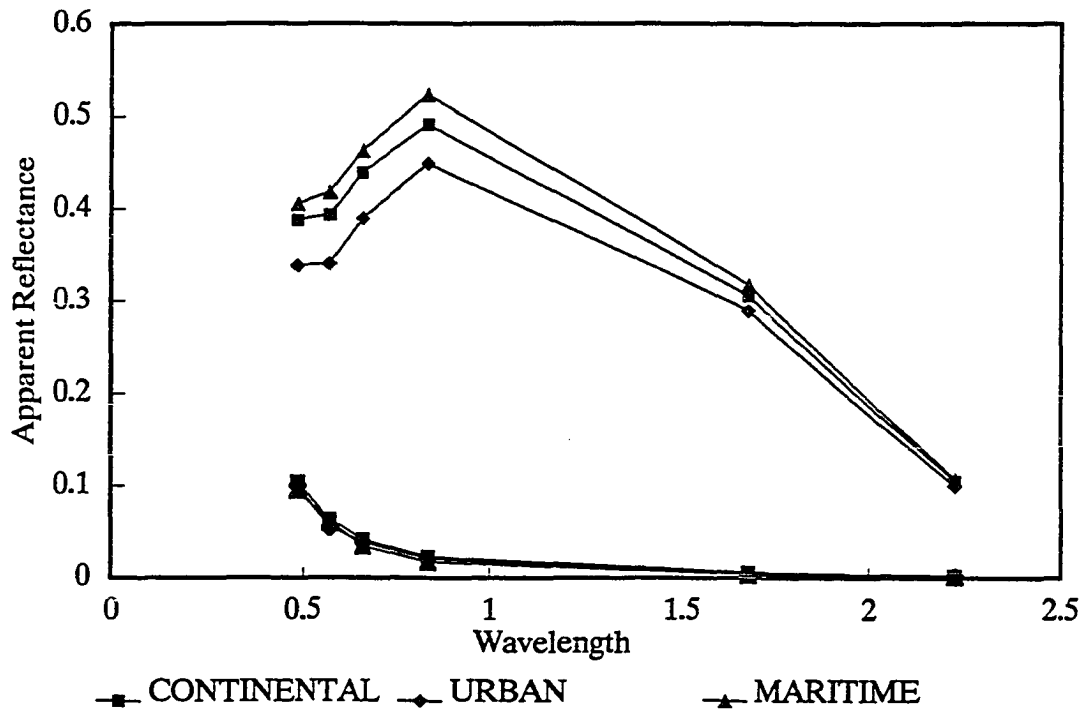


Figure 5.4. Computation of the apparent reflectances measured in the TM bands for three aerosol models and for a winter observation with a solar zenith angle of 60 degrees. The atmospheric reflectances are also plotted for the three models as the three overlapping curves at the bottom of the graph.

negligible for the urban model. The worst cases occur in the winter case for the maritime model, where the path radiance is higher. In terms of relative errors, the irradiance method leads to average inaccuracies of 0.5 percent, with an extreme value of 1.5 percent for a winter TMI observation and for the maritime model. Since the aerosol model can be improved, these errors will certainly be negligible compared to related errors in δ and α measurements.

Table 5.2. Estimation of the accuracy of the irradiance method. The errors in apparent reflectance are given in percent. <i>U</i> and <i>M</i> stand for urban and maritime model atmospheres. See text for details.							
		<i>TM1</i>	<i>TM2</i>	<i>TM3</i>	<i>TM4</i>	<i>TM5</i>	<i>TM7</i>
Summer	<i>U</i>	0.02	0.18	0.12	0.13	0.03	0.00
	<i>M</i>	0.15	0.31	0.27	0.32	0.01	0.01
Winter	<i>U</i>	-0.29	-0.55	-0.08	-0.41	0.6	0.00
	<i>M</i>	-0.74	-0.09	-0.40	-0.61	-0.18	0.00

I now consider the case of different ground reflectances. The apparent reflectances, computed for the three aerosol models, are plotted in Figure 5.5a versus the ground reflectance for winter TM1 observations. According to Equation 5.2, the apparent reflectance is almost linear as a function of the ground reflectance. The interpretation of the discrepancies between the models was described in the previous section. Generally low ground reflectances are observed in TM1 band from 0.025 for vegetation to 0.1 for bare soil. In this range, the errors in the apparent reflectances come from the differences both in the atmospheric reflectances and in the atmospheric transmittance. For TM4 and winter observations, Figure 5.5b, gives the same plot of the apparent reflectance versus the ground reflectance. For a vegetation reflectance of around 0.4, the difference between the continental and maritime model approaches 0.1. The inaccuracies of the irradiance method have been computed using Equation 5.6, and are reported in Table 5.3 for the reflectance range of 0 to 0.6 and for TM1 and TM4 observations in summer and winter. For the summer case, the errors are negligible. They remain acceptable if the urban model is

assumed. For the maritime model, the errors mainly come from the differences in the atmospheric reflectances. The decrease of the error with the ground reflectance illustrates the advantage of the irradiance method: the initial difference in the atmospheric reflectance is partially counter-balanced by the error in the irradiance correction involving the spherical albedo.

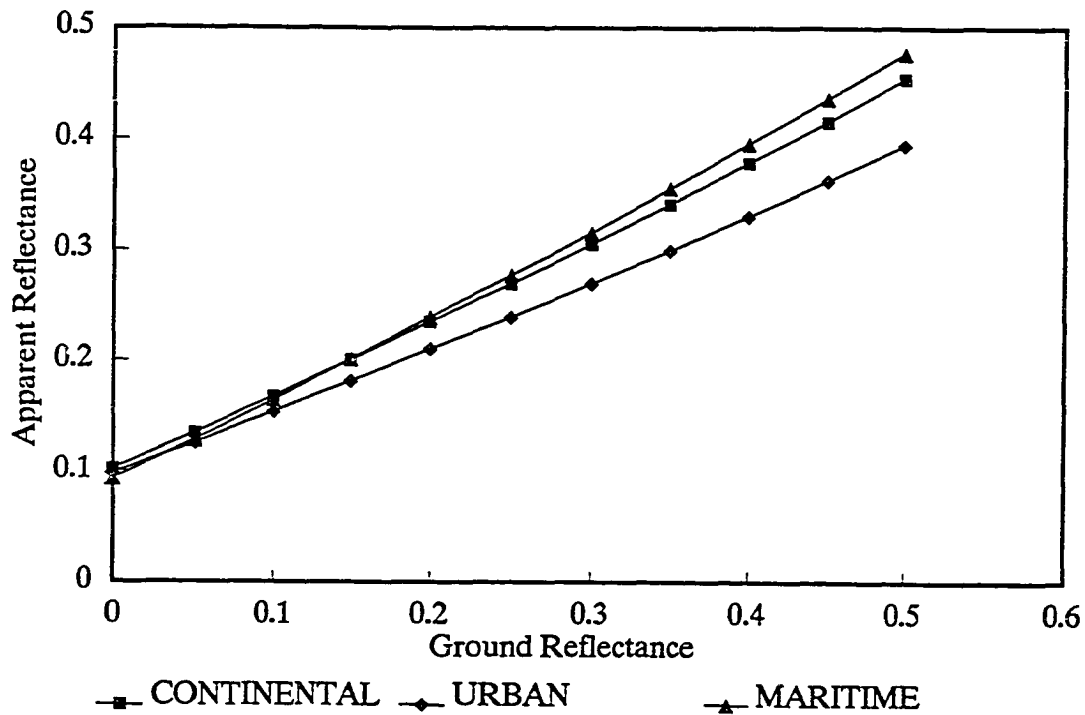


Figure 5.5a. Variation of the TM1 apparent reflectance computed for the three aerosol models versus the ground reflectances for the winter case.

The general conclusion is obvious: for large ground reflectance the irradiance method avoids a key assumption of the aerosol model and so removes large related inaccuracies. It may reduce significantly the time-consuming use of a transfer code since the corrective terms ρ_A and s can be evaluated using approximations.

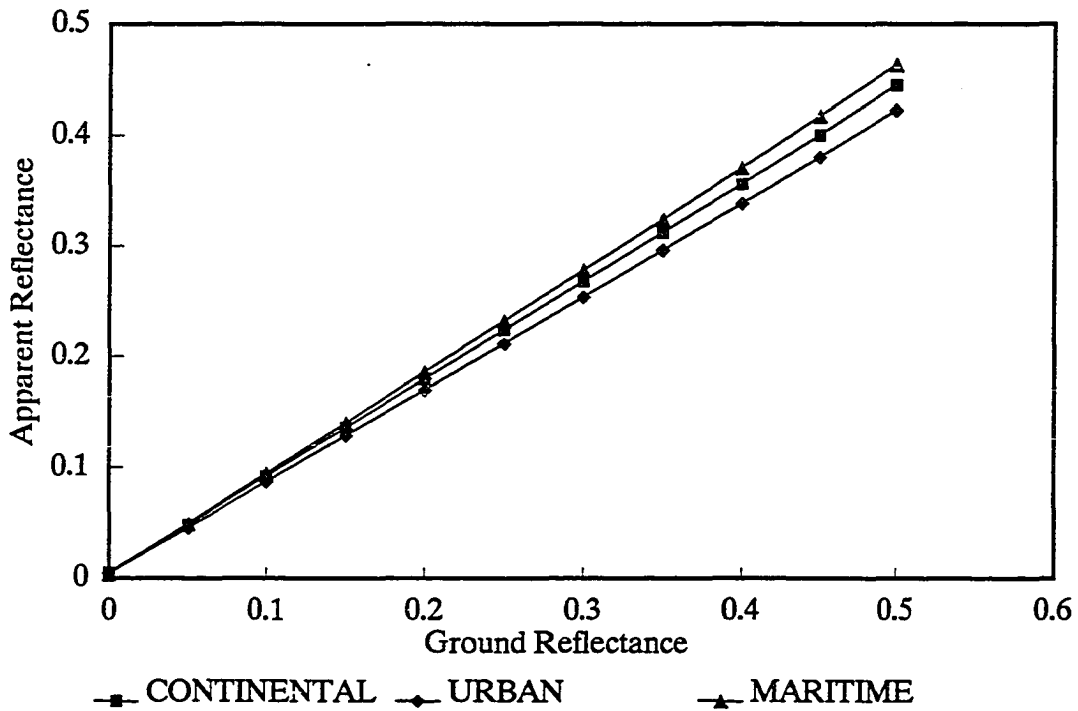


Figure 5.5b. Variation of the TM4 apparent reflectance computed for the three aerosol models versus the ground reflectances for the winter case.

Irradiance Measurements

Principle

The diffuse-to-global irradiance ratio can be determined from ground reflectance factor measurements using a BaSO_4 panel as reference. Figure 5.6a is a schematic of the measurements and of the different components of the measured radiance. Since the panel is nearly lambertian, the global $E_G(\mu_s)$ is proportional to the panel radiance $L_G(\mu_s)$ measured at nadir. In the same way, the diffuse irradiance $E_d(\mu_s)$ is obtained by measuring $L_d(\mu_s)$ by using an opaque parasol or shadower to remove the direct solar irradiance, Figure 5.6b.

Table 5.3. Estimation of the inaccuracy of the irradiance method for different ground reflectances. TM1 and TM4 observations.									
ρ ground		0.0	0.1	0.2	0.3	0.4	0.5	0.6	
Summer	TM1	U	-0.10	-0.09	-0.07	-0.04	0.01	0.08	0.17
		M	0.00	0.01	0.03	0.07	0.17	0.22	0.33
	TM4	U	-0.09	-0.09	-0.06	-0.03	0.02	0.08	0.16
		M	0.09	0.10	0.12	0.15	0.20	0.27	0.35
Winter	TM1	U	-0.39	-0.39	-0.37	-0.34	-0.30	-0.24	-0.16
		M	-0.88	-0.87	-0.85	-0.81	-0.75	-0.67	-1.56
	TM4	U	-0.19	-0.20	-0.22	-0.25	-0.30	-0.36	-0.44
		M	0.09	0.10	0.12	0.15	0.20	0.27	0.35

The two data sets give the diffuse-to-global ratio:

$$\frac{E_d(\mu_s)}{E_G(\mu_s)} = \frac{L_d(\mu_s)}{L_G(\mu_s)}. \quad (5.8)$$

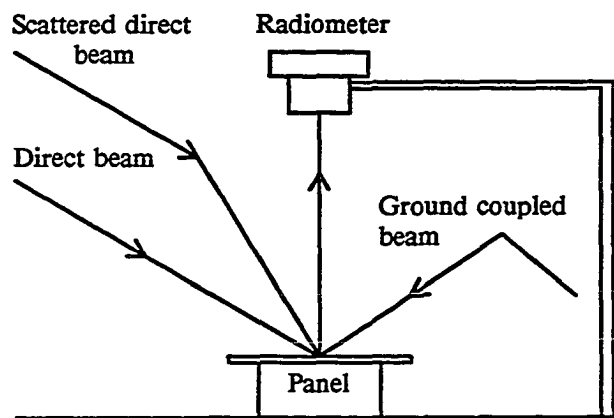


Figure 5.6a. Diffuse-to-global measurement setup -- Unshaded by parasol

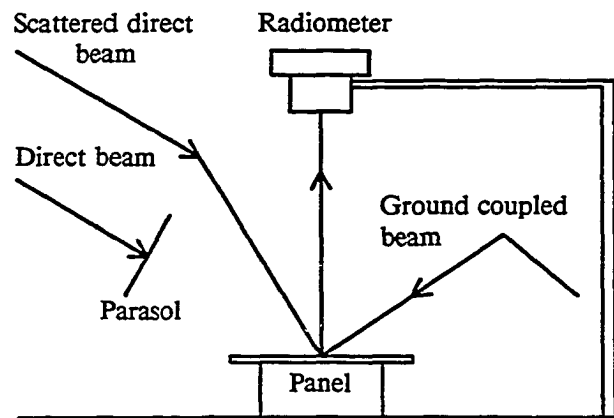


Figure 5.6b. Diffuse-to-global measurement setup -- Shaded by parasol

At the same time, extinction measurements give the total optical thickness δ ; the global irradiance can then be expressed by:

$$E_G(\mu_s) = \frac{\mu_s E_s e^{-\delta/\mu_s}}{1 - L_d(\mu_s)/L_G(\mu_s)} \quad (5.9)$$

At the time of satellite overpass, the global irradiance gives the downward transmittance.

From the reciprocity principle, the global transmittance for the upward path can be derived from measurements at the solar angle θ_s , equal to the viewing angle. There are two limitations to this approach. First, it assumes that the atmosphere is stable between the time of overpass and the measurements and variations in the atmospheric conditions will be attributed to variations in the aerosol content (i.e. the optical thickness) rather than changes in the aerosol properties. In many cases the stability of the atmosphere can be checked using the transmittance measurements and the Langley plot technique. In the second case, for TM observations, we need to extrapolate the diffuse-to-global ratio measurements made at noon to an air mass of 1 which is more difficult at higher latitudes. In this case, a knowledge of the behavior of the diffuse-to-global ratio versus the air mass can be helpful.

Figure 5.7 gives the diffuse-to-global ratio computed for TM1 versus the air mass. The continental model is assumed with a visibility of 23 kilometers; the two curves correspond respectively to a ground reflectance of 0.0 and 0.5. For a black ground, the diffuse-to-global ratio decreases with the air mass and is almost linear if $m < 2$. The contribution of the light reflected by the ground is more effective around noon, which gives rise to a slight increase in the diffuse-to-global ratio. For measurements made at noon, at White Sands, the air mass is 1.134 on April 1, and 1.015 on July 1. The inaccuracy of the linear interpolation will be then about 0.005 and near zero for a ground reflectance of 0.5 and thus tolerable.

For the case of satellite observations when the sensor view angle is small, the range of solar elevations may preclude the measurement of the diffuse-to-global ratio at the needed angle θ_v . In this case we need to extrapolate a series of measurements to the required angle. We can also use the following method to interpolate a value for α_s at θ_s if α was not measured at exactly the angle needed.

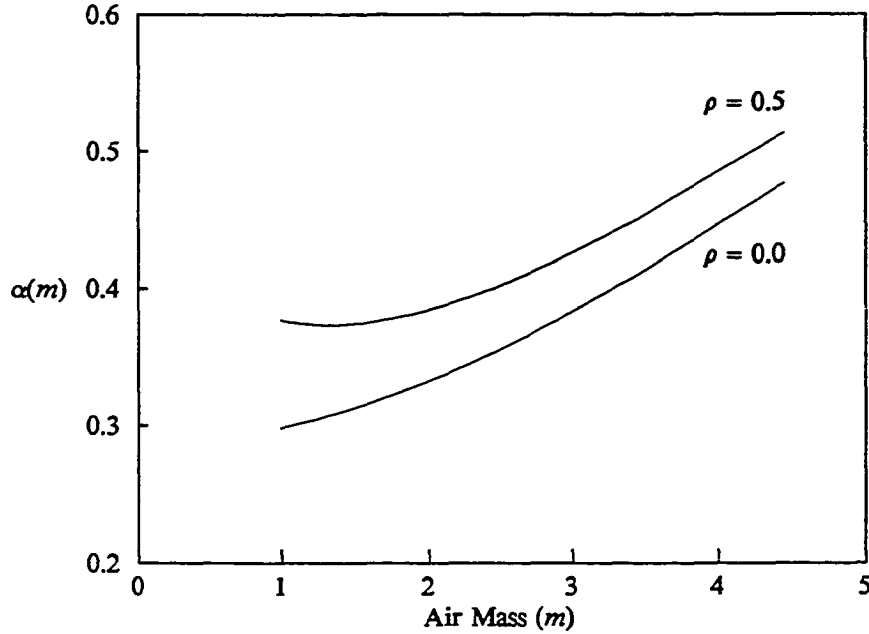


Figure 5.7. Diffuse-to-global ratio computed versus the air mass for TM1 band and ground reflectances of 0.0 and 0.5

The diffuse irradiance is defined to be E_d , the direct irradiance to be E_D , and the global irradiance to be E_G . The diffuse-to-global ratio is then:

$$\frac{E_d}{E_G} = \frac{E_G - \mu_s e^{-\delta/\mu_s} E_s}{E_G} = 1 - \frac{e^{-\delta/\mu_s}}{T(\mu_s)} \quad (5.10)$$

where $T(\mu_s)$ is the global atmospheric transmittance. Following the 5S approximations:

$$T(\mu_s) = \frac{e^{-\delta b/\mu_s}}{1-\rho s} \quad (5.11)$$

where s is the spherical albedo. Combining 5.10 and 5.11 we get

$$1 - \frac{E_d}{E_G} = \frac{e^{-\delta/\mu_s}}{T(\mu_s)} = (1-\rho s) e^{-\delta(1-b)/\mu_s} \quad (5.12)$$

or

$$\log \left(\frac{E_D}{E_G} \right) = \log(1-\rho s) - (1-b)\delta/\mu_s. \quad (5.13)$$

From the measurements of diffuse-to-global ratio we get

$$\alpha = \frac{E_d}{E_G} \text{ which gives } \frac{E_D}{E_G} = 1 - \alpha .$$

Now the airmass $m = 1/\mu_s$ and we have a set of datum points of the form of $y = y_0 + cm$ with the slope c being $-(1-b)\delta$ and the intercept y_0 being $\log(1-\rho_s)$. We can make a least squares fit of the transformed data to find $(1-b)\delta$. We then examine a log plot of the data ($\log(1-\alpha)$ versus m) to decide if the day was stable in a manner analogous to the Langley method for optical depths. If we have a stable day, we can use the fitted slope value to compute a value for α at both θ_v and θ_s .

Field Measurements

Previous work on TM calibration at White Sands has been reported by Slater et al. (1986). This work involved five one-day measurements and for two of them, 85.05.24 and 85.11.16, diffuse-to-global ratios were determined. These measurements were made in an attempt to determine the imaginary part of the aerosol refractive index. Comparisons were made between measured and calculated values of the ratio for this purpose by Phillips (1985). These measurements were only made near the time of overpass of the satellite and this time limitation does not allow the determination of the global transmittance for the upward path by extrapolation. Nevertheless, the 85.11.16 measurements provide a good check of the validity of the irradiance measurement method, because the high visibility corresponded to a near-Rayleigh atmosphere.

To complement this earlier work, we made more extensive diffuse-to-global measurements at White Sands during March 1987 (87.02.27: TM, 87.03.28: SPOT), July 1987 (87.07.17: SPOT), and February 1988 (88.02.08 and 88.02.09: SPOT, 88.02.10: TM). The conditions of the observations are presented in Table 5.4 both for TM and SPOT calibrations. A typical value for the Rayleigh optical thickness (88.02.10 with a barometric

pressure of 882.5 mb) is given with the ground reflectances and aerosol optical thicknesses measured for each day.

The Rayleigh optical thicknesses were computed from the measured barometric pressure. The global optical thicknesses were derived from extinction measurements. Very little gaseous absorption affects the bands at 0.44 μm and 0.868 μm . For these bands, a linear regression of a log-log plot of the aerosol optical thickness versus the wavelength was made after removing the Rayleigh component. The aerosol optical thicknesses for the satellite bands were deduced using this linear regression. In the Chappuis band, the ozone optical thicknesses were then deduced from the measurement after removing both the Rayleigh and aerosol optical thicknesses (the 2 point fit). For the February 1988 dates, the iterative method was used.

The diffuse-to-global ratio was measured using the technique described in the previous section. Two radiometers were used: An Exotech with bands simulating the first four TM bands or the SPOT spectral bands, and a Barnes MMR with bands simulating the six solar-reflective TM bands. These results are reported in Tables 5.5a-5.5g as a function of the time and of the corresponding air mass. Few measurements were made on 85.05.24 and 87.07.17. The extensive set obtained on 87.03.27 is plotted in Figure 5.8 for the TM1 band and as expected the diffuse-to-global ratio decreases with the air mass. The measurements were performed using a Barnes early in the morning and around noon and with the Exotech during the time of overpass. The higher values recorded using the Exotech correspond partially to a slight variation of the central wavelength of the two radiometers with respectively 0.488 μm for the Exotech and 0.491 μm for the Barnes. Around noon we used the Barnes to obtain an extensive set of 23 measurements for an air mass quite stable in the range 1.1662 to 1.1632. We made these measurements to get an idea of their repeatability and Table 5.6 presents for the TM bands the mean value of the diffuse-to-global ratio, the

Table 5.4. Optical thickness and ground reflectances for the White Sands calibrations.					
		<i>TM1</i>	<i>TM2</i>	<i>TM3</i>	<i>TM4</i>
	δ_R	0.1399	0.0728	0.0401	0.0153
85.05.24	ρ	0.4695	0.5345	0.5778	0.6143
	δ_A	0.1390	0.0959	0.0775	0.0708
85.11.16	ρ	0.4131	0.4805	0.5189	0.5629
	δ_A	0.0260	0.0212	0.0176	0.0131
87.03.27	ρ	0.3456	0.4042	0.4374	0.4895
	δ_A	0.1128	0.1020	0.0931	0.0801
88.02.10	ρ	0.3590	0.4137	0.4442	0.4920
	δ_A	0.0920	0.0834	0.0763	0.0660
		<i>XS1</i>	<i>XS2</i>	<i>XS3</i>	
	δ_R	0.0852	0.0422	0.0152	
87.03.28	ρ	0.3873	0.4306	0.4918	
	δ_A	0.0663	0.0611	0.0541	
87.07.17	ρ	0.5086	0.5435	0.5904	
	δ_A	0.0823	0.0687	0.0528	
88.02.08	ρ	0.3626	0.4087	0.4679	
	δ_A	0.0231	0.0184	0.0132	
87.02.09	ρ	0.3848	0.4277	0.4822	
	δ_A	0.0302	0.0257	0.0202	

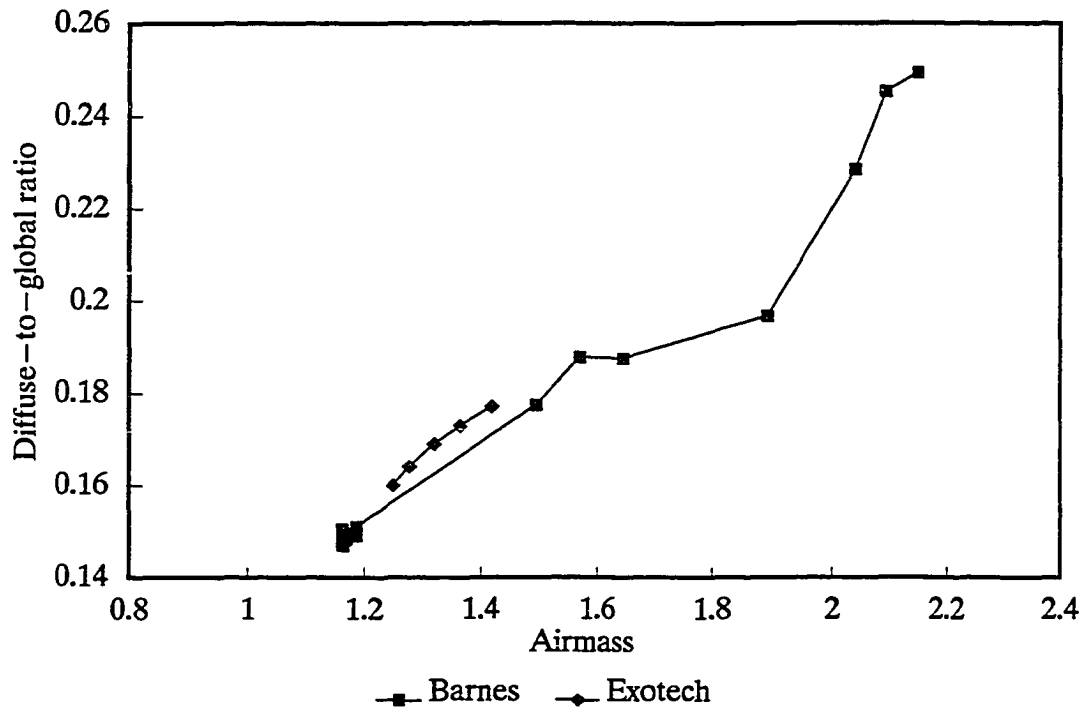


Figure 5.8. Diffuse-to-global ratio measured on 87.03.27 in the TM1 band.

1 σ standard deviation and the standard deviation in percent for 9 readings at the same airmass. The measurements are repeatable within about 1%. This result shows the reliability of this technique which is included in the careful measurement technique for determining the ground reflectance factor.

Table 5.5a. Diffuse-to-global ratio measurements at White Sands in 1985. The first set was done on 85.05.24 using a Barnes Radiometer. The second and third sets were for 85.11.16 using both the Barnes and an Exotech.

<i>Time</i>	<i>Airmass</i>	<i>Wavelength (μm)</i>						
		<i>0.4909</i>	<i>0.5622</i>	<i>0.6632</i>	<i>0.8117</i>	<i>1.254</i>	<i>1.688</i>	<i>2.217</i>
9.2281	1.276	0.239	0.184	0.134	0.098	0.053	0.041	0.026
10.5300	1.085	0.202	0.157	0.115	0.085	0.045	0.035	0.022
9.3558	2.125	0.194	0.138	0.094	0.073	0.046	0.037	0.024
9.4331	2.087	0.191	0.135	0.091	0.070	0.044	0.035	0.022
9.5025	2.052	0.188	0.133	0.090	0.069	0.042	0.034	0.021
9.8419	1.907	0.178	0.128	0.087	0.066	0.040	0.032	0.020
10.0542	1.836	0.171	0.122	0.083	0.062	0.037	0.030	0.020
10.4714	1.729	0.164	0.118	0.080	0.062	0.037	0.028	0.018
<i>Time</i>	<i>Airmass</i>	<i>Wavelength (μm)</i>						
		<i>0.4863</i>	<i>0.5706</i>	<i>0.6607</i>	<i>0.8382</i>			
9.2161	2.211	0.213	0.141	0.093	0.069			
9.2562	2.186	0.212	0.139	0.092	0.069			
9.4792	2.062	0.202	0.133	0.087	0.065			
9.5189	2.043	0.199	0.131	0.086	0.064			
9.8172	1.916	0.189	0.125	0.082	0.059			
10.0235	1.845	0.179	0.122	0.076	0.054			
10.2206	1.788	0.179	0.118	0.076	0.053			
10.4336	1.738	0.173	0.114	0.074	0.053			
10.6372	1.697	0.169	0.112	0.072	0.052			
10.8081	1.670	0.167	0.110	0.071	0.051			

Table 5.5b. Diffuse-to-global ratio measurements using the Barnes on 87.03.27 at White Sands.

Time	θ_s	Airmass	Diffuse/global					
			TM1	TM2	TM3	TM4	TM5	TM7
8.3231	62.27	2.149	0.2492	0.1917	0.1422	0.1084	0.0763	0.0636
8.3908	61.45	2.093	0.2452	0.1885	0.1405	0.1076	0.0761	0.0634
8.4572	60.66	2.041	0.2285	0.1754	0.1301	0.0990	0.0698	0.0583
8.6742	58.08	1.891	0.1966	0.1488	0.1883	0.0805	0.0557	0.0473
9.1500	52.58	1.646	0.1874	0.1415	0.1021	0.0753	0.0515	0.0440
9.3444	50.40	1.569	0.1877	0.1417	0.1020	0.0750	0.0503	0.0434
9.5633	48.02	1.495	0.1775	0.1336	0.0963	0.0705	0.0485	0.0417
11.4261	32.58	1.187	0.1510	0.1135	0.0809	0.0593	0.0405	0.0355
11.4325	32.55	1.186	0.1489	0.1125	0.0801	0.0585	0.0401	0.0356
11.7442	31.39	1.172	0.1494	0.1129	0.0812	0.0598	0.0410	0.0358
11.7525	31.37	1.171	0.1489	0.1130	0.0811	0.0595	0.0408	0.0361
11.7586	31.35	1.171	0.1486	0.1123	0.0804	0.0592	0.0403	0.0352
11.7744	31.31	1.171	0.1482	0.1124	0.0811	0.0597	0.0412	0.0362
11.9381	30.97	1.166	0.1483	0.1121	0.0806	0.0595	0.0410	0.0360
11.9481	30.95	1.166	0.1496	0.1141	0.0822	0.0606	0.0420	0.0371
11.9547	30.94	1.166	0.1485	0.1126	0.0808	0.0598	0.0414	0.0363
11.9614	30.93	1.166	0.1480	0.1124	0.0812	0.0598	0.0417	0.0367
11.9694	30.92	1.166	0.1484	0.1125	0.0211	0.0597	0.0415	0.0364
11.9775	30.91	1.166	0.1479	0.1123	0.0811	0.0597	0.0414	0.0364
11.9833	30.90	1.165	0.1489	0.1131	0.0814	0.0603	0.0418	0.0368
11.9900	30.89	1.165	0.1469	0.1115	0.0805	0.0590	0.0410	0.0359
11.9964	30.88	1.165	0.1485	0.1122	0.0809	0.0597	0.0412	0.0361
12.0042	30.87	1.165	0.1491	0.1135	0.0819	0.0603	0.0418	0.0369
12.0100	30.87	1.165	0.1489	0.1126	0.0809	0.0598	0.0413	0.0361
12.0158	30.86	1.165	0.1475	0.1120	0.0806	0.0596	0.0411	0.0362
12.0217	30.85	1.165	0.1488	0.1132	0.0812	0.0601	0.0416	0.0369
12.0300	30.85	1.165	0.1478	0.1124	0.0809	0.0597	0.0414	0.0364
12.1736	30.77	1.164	0.1464	0.1123	0.0815	0.0609	0.0429	0.0377
12.1803	30.77	1.164	0.1477	0.1130	0.0818	0.0610	0.0429	0.0382
12.1856	30.76	1.164	0.1485	0.1127	0.0816	0.0611	0.0429	0.0378
12.1917	30.76	1.164	0.1487	0.1135	0.0824	0.0615	0.0434	0.0385
12.1972	30.77	1.164	0.1480	0.1130	0.0820	0.0614	0.0432	0.0380
12.2042	30.77	1.164	0.1489	0.1138	0.0829	0.0617	0.0435	0.0389
12.2103	30.77	1.164	0.1500	0.1146	0.0832	0.0623	0.0437	0.0383
12.2192	30.77	1.164	0.1504	0.1157	0.0842	0.0629	0.0441	0.0390
12.2275	30.77	1.164	0.1500	0.1146	0.0885	0.0625	0.0448	0.0386

Table 5.5c. Diffuse-to-direct measurements with Exotech at White Sands on 87.07.17.						
<i>Time</i>	θ_s	<i>Airmass</i>	<i>Band</i>			
			<i>XS1</i>	<i>XS2</i>	<i>XS3</i>	
9.9559	44.13	1.39	0.135	0.094	0.080	
10.1107	42.24	1.35	0.147	0.106	0.095	
10.4835	37.6	1.26	0.123	0.084	0.071	
			<i>TM1</i>	<i>TM2</i>	<i>TM3</i>	<i>TM4</i>
11.1345	29.5	1.15	0.107	0.106	0.075	0.060
11.4802	25.37	1.11	0.134	0.133	0.106	0.102
11.6135	23.85	1.09	0.100	0.100	0.068	0.062

Table 5.5d. Diffuse-to-global ratio for White Sands on 87.03.28, for SPOT using Panel 11.				
<i>Time</i>	<i>Band</i>			
	<i>Pan</i>	<i>XS1</i>	<i>XS2</i>	<i>XS3</i>
11.0031	0.113	0.134	0.088	0.079
11.2128	0.126	0.143	0.099	0.089
11.4297	0.205	0.219	0.182	0.174
	<i>TM1</i>	<i>TM2</i>	<i>TM3</i>	<i>TM4</i>
11.0944	0.165	0.121	0.093	0.075
11.3478	0.205	0.165	0.139	0.124
11.6797	0.244	0.210	0.191	0.180

Table 5.5e. Diffuse-to-global ratio measurements using the Exotech on 88.02.08 at White Sands.

<i>Time</i>	θ_s	<i>Airmass</i>	Diffuse/global		
			<i>XS1</i>	<i>XS2</i>	<i>XS3</i>
10.5480	54.51	1.722	0.124	0.067	0.051
10.9364	52.13	1.629	0.118	0.066	0.048
11.4482	49.78	1.549	0.111	0.064	0.047
11.6815	49.04	1.525	0.109	0.063	0.046
11.7952	48.76	1.517	0.109	0.063	0.046
11.9142	48.52	1.510	0.109	0.062	0.046
12.4046	48.16	1.499	0.106	0.061	0.045
12.9370	48.92	1.522	0.111	0.065	0.046
13.3970	50.50	1.572	0.112	0.066	0.046
13.8725	52.97	1.660	0.122	0.072	0.049
14.4503	56.92	1.832	0.137	0.081	0.053
14.8503	60.24	2.015	0.148	0.088	0.057
15.3551	64.76	2.345	0.166	0.099	0.062
15.9011	70.21	2.954	0.199	0.119	0.073
16.2806	74.24	3.682	0.239	0.143	0.087
16.4028	75.58	4.016	0.259	0.155	0.092

Table 5.5f. Diffuse-to-global ratio measurements using the Exotech on 88.02.09 at White Sands.

<i>Time</i>	θ_s	<i>Airmass</i>	<i>Diffuse/global</i>		
			<i>XS1</i>	<i>XS2</i>	<i>XS3</i>
7.5971	82.87	8.057	0.460	0.276	0.174
7.7590	81.00	6.392	0.393	0.238	0.151
7.9040	79.35	5.411	0.350	0.214	0.137
8.0729	77.45	4.602	0.306	0.188	0.122
8.1938	76.10	4.163	0.286	0.175	0.113
8.2938	75.00	3.864	0.268	0.164	0.108
8.4733	73.05	3.430	0.238	0.146	0.097
8.7163	70.47	2.991	0.211	0.131	0.088
8.8486	69.09	2.802	0.199	0.124	0.082
9.0847	66.70	2.528	0.181	0.113	0.076
9.1951	65.61	2.422	0.175	0.110	0.074
9.5624	62.14	2.140	0.158	0.099	0.068
9.6783	61.09	2.069	0.154	0.097	0.066
9.9742	58.55	1.917	0.144	0.091	0.063
10.0954	57.57	1.865	0.141	0.089	0.062
10.3612	55.54	1.767	0.135	0.086	0.060
10.4806	54.69	1.730	0.132	0.084	0.059
10.8064	52.59	1.646	0.128	0.082	0.057
10.9153	51.96	1.623	0.126	0.081	0.057
11.0443	51.27	1.598	0.125	0.080	0.057

Table 5.5g. Diffuse-to-global ratio measurements using the Barnes on 88.02.10 at White Sands.

Time	θ_s	Airmass	Diffuse/global					
			TM1	TM2	TM3	TM4	TM5	TM7
8.0622	77.37	4.573	0.491	0.393	0.304	0.240	0.139	0.101
8.1561	76.32	4.228	0.461	0.367	0.282	0.223	0.128	0.092
8.2403	75.38	3.962	0.433	0.343	0.262	0.206	0.117	0.084
8.3444	74.24	3.682	0.406	0.320	0.243	0.190	0.108	0.077
8.4264	73.35	3.490	0.388	0.304	0.230	0.180	0.102	0.073
8.5353	72.17	3.266	0.367	0.288	0.218	0.170	0.096	0.068
8.6550	70.90	3.056	0.348	0.272	0.206	0.161	0.091	0.064
8.8442	68.92	2.780	0.324	0.253	0.192	0.150	0.085	0.060
9.0447	66.87	2.546	0.303	0.237	0.180	0.141	0.081	0.057
9.3719	63.67	2.255	0.274	0.214	0.162	0.127	0.073	0.051
9.5967	61.58	2.101	0.260	0.204	0.154	0.121	0.070	0.049
9.7750	59.99	1.999	0.249	0.195	0.147	0.116	0.067	0.047
10.0131	57.97	1.886	0.234	0.183	0.138	0.108	0.063	0.044
10.2272	56.27	1.801	0.223	0.174	0.131	0.103	0.060	0.042
10.8844	51.84	1.618	0.205	0.161	0.121	0.094	0.055	0.039
11.1550	50.42	1.569	0.197	0.153	0.115	0.090	0.053	0.037
11.3372	49.60	1.543	0.192	0.150	0.112	0.087	0.051	0.036
11.6172	48.60	1.512	0.188	0.146	0.109	0.084	0.049	0.035

Corrections to the diffuse-to-global ratio related to the non-lambertian properties of the $BaSO_4$ panel

Figure 5.9 gives the reflectance factor $R(\theta)$ of the $BaSO_4$ panel used for the field measurements. If we take into account the non-lambertian properties of the panel, we then get from equation 5.4:

$$\alpha = \frac{\iint \mu L(\mu, \mu_s, \phi - \phi_s) R(\mu, \mu_s, \phi - \phi_s) d\mu d\phi}{\mu_s E_s R(\theta) + \iint \mu L(\mu, \mu_s, \phi - \phi_s) R(\mu, \mu_s, \phi - \phi_s) d\mu d\phi} \quad (5.14)$$

Table 5.6. Diffuse-to-global ratio variability data from measurements using the Barnes on 87.03.27 at White Sands.								
	$\langle \theta_s \rangle$	$\langle m \rangle$	<i>TM1</i>	<i>TM2</i>	<i>TM3</i>	<i>TM4</i>	<i>TM5</i>	<i>TM7</i>
mean	30.7662	1.1638	0.1490	0.1137	0.0826	0.0617	0.0434	0.0383
σ	0.00174	0.00002	0.0010	0.0011	0.0009	0.0007	0.0005	0.0005
σ (%)	0.005	0.002	0.64	0.96	1.14	1.16	1.08	1.20

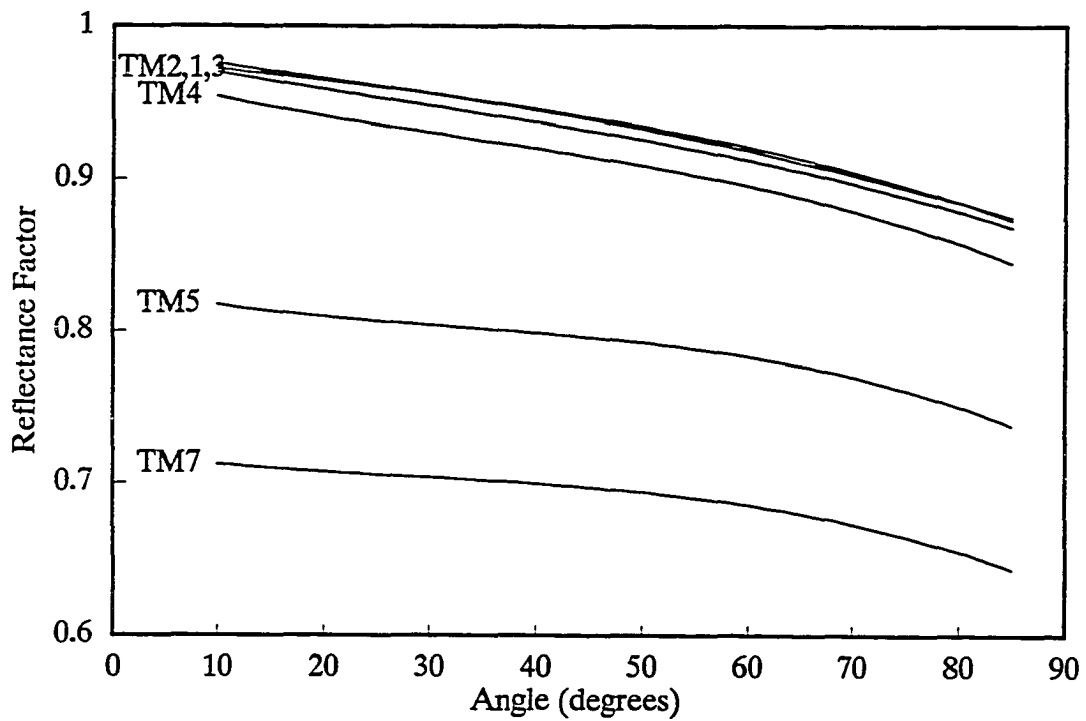


Figure 5.9. Reflectance factor of BaSO₄ panel 11.

Using a Fourier series expansion of the radiance in azimuth and making the reasonable assumption that the reflectance factor of the panel is independent of the azimuth, equation 5.14 becomes:

$$\alpha = \frac{2\pi \int_0^1 R(\mu) L^0(\mu, \mu_s) \mu d\mu}{\mu_s E_s R(\theta) + 2\pi \int_0^1 R(\mu) L^0(\mu, \mu_s) \mu d\mu} \quad (5.15)$$

where L^0 is the zeroth term of the Fourier series. This last equation is easily computed using a transfer code which uses a Fourier series expansion as does the successive order code developed by Deuzé (1974). We then compute the diffuse-to-global ratio in the TM1 band versus the solar zenith angle both for a pure molecular atmosphere and for a visibility of 23 km assuming the continental aerosol model. In Table 5.7 we compare the simulated measurements as affected by the non-lambertian panel with $R(\theta)$ as shown in Figure 5.9. Differentiating equation 5.6, we can compute the error in the apparent reflectance due to the change in α caused by the imperfect panel:

$$d\rho^* = - \frac{e^{-\delta/\mu_s}}{(1-\alpha_s)^2} d\alpha_s \rho(1-\rho_s) \frac{e^{-\delta/\mu_v}}{1-\alpha_v} - \frac{e^{-\delta/\mu_s}}{1-\alpha_s} d\alpha_v \rho(1-\rho_s) \frac{e^{-\delta/\mu_v}}{(1-\alpha_v)^2} \quad (5.16)$$

Table 5.8 gives the resulting errors in the apparent reflectance ρ^* for a ground reflectance of $\rho = 0.5$ and a view zenith angle of about 10 degrees for both a molecular atmosphere and an atmosphere with aerosols resulting in a visibility of 23 km. In both cases, the resulting errors are quite small.

Truncated diffuse irradiance

When shading the panel in order to stop the direct solar beam, the forward part of the diffuse light is removed also. I shall now estimate the magnitude of this forward diffuse light.

Table 5.7. Simulated diffuse-to-global ratios for perfect and non-lambertian panel and Rayleigh and 23 Km visibility atmospheres.

Solar Zenith Angle	Rayleigh		23 Km	
	Lambertian	Non	Lambertian	Non
2.841	0.178	0.167	0.377	0.362
6.521	0.178	0.168	0.377	0.363
10.223	0.177	0.168	0.376	0.364
13.930	0.177	0.168	0.376	0.365
17.638	0.176	0.167	0.376	0.365
21.348	0.175	0.167	0.375	0.365
25.058	0.174	0.166	0.374	0.365
28.768	0.172	0.165	0.374	0.365
32.479	0.171	0.164	0.373	0.365
36.190	0.169	0.163	0.373	0.366
39.901	0.167	0.162	0.373	0.366
43.611	0.165	0.161	0.373	0.367
47.322	0.163	0.160	0.373	0.369
51.033	0.162	0.159	0.375	0.372
54.744	0.160	0.158	0.377	0.376
58.455	0.159	0.158	0.381	0.382
62.167	0.158	0.159	0.388	0.391
65.878	0.158	0.161	0.399	0.406
69.589	0.159	0.164	0.418	0.428
73.300	0.163	0.171	0.451	0.466
77.011	0.173	0.184	0.513	0.533
80.722	0.199	0.214	0.641	0.664
84.433	0.290	0.316	0.885	0.898
88.144	0.920	0.931	1.000	1.000

Solid angle estimate

Figure 5.10 gives the approximate setup used for shadowing the panel. The parasol is a square piece of sheet aluminum about 0.9-m square which is painted black. It is fastened to a pole about 3.7-m long. The panel is placed on a stand which positions it about 30 cm horizontally above ground level. The panel is a square with sides of about 56 cm. The

Table 5.8. Errors in apparent reflectance for Rayleigh and 23 Km-visibility atmospheres for a view zenith angle of 10 degrees.		
Solar Zenith Angle	Rayleigh	23 Km Visibility
2.841	-0.013	-0.017
6.521	-0.013	-0.016
10.223	-0.012	-0.016
13.930	-0.012	-0.015
17.638	-0.011	-0.015
21.348	-0.011	-0.014
25.058	-0.011	-0.014
28.768	-0.010	-0.013
32.479	-0.010	-0.012
36.190	-0.009	-0.012
39.901	-0.009	-0.011
43.611	-0.008	-0.010
47.322	-0.008	-0.009
51.033	-0.007	-0.008
54.744	-0.006	-0.007
58.455	-0.005	-0.006
62.167	-0.004	-0.004
65.878	-0.003	-0.003
69.589	-0.002	-0.002
73.300	-0.001	-0.000
77.011	0.000	0.001
80.722	0.002	0.003
84.433	0.004	0.013
88.144	0.010	0.024

radiometer is placed over the panel looking vertically down with a field of view of 15 degrees. The radiometer is less than 1 meter above the panel and care is taken to insure that no shadows from the radiometer are in its field of view. A reading V_1 is taken with the parasol shadow off the panel. Then the parasol is moved into position to just shadow the

panel. A new reading V_2 is taken. The parasol is moved aside and a new total reading V_3 is taken. The measured diffuse-to-global ratio is calculated as

$$\alpha = \frac{2 V_2}{V_1 + V_3}.$$

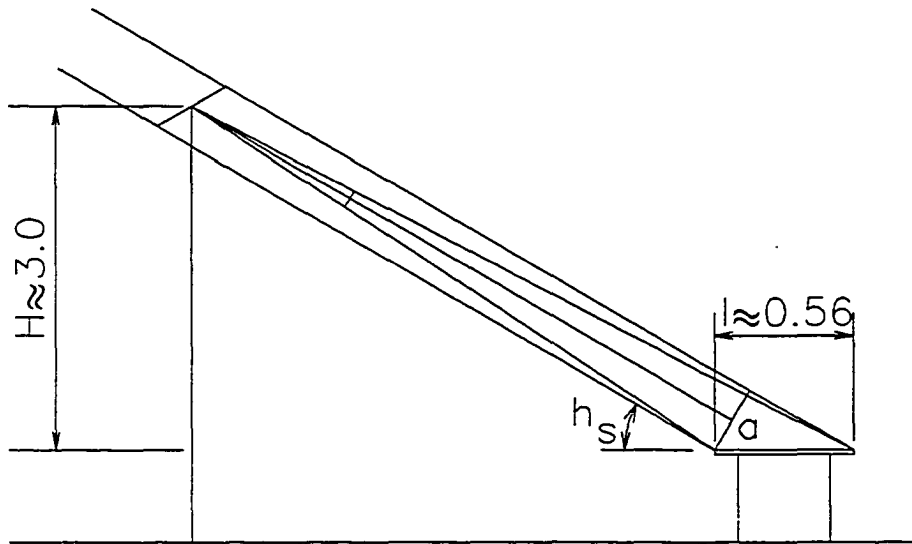


Figure 5.10. Panel and parasol geometry.

Computation of the irradiance

The forward radiance L is mainly due to primary scattering and can be expressed as:

$$L(\mu, \mu_s, \phi - \phi_s) = \frac{\delta}{\mu} e^{-\delta/\mu} E_s \frac{P(\Theta)}{4\pi} \quad (5.17)$$

Figure 5.11 gives the angles used in the following computations. The diffuse irradiance in the solid angle Ω is given by

$$E_d^\Omega = \int_{\phi} \int_{\mu} \mu L(\mu, \mu_s, \phi - \phi_s) d\phi d\mu . \quad (5.18)$$

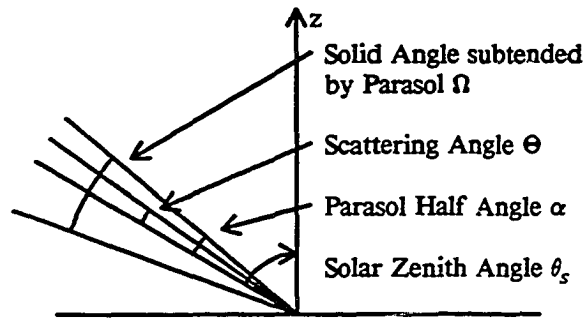


Figure 5.11. Angle definitions for diffuse correction

For a small parasol and corresponding small solid angle Ω , $\mu \simeq \mu_s$ which allows us to simplify Equation 5.18 to

$$E_d^\Omega = \frac{\delta E_s}{4\pi} e^{-\delta/\mu_s} \int_0^{2\pi} d\phi \int_1^{\cos\alpha} P(\Theta) d(\cos\theta) \quad (5.19)$$

or

$$E_d^\Omega = E_s e^{-\delta/\mu_s} \frac{\delta A}{2} \quad (5.20)$$

if A is defined as the integral of the phase function P between $\Theta = 0$ and $\Theta = \alpha$. For an atmosphere which provides a mixture of Rayleigh and aerosol scattering:

$$\delta A \simeq 1.5 \delta_R + \delta_A A_a . \quad (5.21)$$

A_a is computed by assuming an aerosol model. Our measurements of the diffuse-to-global ratio are

$$\alpha = \frac{E_d - E_d^\Omega}{E_G} \quad (5.22)$$

A short manipulation shows that the real value of α^* corrected for the blocked diffuse component is given by:

$$\alpha^* = \frac{\alpha + \frac{\delta A}{2\mu_s}}{1 + \frac{\delta A}{2\mu_s}} \quad (5.23)$$

The percentage change in the diffuse-to-global ratio on 88.02.10 due to the diffuse correction is given in Table 5.9 for various solar angles. The corrections for this effect are small unless the solid angle is large or the $\delta A/2\mu_s$ correction term is comparable to α . As α is smaller for longer wavelengths, the correction increases with wavelength. The correction also increases for smaller zenith angles as the parasol is closer to the panel with a consequent increase in the solid angle.

Comparison of the reflectance- and irradiance-based methods

In the reflectance-based method the radiance at the satellite level was computed using a transfer code with a boundary condition of a lambertian ground with the measured value of the reflectance. The Junge size distribution used to describe the aerosol size distribution had a slope determined from the spectral optical depths and the effective complex refractive index of the aerosol particles was assumed to be $m = 1.54 - 0.01i$.

For the irradiance-based method, according to equation 5.6, corrected measurements of α_s and α_v were used while ρ_A and s were computed using either a radiative transfer code or 5S with an input of a continental model and measured aerosol optical depths. Since differences between the two methods will derive from differences in the global irradiance estimate, I shall first compare this term.

Comparison of the measured diffuse-to-global ratio to an estimate using a transfer code

A ground reflectance of 0.5 was used. The successive order program (Deuzé, 1974), used to compute the apparent reflectance, also provided the diffuse downward irradiance.

Table 5.9. Percentage increase in diffuse-to-global ratio on 88.02.10 due to diffuse correction according to equation 4.23.				
<i>Zenith Angle</i>	<i>TM1</i>	<i>TM2</i>	<i>TM3</i>	<i>TM4</i>
77.37	0.14	0.20	0.26	0.33
76.32	0.15	0.22	0.28	0.31
75.38	0.16	0.20	0.30	0.34
74.24	0.30	0.41	0.53	0.63
73.35	0.31	0.39	0.52	0.61
72.17	0.33	0.42	0.55	0.64
70.90	0.49	0.62	0.82	0.99
68.92	0.71	0.90	1.14	1.32
66.87	0.92	1.17	1.49	1.76
63.67	1.20	1.53	1.96	2.18
61.58	1.49	1.85	2.31	2.69
59.99	1.79	2.18	2.82	3.14
57.97	2.45	2.96	3.77	4.26
56.27	2.79	3.39	4.26	4.83
51.84	3.36	4.08	5.15	5.79
50.42	3.74	4.54	5.66	6.45
49.60	4.08	4.88	6.23	6.99
48.60	4.12	4.94	6.22	7.12

The computed diffuse-to-global ratios are given in Figure 5.12. For 85.11.16, a complementary run has been made for the Rayleigh case. The two runs are represented by error bars. The computations agree well in the first three bands. For this clear day, Rayleigh scattering dominates for the visible bands and the fit validates the measurements. A slight tendency can be noted for the computations to underestimate the measurements toward the longer wavelengths. We have not reported in the figure the SWIR measurements; at 2.2 μm an extrapolated aerosol optical thickness of nearly zero leads to a computed diffuse irradiance equal to about zero whereas measurements indicate a diffuse-to-global

ratio equal to 0.02. The degradation in the comparison between the measurements and the computations in the SWIR, mainly at $2.2 \mu\text{m}$ is obviously due to the underestimation of the optical thicknesses. The SWIR optical thicknesses have been extrapolated and the underestimate results from an overestimation of the slope of the Junge parameter.

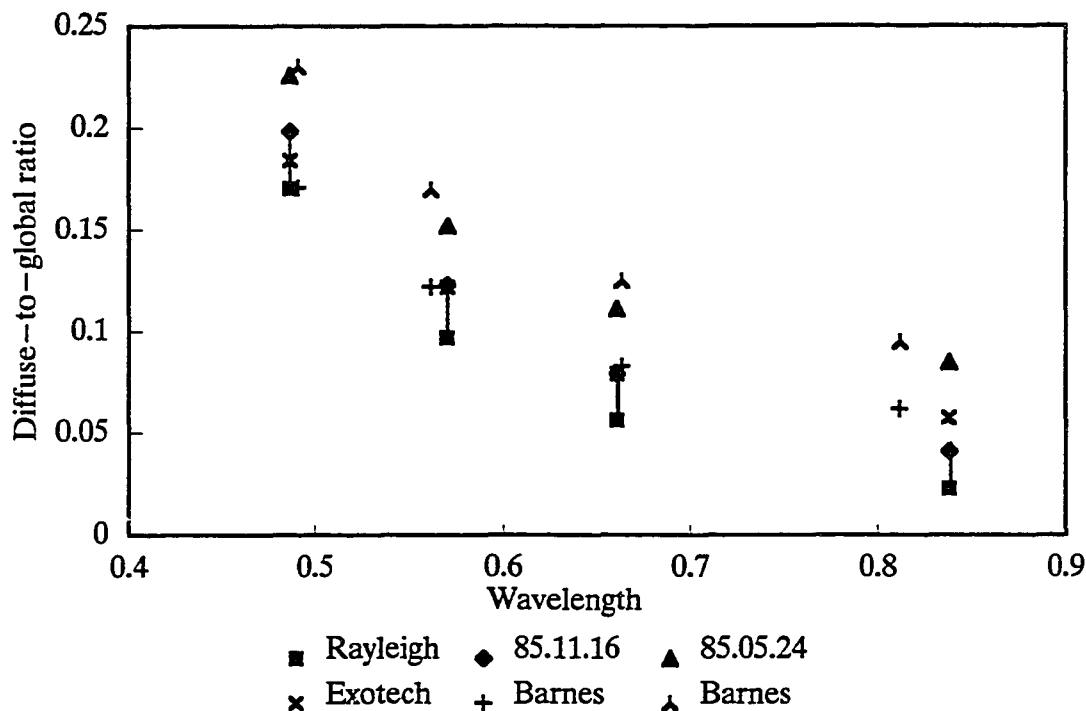


Figure 5.12. Diffuse-to-global ratio measured at TM overpass time. On 85.11.16 using the Exotech (x) and the Barnes (+); on 85.05.24 using the Barnes (inverted y). Comparison of the diffuse-to-global ratio computed according to the tabulated conditions for 85.11.16 (diamond) and 85.05.24 (triangle). For 85.11.16, the computations were also made for the Rayleigh case (square) and connected by bars to ratios for the total atmosphere case.

For 85.05.24, the measurements are higher than predicted by the successive order code computations. Of the several explanations possible, the most likely ascribes the disagreements to the atmospheric models used. On the other hand, for 85.11.16, we have already pointed out that the Junge parameter was overestimated. The effect of this on the aerosol size distribution is to reduce the number of particles with large sizes; consequently the diffuse downward irradiance is under-evaluated because the forward-scattering peak is

smaller than it should be. Finally, the imaginary part of the refractive index is assumed to be 0.01; and this value may be too large for the aerosols observed at White Sands. The result is again to under-evaluate the diffuse irradiance.

The overall conclusion to this section is that the good fit between measurements and theoretical predictions when Rayleigh scattering predominates (i.e. for short wavelengths (TM1) and clear days) gives us confidence in the measurement quality. The original reason for making the irradiance measurements was to attempt to derive the single scattering albedo (or the imaginary part of the refractive index). Such an attempt needs a good description of the size distribution. The Junge distribution assumed is probably not accurate enough to infer the single scattering albedo.

Comparison of the two methods

Table 5.10 gives the geometrical conditions of the observations for the two satellites of concern. We also report the aerosol optical thickness computed in the TM2 (or SPOT HRV XS1) band and the Junge slope ν derived from the spectral dependence of the aerosol optical depth. The predicted apparent reflectances and the relative difference between the reflectance- and irradiance-based methods are given in Table 5.11.

In the determination of the apparent radiance measured over high reflectance surfaces, the atmospheric effects are mainly described by the atmospheric transmittance. For both the upward path and the downward path, these atmospheric transmittances may be related directly to measurements of the direct and diffuse irradiances at the ground. The main advantage of this method is that it reduces the requirement for a complete and correct description of the aerosols. In a first attempt to use this technique, measurements were made during calibration campaigns at White Sands, New Mexico. We have some good indications from the spectral dependence of the diffuse-to-global ratio and from the repeatability of the measurements that the technique used is valid. The very good

Table 5.10. Geometrical conditions of the observations, aerosol optical depth, and Junge slope ν used for the aerosol characterization.					
Date	Time of Overpass	θ_s	θ_v	δ_A	ν
85.11.16 (TM)	17:07:24	57.2	0.0	0.0212	3.27
87.03.27 (TM)	17:09:00	41.5	0.0	0.1020	2.63
87.03.28 (SPOT)	18:18:21	32.3	31.1	0.0663	2.48
87.07.17 (SPOT)	17:39:17	23.5	30.2	0.0823	3.04
88.02.08 (SPOT)	18:17:18	50.2	32.0	0.0231	3.32
88.02.09 (SPOT)	17:58:03	51.5	0.9	0.0302	2.95
88.02.10 (TM)	17:08:08	56.8	0.0	0.0834	2.61

agreement (< 3%) with the reflectance-based method for four of the seven dates listed in Table 5.11 confirms the validity of the method. The discrepancies observed for the other days can be qualitatively explained by the presence of clouds and blowing gypsum. The analysis of the difference indicates some possibilities for improving both methods.

For the reflectance method, better characterization of the aerosols is needed starting with an accurate measurement and analysis of the SWIR optical depth. For the diffuse-to-global measurements, we need to correct our measurements for the non-lambertian properties of the BaSO₄ panel. We made corrections for the forward-diffuse contribution cut off by the parasol. The two methods have in common the use of optical depth measurements. The inaccuracies in the aerosol optical thickness determination affect the results of the reflectance method only slightly (Kastner 1985). Improvements in the ground

Table 5.11. Apparent reflectances computed using a transfer code and the irradiance method and relative difference (%).				
	<i>TM1</i>	<i>TM2</i>	<i>TM3</i>	<i>TM4</i>
85.11.16	0.4072 0.3983 2.2	0.4268 0.4259 0.2	0.4768 0.4763 0.1	0.5415 0.5554 -2.5
87.03.27	0.3459 0.3170 8.7	0.3704 0.3470 6.5	0.4064 0.3809 6.5	0.4658 0.4421 5.2
88.02.10	0.3531 0.3439 2.7	0.3675 0.3654 0.6	0.4036 0.3968 1.7	0.4629 0.4602 0.6
	<i>XS1</i>	<i>XS2</i>	<i>XS3</i>	
87.03.28	0.3692 0.3745 -1.4	0.4040 0.4022 0.5	0.4746 0.4908 -3.4	
87.07.17	0.4739 0.4463 6.0	0.5096 0.4887 4.2	0.5715 0.5777 -1.1	
88.02.08	0.3551 0.3585 -0.9	0.3905 0.3915 -0.3	0.4561 0.4642 -1.8	
88.02.09	0.3658 0.3701 -1.2	0.4034 0.4024 0.2	0.4684 0.4714 -0.6	

reflectance measurements are dependent on the BaSO_4 panel calibration; a laboratory method has been devised to update and improve this calibration (Biggar et al. 1988). The 87.03.27 results give a higher estimate of the apparent reflectance using the irradiance method. On this day, the site was surrounded by clouds and the results correspond with this fact. There are two opposite effects due to clouds: they scatter and so increase the diffuse irradiance measured on the site but they also shade part of the surrounding terrain and so reduce the contribution of the ground-atmosphere coupling term. It is very difficult to quantitatively estimate these two contributions. In the irradiance method, we assume a homogeneous ground and consequently the effect of the clouds is only related to the diffuse light they scatter over the site. It is probably this assumption that results in an overestimation of the reflectances using the irradiance method.

As expected, the largest differences between the two methods tend to occur at the shorter wavelengths where the atmospheric correction is maximum. For 85.11.16, under very clear conditions, the two methods give a good agreement ($\leq 2.5\%$). For 87.03.27 and 87.07.17, the irradiance method gives smaller apparent reflectances than the reflectance method. Some improvement in the size distribution determination should be made by using SWIR optical depth measurements. Bartell (1987) showed that in a log-log plot of the aerosol optical thickness versus the wavelength, two slopes occur for 87.03.27. This additional information may improve the estimate of the size distribution. The fact is that the Junge slope derived from the visible extinction measurements is rather small. That indicates a high density of large particles which is surprising for the clear atmosphere normally present at White Sands. These large particles lead to an overestimation of the forward scattering; the correspondingly large atmospheric transmittances lead to an overestimate of the signal.

On 87.07.17, there were strong winds during the morning with attendant blowing dust and gypsum sand. This affected our diffuse-to-global ratio measurements and restricted the angles at which measurements were made as it was very difficult to hold the parasol in the correct orientation. It also gave rise to spatial variations in measured optical depths and irradiance ratios. On this date our aerosol model is probably not accurate due to the variations in the aerosols near the ground. We also had to extrapolate to the view angle with very few measurements due to the wind.

We took three good sets of data during a field trip in February 1988 at White Sands. Weather was favorable on all three days and we made measurements over a good range of solar angles. Due to the time of year and the large solar zenith angle at solar noon, we had to extrapolate from our measurements to the ratio for the satellite view angle. The results from the two methods agree quite well (< 3% difference in all cases).

Conclusions

I have presented a new method for obtaining an in-flight radiometric calibration of an optical sensor. It uses measurements of diffuse and global irradiances in addition to spectral optical depths and ground reflectances. The ratios are corrected for the diffuse component blocked during the measurements and then interpolated or extrapolated to the values for the satellite and solar zenith angles. The atmospheric reflectance (ρ_A) and spherical albedo (s) are computed using a radiative transfer code or an approximate code such as 5S. The effects of gaseous absorption were computed using 5S based on measurements of O_3 and H_2O . The results, when compared to the results obtained from a reflectance-based method, are good. The irradiance-based method attempts to reduce the uncertainties related to the choice of an aerosol model.

CHAPTER 6

CONCLUSIONS AND RECOMMENDATIONS

I have discussed three methods for the absolute radiometric calibration of in-flight sensors in the previous chapters. Each method can give a reliable calibration and each has certain advantages and problems. By using all three methods for a given sensor, we can possibly identify problems in a method and correct them. The reasonably good agreement between methods on "good" calibration days is encouraging; the absolute calibration of an in-flight sensor is probably precise enough to know when the sensor has degraded by 2 % since launch and that an absolute calibration must be done on a temporal basis to correctly measure radiance. If, however, imagery users wish more accurate calibration than we can now provide, we must improve each of the three methods to lower the possible errors. In this chapter I shall discuss the merits and problems of each method, present tables of possible errors and an estimate of the magnitude of each, and make recommendations for improvements to each method.

Reflectance-based Method

The reflectance-based method has been used more often for absolute calibration of the TM and HRV sensors than the radiance or irradiance methods. Therefore, we have more samples upon which to judge its repeatability. We can show a decrease in the sensitivity of TM over time. In the reflectance-based method we measure the ground reflectance of a known target during satellite overpass. We then calculate the radiance at the sensor using a radiative transfer code that accounts for multiple scattering. The code requires atmospheric parameters including optical depths and an aerosol description. The code assumes that the aerosol scattering is adequately described by Mie scattering theory (spherical, homogeneous aerosols of a known, constant refractive index). The appropriate optical depths can be derived from solar radiometer measurements. In our calibration work, we have assumed

that the aerosol size distribution is described by a Junge power law. The exponent was determined from the spectral optical depths. The choice of a Junge law was probably good for most days, however, it may not have been correct for short wavelengths ($\lambda < 0.45 \mu\text{m}$) and for wavelengths longer than about $1 \mu\text{m}$ on some days. We have also assumed that the limits for the size distribution are 0.01 and $10.0 \mu\text{m}$. The effect on the radiance of changing the large limit is quite small, affecting mainly the strong forward scattering peak. The small size limit affects the diffuse field and may have had a measurable effect if the actual limit was quite different than the $0.01 \mu\text{m}$ used. The factor causing the largest uncertainty in the sensor radiance was the choice of the imaginary part of the complex refractive index (Kastner, 1985). This term controls aerosol absorption and can have a significant effect. We have used a wavelength independent value of first 0.01 and then 0.005 in our work. The latter figure is probably closer to the actual (but very difficult to determine) value. The diffuse-to-global measurements made during satellite calibration work do not have enough sensitivity to the refractive index to determine the index to the accuracy desired. Herman and Browning made several other assumptions in developing their code:

- 1.) a plane parallel horizontally homogeneous atmosphere
- 2.) a lambertian reflector at the base of the atmosphere
- 3.) that a grid of 13 positions in azimuth and 9 in zenith angle are sufficient for determining the scattered fields from the phase function.
- 4.) the ground surface is homogeneous and of infinite extent.

Using 5S it can be shown that there is a negligible error due to the atmospheric adjacency effect because of the high reflectance of the measurement site at White Sands and its 15 km distance from lower reflectance areas. However, for other smaller and lower reflectance sites, the adjacency effect may significantly affect the results if assumption 4 is made. For our satellite calibrations, assumptions 1 and 3 are probably good as long as the solar and

sensor zenith angles are less than about 60 degrees which is almost always true. Recent single plane BRF measurements for White Sands show that the sand is not lambertian, hence assumption 2 needs to be carefully checked.

Radiance-based Method

The radiance-based method is quite attractive if a well-calibrated radiometer can be carried high enough over the calibration target. The most important factor is an accurate calibration of the radiometer. If the radiometer is above 10,000 feet MSL in a White Sands type of atmospheric and reflectance condition, the corrections to convert the aircraft radiometer radiances to spacecraft level radiances are on the order of a few percent or less depending on wavelength. Therefore, a large uncertainty in the corrective term can be tolerated with only a very small effect on the overall sensor calibration. With current laboratory calibration procedures, the radiometer should be no more than 5 percent in error, probably less than 3 percent. The pointing of the radiometer is another possible problem, but the video imagery allows us to determine precisely when the radiometer is viewing the actual target. Target nonuniformities appear in both the sensor image and the radiometer data but a scene average reduces this problem as the radiometer data standard deviation are usually on the order of 2 percent of the mean reflectance value. The standard deviation of the ground reflectance as measured by backpack-mounted radiometers is nearly the same.

With this method, we want the radiometer bandpass to match that of the sensor to be calibrated. This reduces the effect of any solar or atmospheric absorption features (O_3 , NO_2 , O_2 , or water vapor). If we wish to make altitude corrections in the most accurate possible way, we also need all of the data and computations used in the reflectance-based method. The radiance-based method is then more complicated and requires more manpower and equipment. It also requires open airspace over the ground target during sensor overpass,

which may or may not be available at our normal site at White Sands due to higher priority military projects.

Irradiance-based Method

The irradiance-based method results compared well with those from the reflectance-based method when conditions were good at White Sands. This method requires the ground reflectance and optical depth measurements of the reflectance-based method along with a set of diffuse-to-global irradiance ratio measurements. It, like the radiance-based method, requires more measurements than the reflectance-based method, but the same equipment and people used in the reflectance-based method can be used. The irradiance-based method uses some approximations, however, the irradiance ratio measurements replace the assumptions and/or atmospheric inversions required to compute the aerosol scattering for the reflectance method. The two parameters, spherical albedo and atmospheric reflectance, derived from either approximate or "exact" codes for use in the irradiance method are small and errors in these parameters result in small changes in the final calibration. The current method of measuring the irradiance ratios requires a substantial angle dependent correction for the part of the diffuse field blocked by the parasol. A correction is also required for the non-lambertian characteristics of the BaSO_4 panel used in the measurement. For nadir viewing sensors, an extrapolation of the diffuse-to-global ratio to a zenith angle of zero is also required. For winter observations, especially at higher latitudes, this extrapolation may present a serious problem. This extrapolation also requires a stable atmosphere over the period from the largest zenith angle to solar noon.

Error Contributions

For each of the calibration methods presented, there are various possible error sources. Each method is capable of high precision, however high accuracy requires that each source of error be identified and reduced to the smallest possible amount. Some error sources

effect all three methods, however, the end result may be substantially different due to the final use of the error term. A good example is the effect of any errors in the radiative transfer computation. The same inputs and computation are used in the reflectance- and radiance-based calibrations. An error of 3 percent in the reflectance-based method computation would give a 3 percent error in the sensor calibration. The same computation error would give a negligible error in the radiance-based calibration because the 3 percent error applies only to the small (on the order of 2 percent or less) correction term.

Some of the error sources are errors in the measurement of ground reflectance, optical depths, and diffuse-to-global ratios, choice of complex refractive index for the aerosols, size limits, size distribution type, vertical distribution and exoatmospheric solar irradiance, the computation of absorption due to O_3 , NO_2 , O_2 , water vapor and other gases, the assumption of a lambertian characteristic for the ground, calibration of the radiometer and reflectance reference panels, and the choice of a non-polarized versus polarized computation of the scattering. We have also not considered polarization effects in either the radiometers or the in-flight sensors being calibrated. The error sources I have identified for each method are listed in tables 6.1 through 6.3 along with an estimate of the actual error in percent. The errors were estimated for band 2 of TM or XS1 of HRV in the visible part (green) of the spectrum. Some errors such as those for the atmospheric correction would be larger for shorter wavelengths. Many of the error sources for the reflectance-based method were investigated by Kastner (1985). There is also an additional worst case error estimate for the exoatmospheric irradiance ($E_{0\lambda}$) of less than 1% from Neckel and Labs (1984).

The tables show that there are a substantial number of identified problems. We assume that most of the major error sources are independent and compute the overall estimated uncertainty as the root sum of squares. For the irradiance method, the spherical albedo and atmospheric reflectance are not independent and the errors are of opposite sign. Thus they

Table 6.1. Reflectance-based method error sources, with reference to solar exoatmospheric irradiance.

<i>Source</i>	<i>Error (percent)</i>	<i>Overall Error (percent)</i>
Ground reflectance measurement		2.1
Reflectance panel calibration (BRF)	2.0	
Diffuse field Correction	0.5	
Measurement errors	0.5	
Optical depth measurement	5.4	1.1
Errors in extinction optical depth	5.0	
Errors in partition into Mie and Rayleigh	2.0	
Absorption computations		1.3
O ₃ amount error	20.0	
Choice of complex index of aerosols	2.0	2.0
Choice of size distribution of aerosols		
Type		3.0
Size limits	0.2	
Junge parameter	0.5	
Vertical Distribution	1.0	1.0
Non-lambertian ground characteristic	1.2	1.2
Non-polarized versus polarization code	0.1	0.1
Inherent code accuracy	1.0	1.0
Uncertainty in the value of μ_s	0.2	0.2
Total Error (root sum of squares)		4.9

are included in a single term. If imagery users need better accuracy than that allowed by the estimated uncertainties, we must reduce the errors. Some errors can be reduced by equipment modifications and refinements. Others will require further theoretical work or new measurements.

Table 6.2. Radiance-based method error sources			
<i>Source</i>	<i>Error</i>	<i>Overall</i>	<i>Error</i>
	<i>(percent)</i>	<i>(percent)</i>	
Radiometer calibration		2.5	
Panel calibration	2.0		
Lamp calibration	1.3		
Scale uncertainty	1.2		
Transfer uncertainty	0.5		
Lamp positioning	0.3		
Lamp current stability	0.5		
Voltage measurement error	0.5		
Measurement accuracy		1.3	
Data logger accuracy	0.5		
Radiometer stability	0.5		
Pointing angle errors ($\pm 10^\circ$)	1.1		
Correction for altitude difference		< 0.1	
Uncertainty in Reflectance-based method	5.0		
Total Error (root sum of squares) for radiance calibration		2.8	

Table 6.3. Irradiance-based method error sources, with reference to solar exoatmospheric irradiance.			
<i>Source</i>	<i>Error</i>	<i>Overall Error</i>	
	<i>(percent)</i>	<i>(percent)</i>	
Extinction optical depth	5.0	1.0	
Diffuse-to-global ratio measurement		2.3	
Field measurement	2.0	0.5	
Correction for blocked diffuse component	2.0	0.5	
Extrapolation to required angles	1.0	0.25	
Non-lambertian panel correction ($\theta_g \approx 50^\circ$)	2.2	2.2	
Ground reflectance measurement (See table 6-1)	2.1	2.1	
Spherical albedo and atmospheric reflectance		1.0	
Atmospheric model error	1.0		
Uncertainty in the value of μ_s and μ_v	0.4	0.1	
Total Error (root sum of squares)		3.5	

Recommendations

For the reflectance-based method, I recommend both new measurements and new methods of computation.

1.) Obtain a closer approximation to the full BRDF of the surface by measuring the BRDF over a large range of view angles ($\pm 70^\circ$) and in at least 3 planes (principal,

perpendicular to principal, and sensor scan). The BRDF should be measured at all angles used in the radiative transfer calculations ($\Delta\phi = 30^\circ$) if feasible.

- 2.) Determine the amount of polarization induced by reflection at the ground.
- 3.) Include the measured and estimated full BRDF and polarization effects of the ground in the radiative transfer computation.
- 4.) More accurately determine the reference panel BRDF as it directly affects the ground reflectance measurement and hence the calibration accuracy.
- 5.) Modify the laboratory reflectance measurement apparatus to enable measurement at and near the illumination angle (beam splitter) to look for retroreflections.
- 6.) Determine the polarization characteristics of the reflectance panel.
- 7.) Measure the extinction optical depth at more wavelengths and over a larger wavelength range. The range should be extended to at least $2.5 \mu\text{m}$ at the long wavelength limit and to about 0.3 to $0.35 \mu\text{m}$ at the short limit. The instrument would preferably be a spectrometer but a narrowband filter instrument would be acceptable.
- 8.) Attempt an actual size distribution inversion to check the validity of the choice of a Junge distribution.
- 9.) Make the computations with a polarization code, especially on days where the atmosphere is extraordinarily clear.
- 10.) Investigate the use of polarization sky measurements along with diffuse-to-global ratios to infer the spectral dependence of the imaginary part of the complex refractive index.
- 11.) Determine if the radiometers used in the reflectance measurements are sensitive to polarization.
- 12.) Investigate if the radiance-based method can help in determining the single scattering albedo for use in the reflectance-based method. The complex index input to the

code would be varied to try to reproduce the spectral radiance measured at the radiometer intermediate altitude.

For the radiance-based method, the major improvements would involve the calibration of the radiometer. Smaller improvements would result from the use of the suggested improvements for the reflectance-based method.

1.) Use absolute detectors to check the radiance calibration of the lamp/panel/radiometer combination.

2.) Carefully measure the out-of-field response of the Exotech/external SPOT filter combination for use over dark targets at high altitudes.

3.) Calibrate a spectrometer such as the Spectron SE-590 in radiance if it has sufficient stability.

4.) Mount a single-band absolute radiometer boresighted with the Exotech and Spectron as a stability and accuracy reference.

5.) Improve pointing accuracy or knowledge of pointing angle by adding orthogonal tilt sensors to the Exotech and recording angles along with the radiometer outputs.

6.) Improve collection and synchronization of time signals from the radiometer(s) and video.

7.) Extend the wavelength range to include future sensors (0.4 to 2.5 μm).

8.) Use any reflectance-based method improvements to reduce errors in the altitude correction term.

9.) To investigate the magnitude of the adjacency effect over dark targets, measure the radiance at several different altitudes at several distances from the edge of the dark target.

10.) If a spectrometer is used, attempt to determine the water vapor content between the radiometer and the ground using the method Gao and Goetz (1990) used with AVIRIS data.

For the irradiance-based method, the major improvement would come from the design and construction of an instrument for automated measurement of the diffuse-to-global ratio.

1.) Design a new instrument to minimize the blocked diffuse component and especially the change in this component with solar zenith angle. The new instrument might use an integrating sphere to reduce the effects of the non-lambertian BaSO_4 panel and any polarization effects. It might also use a spectrometer (or radiometer with many more than 4 or 7 bands) to more accurately determine the spectral dependence. Automation would allow the collection of more data to help in the determination of atmospheric stability and the accuracy of the extrapolation to the sensor zenith angle (if required).

2.) Use an "exact" instead of approximate code to compute the spherical albedo.

3.) Extend the range of spectral coverage to that proposed for the reflectance-based method.

4.) Include any measurement improvements made in the reflectance-based method.

If some of these recommendations are implemented, the uncertainties in the sensor calibration would be reduced. This could help meet the stated accuracy requirements of some investigators. One real problem in the use of a "calibrated" sensor is, however, the lack of knowledge of the solar irradiance on the ground. If the ground surface is tilted, the reflectance determined from the imagery of a perfectly calibrated sensor will be wrong because of the assumption of a flat ground surface. Hence, to accurately use data from a calibrated sensor, an investigator needs a database of terrain slopes. An imaging sensor with a sensitive and accurate stereo capability would be useful.

LIST OF REFERENCES

- Abel, P., Smith, G. R., Levin, R. H., Jacobowitz, H. (1988), Results from aircraft measurements over White Sands, New Mexico, to calibrate the visible channels of spacecraft instruments, *Proc. SPIE* 924:208-214.
- Bartell, R. J. (1987), *Atmospheric corrections for in-flight satellite radiometric calibration*, M.S. thesis, University of Arizona, 100 pp.
- Biggar, S. F., Labeled, J., Santer, R. P., Slater, P. N., Jackson, R. D., and Moran, M. S. (1988), Laboratory calibration of field reflectance panels, *Proc. SPIE* 924:232-240.
- Born, M. and Wolf, E. (1980), *Principles of Optics*, Pergamon Press, Oxford, England.
- Castle, K. R. (1985), *Absolute radiometric calibration of a spectropolarimeter*, PhD dissertation, University of Arizona, 129 pp.
- Chandrasekhar, S. (1950), *Radiative Transfer*, Oxford University Press, Oxford, England.
- Coulson, K. L. (1988), *Polarization and intensity of light in the atmosphere*, A. Deepak Publishing, Hampton, Virginia.
- Coulson, K. L., and Jacobowitz, H. (1972), Proposed Calibration Target for the visible channel of a satellite, *NOAA Tech. Rep. NESS* 62, 27 pp.
- Deuzé, J. L. (1974), *Etude de la polarisation du rayonnement par les milieux diffusants, Application a la polarisation localisee de Venus*, Thèse, Lille, France.
- Dobrowolski, J. A. (1978), Coating and Filters, *Handbook of Optics*, edited by Driscoll, W. G., and Vaughan, W., McGraw-Hill Book Company, New York.
- Elterman, Louis (1968), *UV, Visible, and Ir Attenuation for altitudes to 50 km*, Report AFCRL-68-0153, Air Force Cambridge Research Laboratories, Bedford, Mass., 49 pp.
- Fraser, R. S., Bahethi, Om P., Al-Abbas, A. H. (1977), The effect of the atmosphere on the classification of satellite observations to identify surface features, *Remote Sens. Environ.* 6:229-249.
- Frouin, R., and Gautier, C. (1987), Calibration of NOAA-7, AVHRR, GOES-5 and GOES-6 VISSR/VAS solar channels, *Remote Sens. Environ.* 22:103-127.
- Gao, B. and Goetz, A. F. H. (1990), Column atmospheric water vapor retrievals from airborne imaging spectrometer data, *J. Geophys. Res.*, in press.
- Goody, R. M. (1964), *Atmospheric Radiation*, Oxford University Press, New York, New York.

- Gordon, H. R., Clark, D. K., Brown, J. W., Brown, O. B., Evans, R. H., and Broenkow, W. W. (1983), Phytoplankton pigment concentrations in the middle Atlantic bight: comparison of ship determinations and CZCS estimates, *Appl. Opt.* 22:20-36.
- Gordon, H. R. (1987), Calibration requirements and methodology for remote sensors viewing the ocean in the visible, *Remote Sens. Environ.* 22:103-126.
- Gradshteyn, I. S., Ryzhik, I. M. (1980), *Tables of Integrals, Series, and Products*, Academic Press, Inc, New York, New York.
- Griggs, M. (1973), Determination of aerosol content in the atmosphere, *Symposium on significant results of ERTS-1*, NASA SP-327:1104-1113.
- Herman, B. M. (1963), *A numerical solution to the equation of radiative transfer for particles in the Mie region*, Ph.D. dissertation, University of Arizona, 130 pp.
- Herman, B. M. (1989), Personal communication, Department of Atmospheric Sciences, University of Arizona.
- Herman, B. M., and Browning, S. R. (1965), A numerical solution to the equation of radiative transfer, *J. Atmos. Sci.* 22:559-566.
- Herman, B. M., and Browning, S. R. (1975), The effect of aerosols on the earth-atmosphere albedo, *J. Atmos. Sci.* 32:158-165.
- Holm, R. G., Moran, M. S., Jackson, R. D., Slater, P. N., Yuan, B., Biggar, S.F. (1989), Surface reflectance factor retrieval from Thematic Mapper data, *Remote Sens. Environ.* 27:47-57.
- Hovis, W. A., Knoll, J. S., and Smith, G. R. (1985), Aircraft measurement for calibration of an orbiting spacecraft sensor, *Appl. Opt.*, 24:407-410.
- Hsia, J. J. and Weidner, V. R. (1981), NBS 45°/normal reflectometer for absolute reflectance factors, *Metrologia* 17:97-102.
- Hulstrom, R. L. (1975), Spectral measurements and analyses of atmospheric effects on remote sensor data, *Proc. SPIE* 51:90-100.
- Iqbal, M., (1983), *An Introduction to Solar Radiation*, Academic Press, Inc, New York, New York.
- Jackson, R. D., Moran, M. S., Slater, P. N., and Biggar, S. F. (1987), Field calibration of reference reflectance panels, *Remote Sens. Environ.* 22:145-158.
- Junge, C. E. (1963), *Air Chemistry and Radioactivity*, Academic Press, Inc, New York, New York.
- Justus, C. G. (1988), Calibration of satellite shortwave sensors using overcast cloudlayer targets, *Proc. SPIE* 924:120-128.

- Kastner, C. J. (1985), *In-flight absolute radiometric calibration of the Landsat thematic mapper*, Ph.D. dissertation, University of Arizona, 195 pp.
- Koepke, P. (1982), Vicarious satellite calibration in the solar spectral range by means of calculated radiances and its application to Meteosat, *Appl. Opt.* 21:2845-2854.
- Kneizys, F. X., Shettle, E. P., Abreau, L. W., Chetwynd, J. H., Anderson, G. P., Gallery, W. O., Selby, J. E. A., and Clough, S. A. (1988), *Users Guide to LOWTRAN 7*, AFGL-TR-88-0177, ERP, No. 1010, Air Force Geophysics Laboratory, Hanscom AFB, Mass.
- Kriebel, K. T. (1981), Calibration of the METEOSAT-VIS channel by airborne instruments, *Appl. Opt.* 20(1):11-12.
- Liou, K. (1980), *An Introduction to Atmospheric Radiation*, Academic Press, Inc, Orlando, Florida.
- Markham, B. L. and Wood, F. M. (1988), Radiometric calibration of the reflective bands of NS001 thematic mapper simulator (TMS) and modular multispectral radiometers (MMR), *Proc. SPIE* 924:96-108.
- Malkmus, W. (1967), Random Lorentz band model with exponential-tailed S^{-1} Line-intensity distribution function, *J. Opt. Soc. Am.* 57:323-329.
- Mie, G. (1908), A contribution to the optics of turbid media, especially colloidal metallic suspensions, *Ann. Phys.* 25:377-445, in German.
- Nautical Almanac Office (1988), *Almanac for Computers 1988*, United States Naval Observatory, Washington, DC.
- Neckel, H. and Labs, D. (1984), The solar radiation between 3300 and 12500 A, *Solar Phys* 90:205-258.
- Palmer, J. M. and Tomasko, M. G. (1980), Broadband radiometry with spectrally selective detectors, *Opt. Lett.* 5(5), 208-210.
- Phillips, A. L. (1985), *Absolute calibration of, and atmospheric measurements using, a multiband field radiometer*, M.S. thesis, University of Arizona, 95pp.
- Potter, J. F. (1975), Haze and sun angle effects on automatic classification of satellite data - simulation and correction, *Proc. SPIE* 51:71-83.
- Reagan, J. A. (1989), Personal communication, Department of Electrical and Computer Engineering, University of Arizona.
- Robinson, B. R., and Biehl, J. J. (1979), Calibration procedures for measurement of reflectance factor in remote sensing field research, *Proc. SPIE*. 196:16-26.
- Sargent, M. III (1985), Class notes, Optical Sciences 543, Laser Physics, Optical Sciences Center, University of Arizona.

- Schott, J. R. (1988), Thematic Mapper, band 6, radiometric calibration and assessment, *Proc. SPIE* 924:72-88.
- Schaefer, A. R., Saunders, R. D., Hughley, J. R. (1984), Intercomparison between irradiance scales based on silicon photodiode physics, gold point blackbody radiation, and synchrotron radiation, *Proc. SPIE* 499:15-23.
- Schneider, W. E. (1986), *Report of calibration of one standard of spectral irradiance*, Optronic Laboratories, Inc, Orlando, Florida.
- Slater, P. N., Biggar, S. F., Holm, R. G., Jackson, R. D., Mao, Y., Moran, M. S., Palmer, J. M., and Yuan, B. (1986), Absolute radiometric calibration of the thematic mapper, *Proc. SPIE* 660:2-8.
- Slater, P. N., Biggar, S. F., Holm, R. G., Jackson, R. D., Mao, Y., Moran, M. S., Palmer, J. M., and Yuan, B. (1987), Reflectance- and radiance-based methods for the in-flight absolute calibration of multispectral sensors, *Remote Sens. Environ.* 22:11-37.
- Slater, P. N. (1988), Review of the calibration of radiometric measurements from satellite to ground level, invited paper presented at Commission VII WG 3 Int. Soc. Photogrammetry and Remote Sensing in Kyoto, Japan, June 1988.
- Stratton, J. A. (1941), *Electromagnetic Theory*, McGraw-Hill, New York.
- Tanré, D. (1982), *Interaction rayonnement-aerosols applications a la teledetection et au calcul du bilan radiatif*, Thèse, Lille, France.
- Tanré, D., Deroo, C., Duhaut, P., Herman, M., Jorcrette, J., J., Perobos, J., Deschamps, P., Y. (1986), *Simulation of the satellite signal in the solar spectrum (5S)*, Laboratoire d'Optique Atmosphérique Université des Sciences et Techniques de Lille, Lille, France.
- Turner, R. E., Malila, W. A., Nalepka, R. F., and Thomson, F. J. (1975), Influence of the atmosphere on remotely sensed data, *Proc. SPIE* 51:101-114.
- Vigroux, E. (1953), Contribution a l'étude expérimentale de l'absorption de l'ozone, *Ann. Phys.* 8:709-762.
- Weidner, V. R. and Hsia, J. J. (1981), Reflection properties of pressed polytetrafluoroethylene powder, *J. Opt. Soc. of Am.* 71:856-861.
- Weidner, V. R., Hsia, J. J., and Adams, B. (1985), Laboratory intercomparison study of pressed polytetrafluoroethylene powder reflectance standards, *Appl. Opt.* 24:2225-2230.
- van de Hulst, H. C. (1957), *Light scattering by small particles*, John Wiley & Sons, Inc., New York, New York.
- Young, A. T. (1981), On the Rayleigh-scattering optical depth of the atmosphere, *J. App. Met.* 20:328-330.